

**Study of Wide-Band Gap Oxide and Nitride-Based Semiconductors: Characterization
and Device Physics**

BY

KETAKI SARKAR

B.Tech Jadavpur University, Kolkata, 2010

B.Sc (Honors) University of Calcutta, Kolkata, 2007

THESIS

Submitted as partial fulfillment of the requirements
for the degree of Doctor of Philosophy in Electrical and Computer Engineering
in the Graduate College of the
University of Illinois at Chicago, 2018
Chicago, Illinois

Defense Committee:

Mitra Dutta, Chair and Advisor

Michael A. Stroscio

Junxia(Lucy) Shi

Vitali Metlushko

Alan Nicholls, Research Resource Center, UIC

Copyright by
Ketaki Sarkar
2017

*To my parents Mr. SibaPrasad Sarkar and Mrs. Ratna Sarkar, my husband Riddha and
my little Raika.*

ACKNOWLEDGEMENTS

Firstly, I would like to express my gratefulness to my advisor Dr. Mitra Dutta for giving me the opportunity to work in her research group. I am immensely thankful to her for all her support, guidance and patience in me. Working under her supervision has been one of the most enriching experience of my academic career and has helped me grow as an independent researcher. Thank you for all your suggestions and discussions that have completely changed my approach to scientific research and have enriched me in several ways. Your words of encouragement have always been a strong driving force in both research and other aspects of life. You have been and will always be my role model.

I would like to thank Dr. Michael Stroschio for being my thesis committee member. Your amazing lectures in the course Nanoscale Semiconductor Structures have been extremely insightful and helpful to my research. Thank you for all your feedbacks and discussions during our research group meetings which have certainly expedited my work. You are one of the most wonderful professor I have ever met.

I would like to extend my thanks to Dr. Vitali Metlushko, Dr. Junixia (Lucy) Shi in the ECE Department at UIC and Dr. Alan Nicholls at the Research Resource Center at UIC for agreeing to be my committee member and review my thesis. I would like to thank Dr. Alan Nicholls, Dr. Fengyuan Shi and Olivia Thomson for all the help with their expertise in SEM, TEM, XPS and Raman system at RRC, UIC.

A considerable portion of my experimental results are from the Centre for nanoscale Materials Division at Argonne National Laboratory. This wouldn't have been possible without the immense

ACKNOWLEDGEMENTS (continued)

cooperation from Dr. Richard Scaller, Dr. Gary Wiederrecht and Dr. David Gosztola. I am thankful for all their time and help with the experiments. My sincere acknowledgement to Dr. Ralu Divan for all the trainings, guidance and being so helpful in all means.

I am extremely grateful to my fellow lab members Souvik Mukherjee and Debopam Dutta in the Nano Engineering Research Laboratory. Thank you for being such wonderful friend, helpful colleagues and playing an incredible role in my research work.

I extend my gratitude to the research grants from the Air Force Office of Scientific Research, my advisor and the department of Electrical and Computer Engineering at University of Illinois-Chicago for supporting me through these years of my Ph.D.

Thank you my dear friends Soumya, Adita, Anna, Nirupam and Somak for the all good times, the warmth and togetherness.

It's beyond any words to express my indebtedness to my parents and my sister who have stood by me through thick and thins, and showering me with so much love. Thank you for the never-ending encouragement and faith which have helped me accomplish this milestone of my career. My special acknowledgement to my husband Riddha, for all your unconditional love and encouragement over the years. Thank you for being the best friend, I could have ever asked for. I would have never been able to complete this journey without your unflinching support and care. Raika, my daughter, the sunshine on my shoulder: you have been truly swishing your magic wand in my life.

KS

CONTRIBUTION OF AUTHORS

The results and discussions in this thesis are copied both from my published papers and submitted manuscripts with provided permission from the journal (see appendix). The contributions of all the co-authors are listed as follows:

Authors' contribution in chapter 3 and 4: Dr. Mitra. Dutta led the project and helped with the development of main ideas including revision of the manuscript. Ketaki Sarkar performed the experiments and wrote the manuscript. Dr. Gary Wiederrecht, Dr. Richard Schaller helped with the experiments at Argonne. Souvik Mukherjee contributed to discussions.

Authors' contribution in chapter 5: Dr. Mitra Dutta led the project, supervised the experimental data analysis and manuscript preparation. Ketaki Sarkar performed all the experiments and wrote the manuscript. Souvik Mukherjee and Sidra Farid contributed to experiments and discussions.

Authors' contribution in chapter 6: Dr. Michael. A. Stroschio and Dr. Mitra. Dutta led the project and helped with the development of main ideas. The experiments were done by Ketaki Sarkar and the theoretical calculations were derived by Debopam Dutta. The major part of the manuscript (to be submitted) has been written by Ketaki Sarkar while Debopam Dutta contributed to the theoretical section writeup.

TABLE OF CONTENTS

<u>CHAPTER</u>	<u>PAGE</u>
1. INTRODUCTION.....	1
1.1 Semiconductor Nanowires	1
1.2 Wide band gap materials.....	2
1.3 Research Objectives	5
1.4 Dissertation Outline	9
2. OPERATING PRINCIPLE AND EXPERIMENTAL SET-UP	12
2.1 Overview of the chapter	12
2.2 Chemical Vapor Deposition (CVD) growth furnace.....	13
2.3 Raman spectroscopy.....	16
2.4 Photoluminescence spectroscopy	21
2.5 Pump-probe spectroscopy	22
2.6 Streak Camera Detector/Time-resolved photoluminescence	24
2.7 Conclusion	25
3. STUDY OF ULTRAFAST CARRIER DYNAMICS OF ENHANCED NEAR-BAND-EDGE EMISSION FROM ARGON-PLASMA TREATED ZINC OXIDE NANORIBBONS	26
3.1 Overview of the chapter	26
3.2 Background of surface treatment on ZnO nanostructures.....	26
3.3 Experimental details.....	28
3.4 Results and discussion.....	29
3.4.1 Structural analysis of ZnO nanoribbons.....	29
3.4.2 Surface treatment of ZnO nanoribbons	31
3.4.3 Photoluminescence of surface treated ZnO nanoribbons	31
3.4.4 Analysis of carrier dynamics and relaxation time of ZnO nanoribbons.....	36
3.5 Conclusion	39
4. STIMULATED EMISSION AND OPTICAL PUMPING OF LASING FROM ZINC OXIDE NANOSTRUCTURES: EFFECT OF MORPHOLOGY AND SURFACE TREATMENT ON THE THRESHOLD AND EFFICIENCY	40
4.1 Overview of the chapter	40
4.2 High-excitation photoluminescence from different ZnO nanostructures.....	41
4.2.1 Stimulated emission of different ZnO nanostructure	42
4.2.2 Effect of morphology on the stimulated emission.....	43
4.3 Lasing from surface passivated ZnO nanoribbons	45
4.3.1 Integrated peak intensity and pump fluence.....	46
4.3.2 Threshold and slope efficiency	48
4.3.3 Time-resolved photoluminescence.....	50
4.4 Conclusion	52

TABLE OF CONTENTS (continued)

<u>CHAPTER</u>	<u>PAGE</u>
5. STUDY OF AN ENSEMBLE OF INDIUM OXIDE AND ZINC OXIDE NANOSTRUCTURES.....	53
5.1 Overview of the chapter	53
5.2 Background of the doped indium oxide nanowires.....	53
5.3 Growth of co-existing In ₂ O ₃ and ZnO nanowires	54
5.4 Morphology of the as grown nanowires.....	55
5.5 Elemental analysis of the nanowires	58
5.6 Photoluminescence studies on the co-existing nanowires.....	59
5.6.1 Room temperature photoluminescence spectroscopy	59
5.6.2 High-temperature photoluminescence spectroscopy.....	60
5.7 Raman spectroscopy measurements.....	63
5.8 Conclusion	66
6. OPTICAL PHONON MODES FROM A SHORT PERIOD ALUMINIUM NITRIDE/GALLIUM NITRIDE SUPERLATTICE	67
6.1 Overview of the chapter	67
6.2 Background on AlN/GaN based superlattice	68
6.3 Experimental details.....	69
6.4 Results and discussions	71
6.4.1 Raman spectroscopy on short period superlattice	71
6.4.2 Temperature Calibration using Raman Spectroscopy	74
6.5 Conclusion	76
7. OPTICAL PROPERTIES OF A SHORT PERIOD ALUMINIUM NITRIDE/GALLIUM NITRIDE SUPERLATTICE UNDER HIGH-EXCITATION AND HIGH TEMPERATURE	77
7.1 Overview of the chapter	77
7.2 Results and discussions	79
7.2.1 Photoluminescence under high excitation density	80
7.2.2 Electron temperature from photoluminescence spectra	82
7.2.3 High-temperature PL at different high-power excitation	83
7.3 Time-resolved photoluminescence of SL layer as a function of pump power	86
7.4 Conclusion	87
8. CONCLUSION AND FUTURE WORK.....	88
8.1 Conclusion	88
8.2 Future Work	92

TABLE OF CONTENTS (continued)

<u>CHAPTER</u>	<u>PAGE</u>
APPENDICES	93
APPENDIX A	94
APPENDIX B	95
CITED LITERATURE	99
VITA	115

LIST OF FIGURES

<u>FIGURES</u>	<u>PAGE</u>
1 Energy band diagram of insulator, semiconductor and metal.....	3
2 List of some widely studied materials with their band gaps	4
3 Schematic outline of the thesis	11
4 Growth furnace set up at Nanotechnology Core Facility, UIC.....	13
5 Schematic diagram of the inside of a quartz tube containing the growth precursor and growth substrates ..	14
6 Flow diagram for the growth of nanowires on an Au coated Si substrate. Au acts as the catalyst for the growth	15
7 Raman scattering showing both Stokes and Anti-Stokes lines	17
8 Schematic diagram of the Raman system at Nano Engineering Research Laboratory, UIC	18
9 Raman/PL set-up at Nano Engineering Research Laboratory, UIC	18
10 Renishaw inVia Reflex Raman system at Centre for Nanoscale Materials in Argonne National Laboratory	19
11 Renishaw inVia Reflex Raman system at Centre for Nanoscale Materials in Argonne National Laboratory	20
12 Mechanism of Photoluminescence	22
13 Schematic of the pump-probe spectroscopy	23
14 Experimental setup of a pump-probe spectroscopy measurement at ANL in CNM.....	24
15 Principle of operation of a streak camera detector system	25
16 (a) SEM image of the randomly grown ZnO nanoribbons on Au coated Si substrate. The inset shows the SEM image of a magnified ribbon for better clarity of the thickness. (b) Raman spectrum of ZnO nanoribbons obtained using back-scattering geometry.....	30

LIST OF FIGURES (continued)

<u>FIGURES</u>	<u>PAGE</u>
17 (a) Room Temperature PL spectra of the as grown and Ar-plasma treated ZnO nanoribbons. Removal of the surface states acting as the alternative de-excitation pathways resulted in the huge enhancement of the UV emission peak and simultaneous reduction in the visible emission peak. The inset shows the dependency of the UV peak intensity on the surface treatment time. Prolonged exposure of the nanostructures to the Ar plasma results in the degradation of the material quality. (b) Comparative plot of the room Temperature PL spectra before and after sputter coating the nanoribbons with Au metallic nanoparticles and Ar-plasma treatment. (c) Left image shows the energy band diagram of ZnO showing band bending and presence of surface traps. The right-hand side image shows the possible relaxation pathways for the carriers in ZnO.	33
18 Effect of surface plasmon resonance on the emission of Au coated ZnO nanoribbons	35
19 (a) Dynamics of the absorption spectrum at different probe delays following an excitation with a 325nm, 120fs, 600 μ W pump pulse and (b) relaxation dynamics for different pump energy for plasma etched ZnO nanoribbons. Comparison of the (c) spectral behavior as function of different time delays and (d) temporal behavior of the nanofibers at the highest pump fluence before and after plasma treatment. Surface modification resulted in the faster relaxation dynamics	38
20 Scanning electron microscopy images of (a) ZnO nanowires, (b) ZnO nanofibers and (c) ZnO ribbons. The inset images in each of the figures shows the magnified structures.....	42
21 Photoluminescence spectra of (a) ZnO nanowire, (b) ZnO nanofibers and (c) ZnO ribbons measured using a 325nm excitation under different pump-fluence.....	43
22 Logarithmic plot of integrated peak intensity vs Pump Power for (a) ZnO nanowire, (b) ZnO nanofibers and (c) ZnO nanoribbons.....	44
23 Evolution of PL spectra with pump power	45
24 (a) and (b) Evolution of the emission spectra as a function of the excitation intensity in as grown and Ar plasma treated ZnO nanoribbons. Characteristics lasing spectra are observed in both the cases at high laser energy.....	47
25 (a) and (b) log-log plot of the integrated peak intensity with the excitation energy showing the threshold behavior in either cases. Clearly, plasma treatment results in the decrease of the lasing threshold of the ZnO nanoribbons	49
26 Time-resolved photoluminescence spectra of (a) as-grown ZnO nanoribbons and (b) etched ZnO nanoribbons respectively measured at different pump-fluences	51

LIST OF FIGURES (continued)

<u>FIGURES</u>	<u>PAGE</u>
27 (a) SEM image of the In ₂ O ₃ nanowires, (b) SEM image of an ensemble of In ₂ O ₃ -ZnO nanowires with additional ZnO fibrous structures.	56
28 (a) TEM image of the In ₂ O ₃ nanowires. The gold tip at the top of the nanowire is shown in the inset image, (b) TEM image of the ZnO nanowires (c) the EDX spectra of the stem of the In ₂ O ₃ nanowires and of the Au tip (inset image), (c) the EDX spectra of ZnO nanowires.	57
29 (a) TEM image of the In ₂ O ₃ nanowires with ZnO nanofibers. (b) EDX spectra of the In ₂ O ₃ nanowires (c) EDX spectra of the ZnO nanofibers.	57
30 XPS spectra of the In ₂ O ₃ -ZnO nanostructures showing both measured and fitted data. (a) High resolution spectrum of C1s with a peak at 285.33 eV, (b) high resolution spectrum of O1s with peaks at 530.21 eV and 531.88 eV, (c) high resolution spectrum of In3d _{5/2} and In3d _{3/2} with peaks at 444.69 eV and 451.94 eV, and (d) high resolution spectrum Zn2p _{3/2} and Zn2p _{1/2} with peaks at 1022.11 eV and 1046.78 eV....	58
31 Room temperature photoluminescence spectra of In ₂ O ₃ nanowire and In ₂ O ₃ -ZnO nanostructures; both the curves have been fit using Gaussians. The magnified peak of the near UV emission at the bandgap of ZnO is shown in the inset image	60
32 Low temperature PL spectra of (a) In ₂ O ₃ nanowires, and (b) In ₂ O ₃ -ZnO nanostructures. The left inset image in (a) and (b) are the integrated PL intensities as functions of temperature. In the right inset image in (b) is shown the resolved UV peaks at 30K for better peak identification	62
33 Room temperature Raman spectra of (a) In ₂ O ₃ showing distinct modes of the cubic crystal, and (b) In ₂ O ₃ -ZnO with additional non-polar and quasi LO phonon modes of the polycrystalline wurtzite crystal of ZnO nanowires in addition to the vibrational modes from cubic In ₂ O ₃ nanowires.	65
34 (a) HRSTEM images of the heterostructure after growth showing the presence of a thin AlN cap layer followed by the 4 period AlN/GaN superlattice and finally a mixture of AlN and GaN where the Ga composition increases towards the GaN buffer layer, (b) distribution of all elements across the top heterostructure.	70
35 (a) Raman spectra of the AlN/GaN superlattice with a 514 nm excitation under back scattering geometry (b) Theoretically obtained dispersion curve for the same structure using Dielectric Continuum Model.	73
36 Theoretical and experimental plot of Stokes/Anti-stokes ratio of $E_2(\text{high})$ and $A_1(\text{LO})$ as a function of temperature. The inset image shows the gaussian fitted peak of $E_2(\text{high})$ and the deconvoluted peak of $A_1(\text{LO})$ on the Stokes side.	75

LIST OF FIGURES (continued)

<u>FIGURES</u>	<u>PAGE</u>
37 Energy band diagram of a AlN/GaN superlattice showing the offset of conduction and valence band. The energies are calculated with reference to the vacuum energy level which has been set to zero.	78
38 Schematic diagram of different relaxation process under photoexcitation of $h\nu > E_g$	79
39 Photoluminescence spectra of AlN/GaN SL at different excitation power with the sample excited at the edge. The inset image shows PL spectra when excited at the center of the sample.	81
40 Evolution of the carrier temperature as a function of the laser power	83
41 Photoluminescence from SL with 325nm excitation at different high temperatures	85
42 Log-log plot of integrated PL intensity as a function of the laser power at different temperatures	85
43 Time resolved photoluminescence spectra measured at room temperature under different excitation intensity	86

LIST OF ABBREVIATIONS

1-D	One dimensional
ASE	Amplified Spontaneous Emission
AlN	Aluminum Nitride
Ar	Argon
Au	Gold
CCD	Charge Coupled Detector
CVD	Chemical Vapor Deposition
DAP	Donor Acceptor Pair
2DEG	Two-Dimensional Electron Gas
EDX	Energy Dispersive X-ray Spectroscopy
EHP	Electron Hole Plasma
eV	Electron Volt
FET	Field Effect Transistor
fs	Femto-second
FWHM	Full-Width Half Maximum
GaN	Gallium Nitride
HeCd	Helium Cadmium
HEMT	High Electron Mobility Transistor
HRSTEM	High Resolution Scanning Transmission Electron Microscopy
In ₂ O ₃	Indium Oxide
kHz	Kilo Hertz
mJ	Milli Joule
LED	Light Emitting Diodes
LO	Longitudinal optical
meV	Milli Electron Volt

LIST OF ABBREVIATIONS (continued)

μ W	Micro Watt
NBE	Near Band Edge
nm	Nanometer
NW	Nanowire
NR	Nanoribbon
PL	Photoluminescence
ps	Pico-seconds
RT	Room Temperature
SEM	Scanning electron Microscopy
Si	Silicon
SL	Superlattice
SPR	Surface Plasmon Resonance
TEM	Transmission Electron Microscopy
TO	Transverse Optical
TRPL	Time-Resolved Photoluminescence Spectroscopy
UV	Ultraviolet
VLS	Vapor Liquid Solid
XPS	X-ray Photoelectron Spectroscopy
ZnO	Zinc Oxide

SUMMARY

Wide band gap materials like ZnO and GaN have come to the forefront of several technological applications over the past decades or so due to their wide variety of electrical and optical properties. The increasing need for short wavelength material alongside high-power and high-frequency devices have encouraged a strong wave of research amongst the scientific community. While, the breakthroughs in the high-quality growth of these materials have been achieved demonstrating promising device applications, further research is warranted in terms of control of electronics structure, improvement in crystalline quality, better control over defects and impurities, more efficient device designs etc. And to push further their potential applications, it is critical to better understand the dynamics and the underlying physics of these structures based on these materials.

ZnO is one of the very interesting wide band gap material with direct band gap, large excitonic binding energy. While it offers a unique possibility of next-generation short-wavelength optoelectronic devices, it still does have obstacles like extrinsic defects or surface traps that effects its emission properties considerably. An effort to eliminate these surface traps to improve the near band edge emission have been discussed in this thesis. The large surface to volume ratio of the ZnO nanostructures introduces these surface traps. Presence of these traps results in very weak near band edge emission but a strong visible emission. While there are several procedures to improve emission from the ZnO nanostructures, a very easy and quick approach has been presented here. An SEM coater system is used to etch the ZnO nanostructures using Ar-plasma. These resulted in a significant enhancement of the near band edge emission and considerable quenching of the visible peak. Controlling the etching time, it is possible to completely passivate these surface traps acting as the non-radiative recombination centers. Sputter coating with gold metallic nanoparticles also

SUMMARY (continued)

resulted in improved emission from near band edge, the elemental logic of which was interpreted in terms of surface plasmons. In context of these improvements in the emission from these nanostructures, further work was done to study the effect of the surface treatment on the carrier dynamics using transient absorption spectroscopy. Improved dynamics with higher density of excitons and faster relaxation time constants were observed in case of the surface passivated ZnO nanostructures as compared to the as-grown ones. Further, extending this study to examine the effect of this Ar-plasma etching on the optical lasing from these nanostructures revealed a higher efficiency and lower threshold of lasing. A faster time decay was observed near the lasing threshold in case of the surface treated nanostructures as demonstrated using time-resolved photoluminescence spectroscopy using femto-second pulse excitation. A comparative study on different as-grown ZnO structures namely nanowires, nanofibers and ribbons as a function of photoexcitation power was done. Better efficiency of stimulated emission was observed for the ZnO ribbons owing to their smaller surface to volume ratio. On the other hand, a higher threshold was observed for the same since larger density of carriers were required to achieve ASE (amplified spontaneous emission).

Band-gap engineering is one of the most sought-after technique to alter the electrical and optical properties of any semiconducting materials. Indium oxide nanowires are doped with smaller atomic percentage by weight of metals like Zn or Sn to accommodate it into specific applications. An attempt to highly dope In_2O_3 nanowires with Zn and analyzing the morphology of the resultant nanostructures has been presented. The presence of an ensemble of In_2O_3 and ZnO nanowires on the growth substrate was concluded based on structural, elemental and optical characterization

SUMMARY (continued)

techniques. SEM and TEM identified two separately grown distinct In_2O_3 and ZnO nanowires. XPS showed the presence of individual elements of In, Zn and O. While EDX along with PL and Raman measurements confirmed the facts that neither heavy doping was achieved, nor alloying, but separately existing nanowires and nanofibers of In_2O_3 and ZnO were formed.

Group III nitrides materials like AlN and GaN with high breakdown voltages, high thermal conductivity and high electron mobility are ideal candidates for the fabrication of high voltage and high temperature operating devices. Heterostructures or superlattices of these materials have been widely studied in this context. Understanding the vibrational and optical properties of the basic structure is therefore fundamental to the optimization of the device performance. In the latter part of the thesis, characterization of short period AlN/GaN superlattice grown on GaN buffer layer on Sapphire substrate using non-resonant Raman spectroscopy and Photoluminescence spectroscopy have been discussed. Optical phonon modes obtained from Raman spectroscopy in back-scattering geometry were identified and assigned to be originating from the superlattice structure and interfaces and underlying alloy. Analysis of the ratio of Stokes/anti-Stokes by examining the temperature dependent population of phonons resulting in stress-independent Raman measurements has also been discussed. Emission from the superlattice as a function of increasing excitation density has been studied. At high excitation, the shorter wavelength peak resulted due to the PL emission from the superlattice while the peak at the long wavelength was due to the band edge emission from the GaN buffer layer. High-energy tail of the PL spectra has been used to calculate the carrier temperature as a function of the laser density. A radiative recombination model was utilized to analyze the emission from the superlattice at different high temperatures.

1. INTRODUCTION

In the last several years, the role of semiconductor nanostructures in the development of science and technology, is undeniable. Specifically, the research on low-dimensional nanostructures has been colossal. While, on one hand the technology market is on a whirlwind of production of integrated circuits scaled down to orders of nanometers, there is increasing research on replacing the existing materials with new ones to endure the device scaling without compromising the functionalities. While the directory of these materials on this list is quite large, however there are quite a few of them which have received an enormous attention owing to their structural and materials properties. The main thrust of this thesis is to bring into picture some optical properties of these materials with specific morphologies and certain surface treatments and discuss their underlying physics. In this chapter is discussed the research motivations and objectives and a layout of the structure of this thesis.

1.1 Semiconductor Nanowires

Nanomaterials can be visualized as the bridge between a single molecule and an infinite bulk system. Different kinds of nanostructures like nanoparticles, nanowires, nanotubes, quantum dots, either as individual structures or superlattices or arrays have been of great interest to science and technology. These structures have properties different from their bulk counterparts. While different types of nanostructures have different applications for which they are being studied, amongst them nanowires are unique 1-D structures. They play an important role as active components and interconnects in nanoscale devices [1]. The other applications of nanowires are widespread and includes transistors [2,3], sensors [4,5], switches [6,7], lasers [8,9] etc. Availabilities of different synthesis techniques

have facilitated the growth of research in several domains involving nanowires. Among them the bottom-up approach is believed to be a great method for the synthesis of the 1-D nanostructures specially keeping in mind the latest scaling down of integrated circuits [10]. This bottom-up approach is conceivable by employing the Vapor-Solid-Liquid (VLS) mechanism as introduced by Wagner and Ellis by growing Si whiskers [11]. This method gives a great control and flexibility over the growth process and hence is used widely for the synthesis of nanowires. These 1-D materials, nanowires, nanofibers and nanoribbons, with unique electrical and optical properties are the main nanostructure materials that have been discussed in this thesis.

1.2 Wide band gap materials

Materials like Gallium Nitride (GaN), Silicon Carbide (SiC) are a natural fit to the devices requiring faster speed, smaller dimension, high temperature susceptibility and high voltages as compared to the Si-counterparts [12, 13]. Another interesting application of wide band material like GaN is as solid-state lighting devices. It is a great replacement to the traditional incandescent bulbs since this GaN based LEDs are not only energy efficient but has a longer lifetime. So, what is a typical wide-band gap material? They are materials having band gap energy larger than that of a conventional silicon. Band gap energy is defined as the energy gap between the valence band and conduction band of that material. Under electrical or optical excitation, electrons from the valence bands can be excited to the conduction band. While for a metal the valence band and the conduction bands overlap, for insulator the band gap is huge. Thus, metals have partially filled overlapping bands that allows movement of electrons making them an excellent candidate for conductors. For insulators, a considerable energy is required to transfer electrons from one band to other. Which is why we are mostly interested in

semiconductors. In case of semiconductors the amount of energy required to transfer electrons between valence band and conduction band is relatively smaller. Materials with wide band gap like GaN and ZnO has been widely studied in the past and is still being explored for several potential applications and their eventual commercialization. Figure 2 shows a list of materials which are widely studied along with their band gap values.

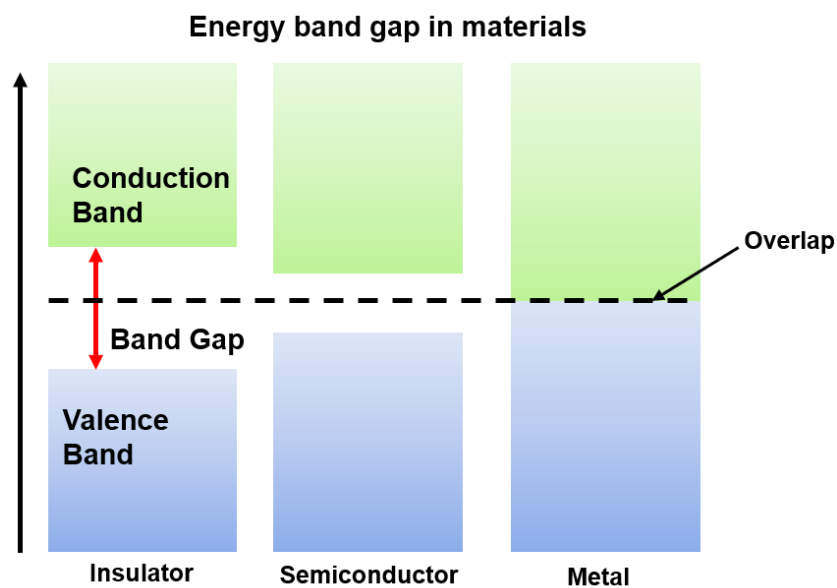


Figure 1 Energy band diagram of insulator, semiconductor and metal

Semiconductor Materials		
Material	Chemical Symbol	Bandgap Energy (eV)
Germanium	Ge	0.7
Silicon	Si	1.1
Gallium Arsenide	GaAs	1.4
Silicon Carbide	SiC	3.3
Zinc Oxide	ZnO	3.4
Gallium Nitride	GaN	3.4
Diamond	C	5.5

Figure 2 List of some widely studied materials with their band gaps

ZnO is a very interesting material with wide applications in optics, photonics and electronics. The most interesting feature of ZnO is its wide band gap ($\sim 3.37\text{eV}$) and a high excitonic binding energy of 60 meV at room temperature. Hence it is an excellent candidate for optoelectronic applications at shorter wavelengths [14]. Room temperature excitons are observed when their binding energy is larger than 25 meV. Photoexcited electron hole pairs are held together by strong Coulomb attraction to form these excitons. Due to low value of electron and hole effective masses, mostly in semiconductors the binding energies are generally $\sim 1\text{meV}$ and generally exists below room temperatures. The large value of binding energy for ZnO thus provides a greater stability to excitons which is why it has got a better edge over GaN when it comes to optoelectronic devices with low cost

of production and better optical properties. One disadvantage however is the difficulty in p-doping compared to the nitrides.

GaN and AlN, both wideband gap ($\sim 3.4\text{eV}$ and $\sim 6.1\text{eV}$ respectively) materials on the other hand is suited for optoelectronic applications even having initial high cost of production. The answer to the widespread adoption of it in the lighting industries, lies in the fact that the devices are far more efficient, with a long lifetime and energy efficient. Another important application of GaN/AlN is in high-frequency and high-power devices like High Electron Mobility Transistors (HEMTs). GaN/AlN based transistors can not only work under high temperature conditions but also high voltages. This is why GaN/AlN based HEMTs were offered commercially since 2006 [15].

Although the wide band gap materials are gaining a lot of acceptances from several domains, however there are several manufacturing challenges that needs considerations. For example, the substrate size and cost for these kinds of devices needs to be checked, alternate designs and packaging materials are needed for withstanding temperatures of these wide band gap materials based devices. System integration using these materials is also not easy, especially drop-in replacement of Si based devices. Hence a better innovative approach to design and manufacturing using wide band gap materials is always warranted.

1.3 Research Objectives

In the previous sections the background of the materials and structures that have been studied and presented in this thesis have been discussed. This section aims to highlight the main purpose of those studies. As mentioned earlier, ZnO has been one of the highly studied semiconductor material over the last few decades owing to its wide band gap of 3.37eV and large excitonic binding energy of

60meV. There have been some outstanding and pioneering work done on ZnO by several scientific groups specifically demonstrating its intriguing properties in different the applications which includes but not limited to FETs [16], chemical and biosensors [17], nanoresonators [18], light emitting diodes [19] etc. More research with the improvement and optimization of the physical properties of the materials and thereby a better approach to the applications is still useful. Most of the research concentrates on the growth, fabrication [20-23] while the emission properties of ZnO, the optical properties of ZnO nanowires pertinent to lasing are also investigated [24, 25]. Also, there have been several separate reports on the improvement of the emission from ZnO using different techniques [26-28] and study of the carrier dynamics under different high-density photoexcitation conditions [29, 30]. The necessity of a study analyzing the carrier dynamics of ZnO structures which are subjected to different surface treatments is undeniable. 1-D nanostructures like nanowires owing to their large surface to volume ratio on being converted from bulk to nanometer dimension, contains surface states which largely affects its PL properties. This is the reason, there have been reports on the observance of surface states related exciton emissions from ZnO nanostructures [31, 32]. Visible emission observed from these nanostructures are attributed to these surface states and sometimes to the oxygen vacancies introduced during the growth process [33-35]. The presence of these surface states or traps also affects the near-band-edge emission (NBE) significantly. These surface states thus need to be studied and treated carefully to successfully integrate and optimize a ZnO nanostructure based optoelectronic device. Different surface modification techniques have been reported which have technically been able to reduce the visible emission and enhance the UV emission considerably. Whatever be the kind of techniques applied, the basic principle remains the same. Removal of surface states implies removal of the non-radiative recombination centers which otherwise acts as an

alternative pathway thus quenching the visible emission peaks and enhancing the NBE peak. Doing a detailed analysis on the carrier dynamics of these surface treated ZnO nanostructures is required because no such detailed probing has been done before on the same report. Another interesting approach to the study of these optical properties of ZnO is to investigate the effect of the above-mentioned surface treatments on the lasing properties. As discussed earlier, ZnO has a great ability to grow into different kinds of structures depending on the growth conditions of the temperature and the vapor pressure. This brings up the question related to the context on how the different morphologies will influence the lasing. Change in dimension changes the ratio of surface to volume which in turn determines the density of surface traps on these structures. This would affect the recombination dynamics including the threshold and efficiency of stimulated emission from these nanostructures. One of the main research objectives of this thesis has been investigating all the changes in dynamics under the influence of surface treatments and a follow up with a study on the improved lasing properties including the effect of structure and size on the amplified spontaneous emission.

In_2O_3 is another interesting material which when doped with metals like Sn or Zn has been found to be great candidate for electrical and optical applications [36, 37]. While there are reports on low concentration doping of these metals into In_2O_3 [38, 39], no such studies have been found so far on highly doped In_2O_3 nanowires. In an attempt to highly dope the as grown indium oxide nanowires with Zn, a completely different outcome was observed in the form of an ensemble of both In_2O_3 and ZnO nanostructures grown on the same substrate. It is interesting to analyze these resultant nanostructures through different structural and optical characterizations and deduce the physical meaning which is what has been presented here.

One of the main properties of a crystal or a heterostructure is lattice vibrations which results in the fluctuations of the periodic potential to the lattice. Presence of heterointerfaces in structures which are low in dimension like superlattices results in the spatial restrictions of the lattice vibrations. This in turn leads to the re-normalization of the phonon spectra and effects the phonon-assisted processes like the confinement of the phonon modes and removal of heat [40-42] in confined structures; reduction of interface related processes in a metal-semiconductor heterointerface [43], an increase in the effect of interface phonon modes in scattering of electron-phonon [44] etc. Although phonons in the low dimensional heterostructures have been investigated over a long time, what is aimed in this thesis is specific to the optical phonon modes of a very short period AlN/GaN superlattice.

There is no doubt in the fact that AlN/GaN base HEMTs is an important area for the research community. Optimizing the structure is the preface to the commercialization of an efficient device. There are several aspects that need to be considered while designing these structures. For development of high power devices, which are the main field of applications of these wide-band gap materials, it is important to understand the dynamics of a high-density system. Different studies have highlighted various heterostructures with different thickness of the layers keeping the underlying principle same [45, 46]. What is aimed in this study is to understand the behavior of a very short period superlattice under the impact of high-excitation and high-temperature, both of which are the operating condition of high power devices.

1.4 Dissertation Outline

This thesis has been divided into 6 main chapters excluding the introduction and conclusion. These sections briefly highlight the work done on the research topics of the corresponding chapter.

Chapter 2, discusses about all the experimental set-ups that have been used in course of this dissertation work. It describes the CVD growth furnace at the Nanotechnology Core facility at University of Illinois, Chicago, used for growing different nanostructures using vapor-liquid-solid growth mechanism. Different optical characterization tools and methods have also been described in detail. These include Raman spectroscopy and Photoluminescence spectroscopy set-up at the Nano Engineering Research Laboratory (NERL), the Renishaw Raman, pump-probe spectroscopy and streak-camera detector system at the Center for Nanoscale Material Division (CNM) at the Argonne National Laboratory (ANL).

Chapter 3, focuses on the improved carrier dynamics of ZnO nanostructures after being subjected to different surface treatments. Two different surface treatment techniques namely Ar-plasma etching and Sputter coating with Au metallic nanoparticles have been discussed. The resulting improved emission after these surface treatments, have been shown and explained including the underlying physics. Transient absorption spectroscopy measurements have been provided showing a comparative study of the carrier dynamics before and after the surface treatments.

In Chapter 4, the effects of surface treatments and morphology on the simulated emission and consequently on the lasing from ZnO nanostructures have been discussed. Different ZnO nanostructures grown using VLS process were subjected to high-photoexcitation. Amplified spontaneous emission from these nanostructures which vary in shape and size were investigated.

Furthermore, comparison of the threshold and efficiency of lasing from surface treated and as-grown ZnO nanostructures has been discussed and analyzed.

Chapter 5, discusses on different structural and optical characterization techniques employed to identify and understand the nature of nanostructures grown through an attempt of highly doping In₂O₃ nanowires with zinc. The co-existence of both In₂O₃ and ZnO nanowires on the same platform were observed instead of formation of any highly Zn doped In₂O₃ nanowires. This has been established by different characterization techniques including TEM, EDX, PL and Raman spectroscopy. These nanowires were randomly oriented as confirmed by the quasi-phonon modes using Loudon's model of uniaxial crystals.

Chapter 6 studies the optical phonon modes of a very short period AlN/GaN superlattice under back scattering geometry. Assessment of different phonon modes obtained from the Raman spectra has been done by literature review and theoretically obtained phonon dispersion curve specific to the short period lattice, using Dielectric Continuum Model. Temperature calibration for $E_2(\text{high})$ and $A_1(\text{LO})$ mode was obtained using Raman spectroscopy and compared theoretically using Bose Einstein Statistics.

Chapter 7, discusses the effect of high photo-excitation and high temperature on the short period AlN/GaN superlattice. It also highlights how the power density has a role to play in the penetration depth by analyzing the individual peaks obtained from the PL spectra. Dependency of carrier temperature on the laser excitation density has been studied as well. Finally, the radiative recombination model was utilized to study the nature of the emission from the superlattice at elevated temperatures.

The schematic outline of the organization of the thesis is presented in presented below:

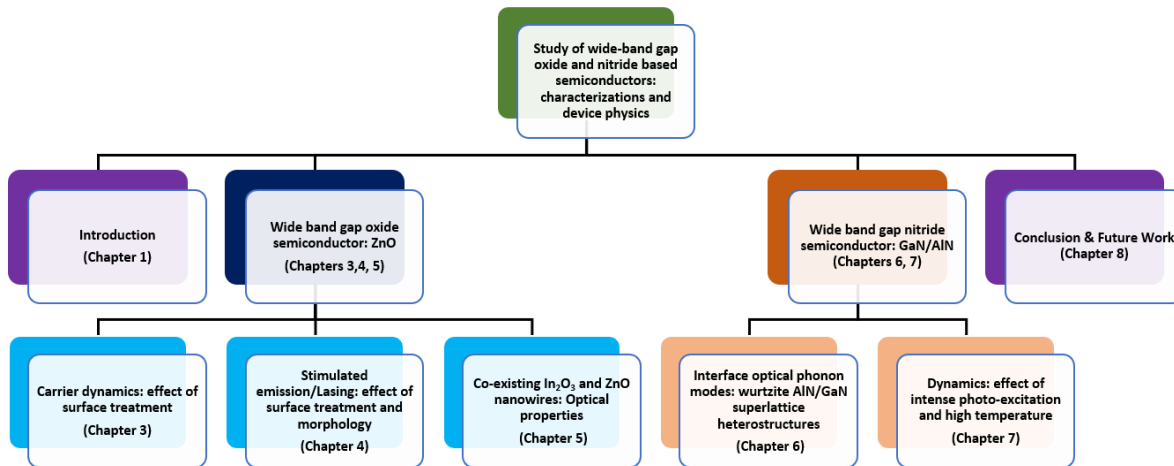


Figure 3 Schematic outline of the thesis

2. OPERATING PRINCIPLE AND EXPERIMENTAL SET-UP

2.1 Overview of the chapter

In this chapter, is discussed all the important setups and their operating principle, which have been used to achieve the experimental data that are presented in this thesis. It starts with the simple CVD growth setup at the Nanotechnology Core Facility at the University of Illinois-Chicago (UIC) which was primarily used to grow the semiconductor nanostructures under atmospheric pressure. Also, is discussed the VLS (Vapor-Liquid-Solid) mechanism for the growth of nanowires using this CVD furnace. Next is discussed the Photoluminescence spectroscopy set up at the Nano Engineering Research Laboratory (NERL) at UIC. It is a very useful technique to study the electronic structure of a material. This has been used to observe all the allowed optical transitions in the near band gap and mid gap energy levels. Almost a similar set up was used but with a different principle of operation for the Raman spectroscopy measurements at NERL, UIC. The main purpose of Raman spectroscopy is to study the optical phonon modes for understanding vibrational or lattice properties of the materials. Pump-probe spectroscopy set up at the Center for Nanoscale Material Division at the Argonne National Laboratory, used for studying the carrier dynamics of the nanostructures by probing at different wavelengths has also been discussed. It is a two-dimensional spectroscopy method which is used to extract both the temporal and spectral information of a material. Finally, is discussed the streak camera detector system which are mainly used in applications like time-resolved spectroscopy. It operates by converting the temporal variation of a light pulse into spectra profile from which several properties can be inferred.

2.2 Chemical Vapor Deposition (CVD) growth furnace

Growth of a specific nanostructure by CVD requires a set up with a temperature controlled furnace to control the growth temperature, an inert gas cylinder which will be the source of the carrier gas, a flowmeter controlling the flow rate of the gas, a vacuum system if and when necessary to pump down the pressure to a low value, a quartz tube to be placed inside the furnace for holding the growth materials and finally a proper exhaust line to vent out the downstream gas resulting from the growth process. Below is shown the picture of the CVD furnace at NCF, UIC which has been used for growing various ZnO and In₂O₃ nanostructures. The components have been labelled for reference.

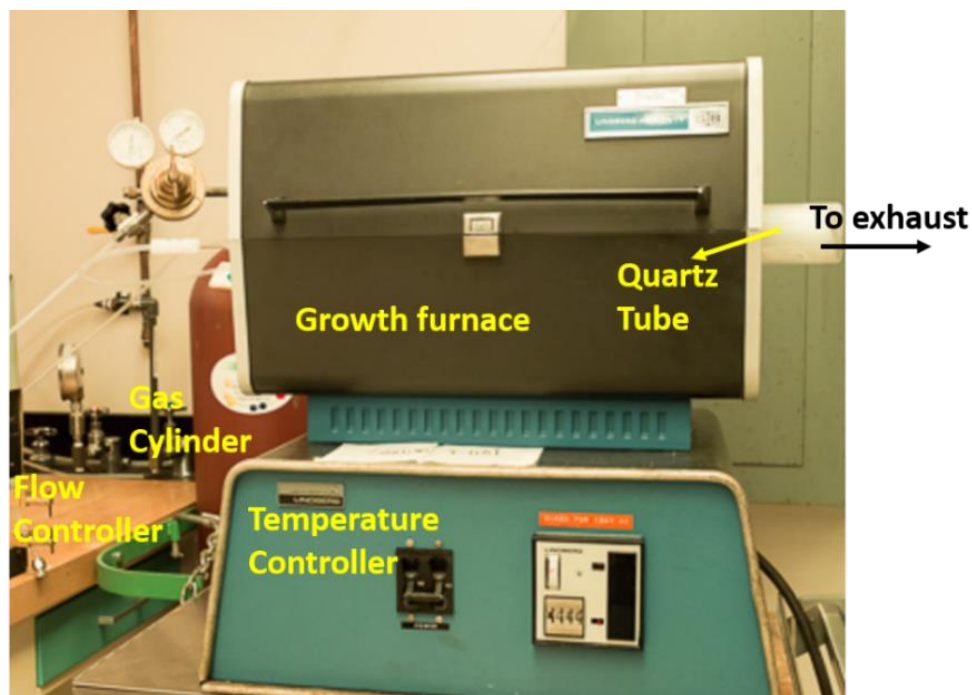


Figure 4 Growth furnace set up at Nanotechnology Core Facility, UIC

Figure 5, shows the schematic of the growth set up specifically showing the inside of the quartz tube. As can be seen from the figure, the source material is placed exactly at the center of the furnace on a quartz boat. Downstream of the tube is placed another small quartz boat with the growth substrates. This is a vapor based technique, hence requires high temperature to vaporize. This is the reason, it is always recommended to use materials like quartz for both the tube and the boats which can withstand the high temperature. The flow rate of the gas is directly proportional to the cross section of the tube. Hence, it is important to keep in mind the diameter of the tube while controlling the flow rate of the carrier gas. The other growth parameters that are equally important and should be carefully controlled to optimize good growth condition are growth time, growth temperature, distance between the source material and substrate. The growth temperature and growth time can be controlled by programming the temperature controller accordingly. The exact location of the substrate with respect to the quartz boat containing the growth powder precisely determines the deposition temperature and vapor pressure. Hence, it is important to control this distance to achieve the specific nanostructures.

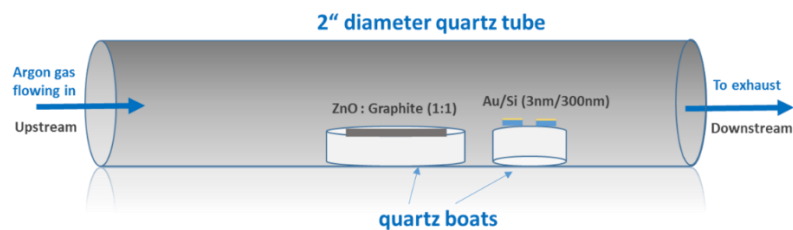


Figure 5 Schematic diagram of the inside of a quartz tube containing the growth precursor and growth substrates

The growth process which takes place to result in the formation of the nanostructures that have been studied in this thesis is the vapor-liquid-solid mechanism. It is a gas-phase reaction where the growth of an anisotropic crystal is promoted by the presence of a liquid alloy-solid interface. Figure 3. shows the flow diagram for the growth process utilizing VLS mechanism. It is known that the eutectic temperature to form a liquid alloy of Si and Au is 363°C [47]. The surface of this liquid alloy has a large coefficient of accommodation. Hence, it is always a favorable site for the deposition of the incoming vapor of the growth powder. Once this liquid alloy becomes supersaturated with the incoming vapor, precipitation occurs at the interface of solid-liquid to form the nanostructure.

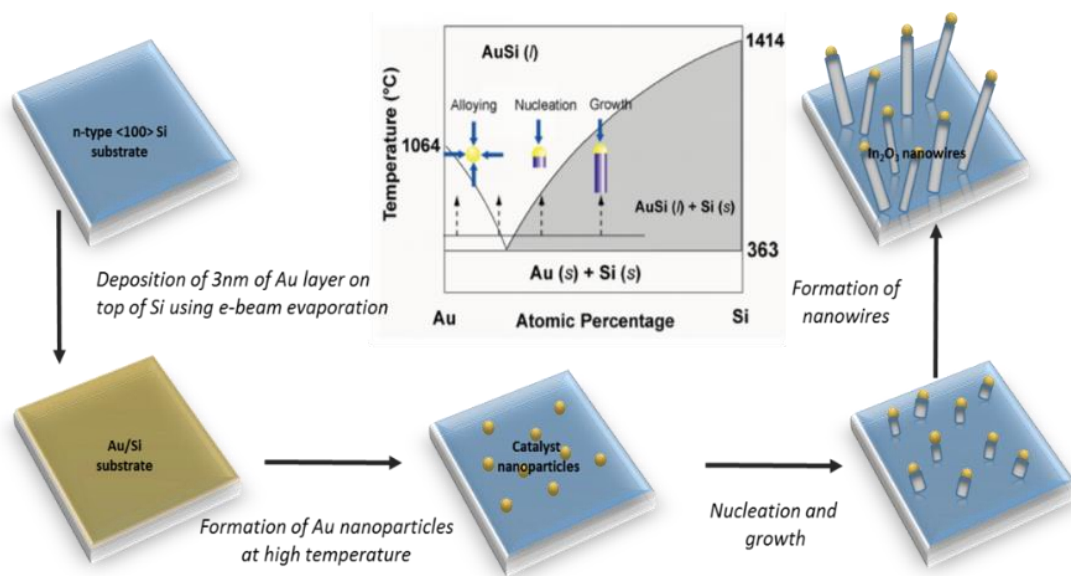


Figure 6 Flow diagram for the growth of nanowires on an Au coated Si substrate. Au acts as the catalyst for the growth

2.3 Raman spectroscopy

Raman spectroscopy is one of the most interesting and insightful technique in the field of optics to identify a molecule by investigating its vibrational, rotational and other modes of frequencies. This spectroscopy is named after famous Dr. C. V Raman who was the first to observe of the scattering of light and the discover the Raman effect [48] for which he was later awarded the Nobel Prize.

Raman spectroscopy depends on what is known as the Raman scattering or the inelastic scattering. More elaborately, when a sample is illuminated by a laser source of known wavelength and frequency, the electromagnetic radiation from the laser spot interacts with the bonds of the molecule or lattice vibration. This can scatter the photon inelastically. This inelastically scattered photon can have energy either more or less than the incoming energy of the photons. This change causes the frequency of the photon to shift to conserve the energy of the system. We will observe a shift to a higher frequency for the scattered photon in case the final energy is larger than the initial energy. This is known as the anti-Stoke shift. On the other hand, if the final state energy is smaller than the initial energy state, then the scattered photon will shift to lower frequency (Stokes shift) to conserve the total energy of the system. This is depicted in figure 7, which shows separately the Stokes and anti-Stokes shift for a Raman scattering/inelastic scattering.

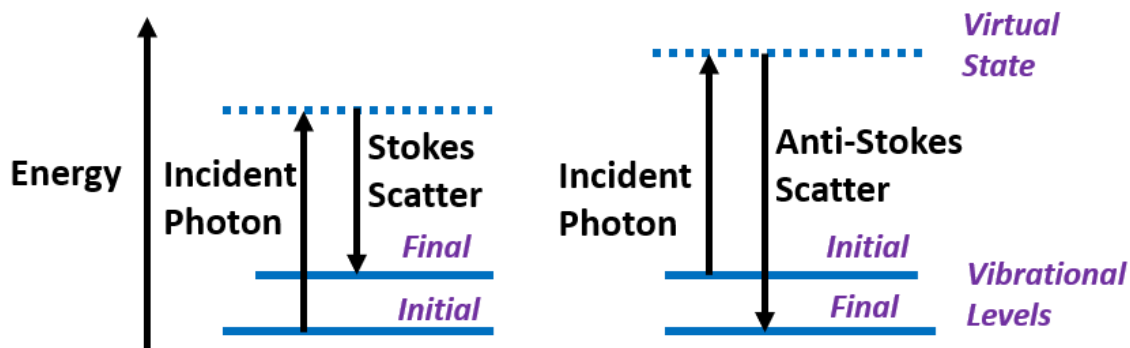


Figure 7 Raman scattering showing both Stokes and Anti-Stokes lines

The schematic of the Raman set-up is shown in Figure 8. All the Raman measurements were done using a back-scattering geometry. An Action SpectroPro-2500i spectrometer containing a triple grating monochromator was used for the measurement of the Raman signal. This spectrometer has three gratings are placed on a rotating turret and can be chosen from the control software which is interfaced with the system. The three gratings are 1200 grooves/mm, 2400 grooves/mm, and 3600 grooves/mm. The detector shown in the figure is a one from Roper Industries. It is a liquid cooled CCD detector and is operated at temperatures -115°C and below as recommended. The optical source used for the Raman measurement is the continuous wave He-Cd laser with a wavelength of 441.6nm. A notch filter is used to filter the laser line from the Raman spectrum.

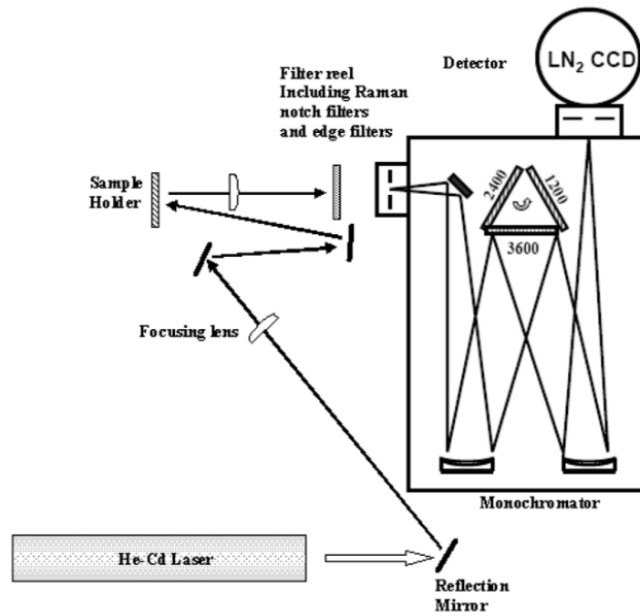


Figure 8 Schematic diagram of the Raman system at Nano Engineering Research Laboratory, UIC

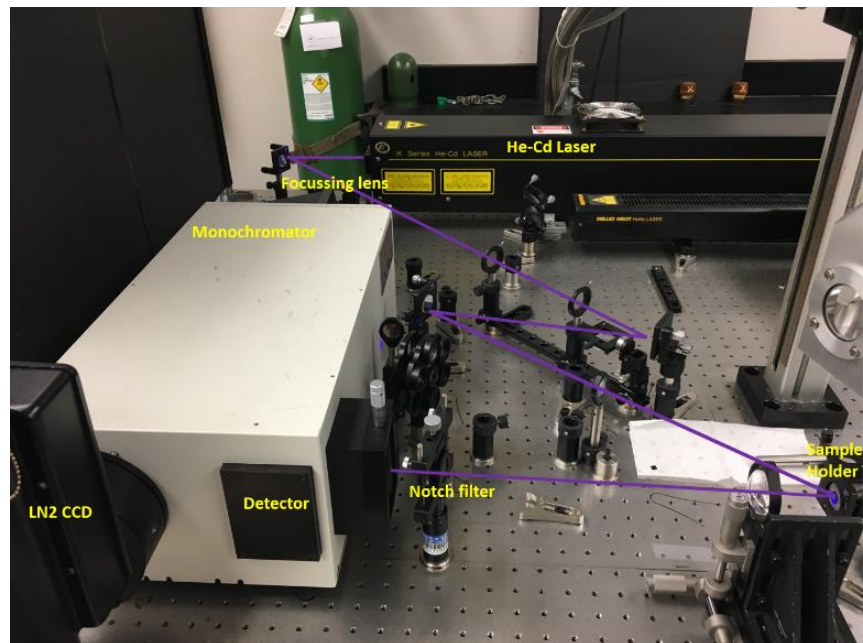


Figure 9 Raman/PL set-up at Nano Engineering Research Laboratory, UIC

Some of the Raman measurements were also done at the CNM division at Argonne National Laboratory. While the principle of operation remains the same, the setup used there was a compact fully automatic Renishaw inVia Reflex Raman system which was integrated with a temperature controlled stage used for high/low temperature Raman measurements. The laser source used was a 514nm green laser.



Figure 10 Renishaw inVia Reflex Raman system at Centre for Nanoscale Materials in Argonne National Laboratory

The Renishaw is a confocal microscope. It is coupled with a Raman spectrometer. A laser source is used for the system which is directed through the beam shaping optics and the objective of the microscope before hitting the sample. The scattered Raman photons are collected by the objective of the microscope before directing to the gratings. There are 3 gratings to choose from, 1200 lines/mm,

1800 lines/mm or 2400 lines/mm. The Raman scattered photons are then finally deflected to the Liquid N₂ CCD detector. Once inside the monochromator, these photons are deflected by the gratings. The amount of deflection is different for each frequency values. The inVia Reflex system contains different objective lens which can be varied to change the lateral resolution. The system is interfaced with the computer using the WiRE™ software which gives an efficient and effective way of controlling and operating the system.

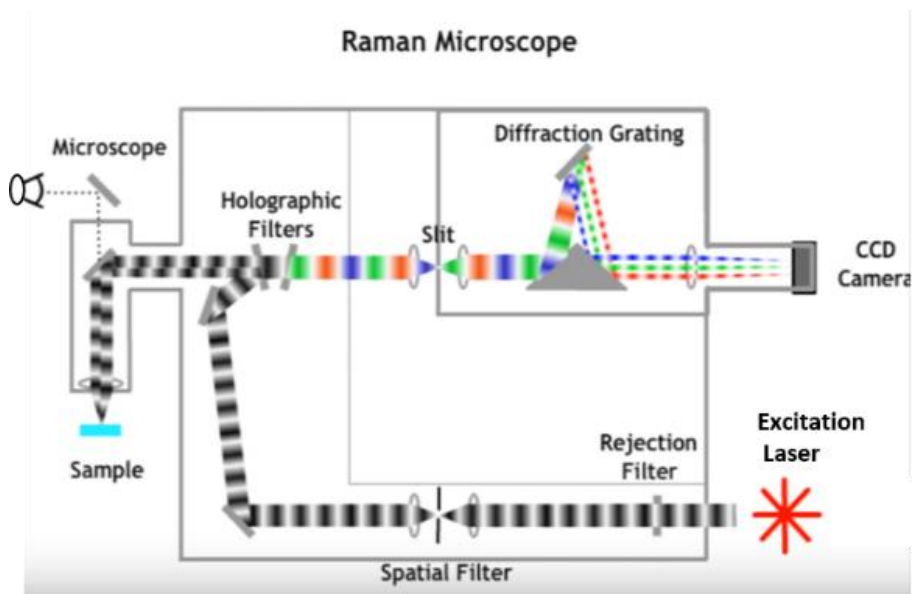


Figure 11 Renishaw inVia Reflex Raman system at Centre for Nanoscale Materials in Argonne National Laboratory

2.4 Photoluminescence spectroscopy

Photoluminescence spectroscopy is the process of emission of light by absorbing photons from the incident photoexcitation. It is not only a contactless method, but also non-destructive to the sample and can be used to extract the electronic structure of the material. Indeed, PL is one of the most important optical characterization technique for any semiconductor. When the energy of the photoexcitation is greater than the energy of the band gap, it causes electrons from the valence band to jump into the conduction by absorbing the incident photon energy, leaving behind holes in the valence band. These electrons then return to the equilibrium state by releasing the excess energy either in form of radiative recombination or non-radiative recombination as shown in Figure 8. PL can be therefore utilized to determine the band gap, detection of defects levels or any kind of electron-phonon interaction. In this thesis, there has been several reports on PL studies which was primarily used to observe any near-band-edge emission and/or visible emission peaks resulting from oxygen vacancies or surface defects.

Figure 9 shows the experimental set-up of PL experiments at NanoEngineering Research Laboartory at UIC. The laser from the He-Cd source travels through focusing lens and mirrors before exciting the sample. The detailed description of the setup has been explained in the previous section 2.3.

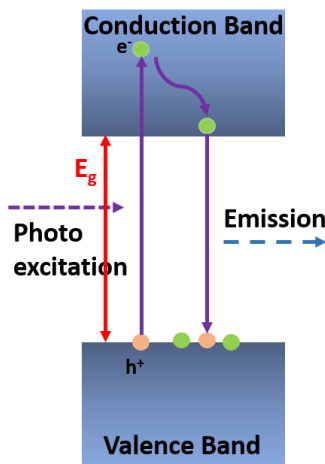


Figure 12 Mechanism of Photoluminescence

2.5 Pump-probe spectroscopy

Pump-probe spectroscopy is a powerful technique to probe and characterize the structural and electronic properties of the transient excited state of any material. It has two laser pulses-pump and probe. While the pump pulse is used to induce perturbation in the sample by photo-excitation, the probe pulse investigates the resulting change in the optical properties. Since, the probe pulse is a very narrow pulse (~femto-second), it is easier to get a very good temporal resolution. Once the probe pulse has interacted with the sample after being excited by the laser, it is measured using the detector. This gives us an accurate measurement of the changes induced due to the photo-excitation. It is a 2-dimensional spectroscopy technique since we get spectra at different time delays and kinetics at different wavelengths.

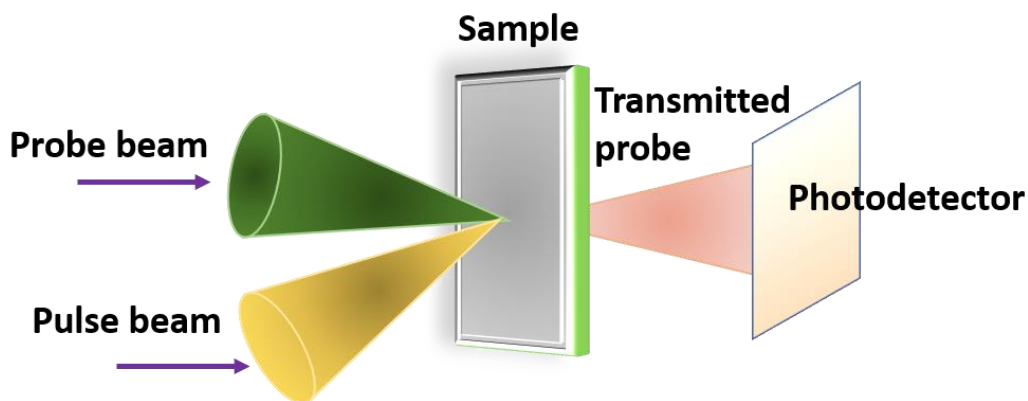


Figure 13 Schematic of the pump-probe spectroscopy

In figure 14, is shown the schematic diagram of the experimental setup of a pump-probe spectroscopy system at Argonne National Laboratory used for the measurement of transient absorption spectroscopy. Initially two green lasers are fed into an oscillator (Tsunami) and an amplifier (Spitfire). The output of Tsunami is an 800nm, 120fs pulse (energy \sim nJ) with a repetition rate of 75MHz. While the output of the Spitfire is another 800nm, but 100ns pulse (energy \sim mJ) with a repetition rate of 5KHz. These two pulses are mixed in an optical switch which contains a polarizer that switched between two polarizations leading to either trapping the weaker signal or transmitting it. While trapping, the weak signal goes through the chamber (multipass) which draws energy from the stronger signal each time during the pass. Finally, what we get out the optical switch is an 800nm, 120-160fs pulse with a repetition rate of 5KHz., i.e. very narrow pulses with high energy and low repetition rate. 90% of this pulse is used to drive an Optical Parametric Amplifier (Topaz), which contains a mixer and two crystals and can generate optical pulses on a wide wavelength range. In our case, an output of 325nm was generated. This is further sent through an optical chopper that chops every alternate signal, such that the outcoming pulse has a repetition rate of 2.5KHz. Finally, the pulses are attenuated

by a neutral density filter before exciting the sample under test. The other 10% of the signal, goes through a variable delay track before mixing with the sapphire crystal (white light continuum) or calcium fluoride (UV) and finally probing the sample.

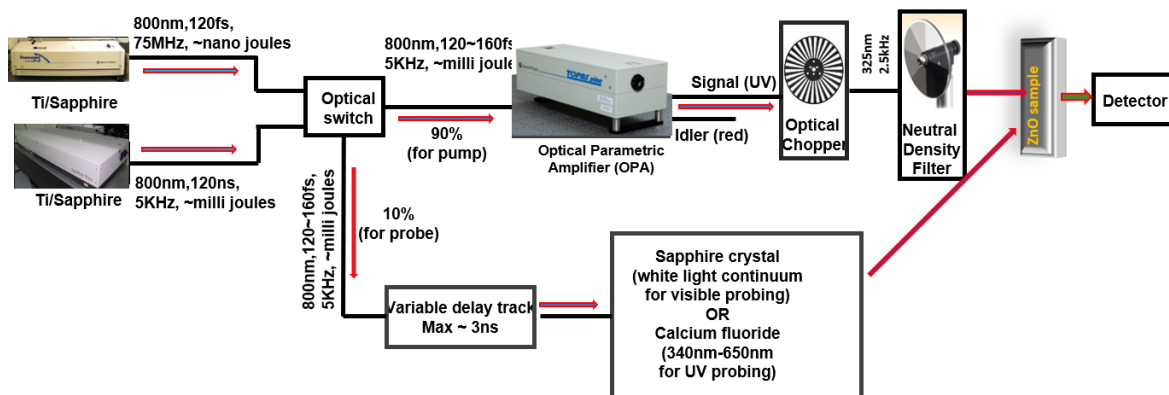


Figure 14 Experimental setup of a pump-probe spectroscopy measurement at ANL in CNM

2.6 Streak Camera Detector/Time-resolved photoluminescence

Streak camera is a device used for converting temporal variation to spectral profile and is used for the measurement of ultra-fast light phenomenon. Time variation of the intensity of a light pulse with respect to wavelength as well as position can be detected using such a system. In figure 15 is shown the operating principle of a typical streak camera system. A train of femtoseconds laser pulse acts as the source of the streak camera system. The photons are then spatially separated according to their wavelength by using a diffraction grating. These photons are incident on a photocathode and are then converted to electron. These electrons pass through an accelerating mesh. A pair of high voltage electrodes initiates a high-speed sweep to these incoming electrons which are deflected at different angles onto the micro-channel plate before finally impacting the phosphor screen. This is where the

electrons are converted back to light. The distribution of brightness on the phosphor screen gives a measure of the spatial and temporal change in light intensity.

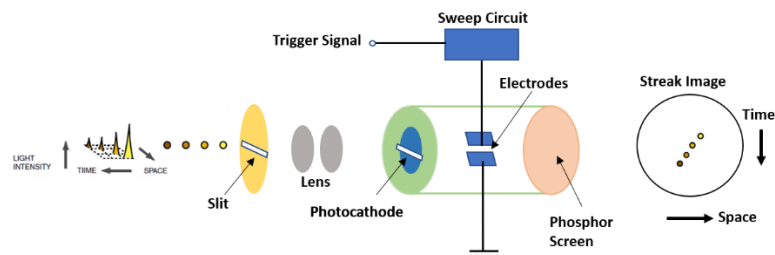


Figure 15 Principle of operation of a streak camera detector system

For the ultrafast time resolved measurements done at Argonne National Laboratory an ultrafast Ti:Sapphire laser and a Hamamatsu C5680 Camera system was used. The output of the laser was 150fs pulse at 325nm operating at a frequency of 2kHz. The photoluminescence spectra were resolved with respect to the wavelength using an Action SP2150 spectrometer while the same was resolved with respect to time using the streak camera having a photon counting detector. The latter was operated under the slow sweep mode. Baseline subtraction of dark counts in the streak camera system was done before exciting the sample. Spectral integration of the PL peak resulted in the time dependent photoluminescence signals.

2.7 Conclusion

The chapter provides a detailed description of the major experimental setup that was used for synthesis and characterization of different oxide and nitride based semiconducting materials. This information is provided to have an insight into the experimental processes and data and for future reference.

3. STUDY OF ULTRAFAST CARRIER DYNAMICS OF ENHANCED NEAR-BAND-EDGE EMISSION FROM ARGON-PLASMA TREATED ZINC OXIDE NANORIBBONS

(Portion of this chapter is copied from my submitted manuscript)

“Ultrafast carrier dynamics and optical pumping of lasing from Ar plasma treated ZnO nanoribbons”, Ketaki Sarkar, Souvik Mukherjee, Gary Wiederrecht, Richard D Schaller, David J Gosztola, Michael A Stroscio and Mitra Dutta, *submitted to Nanotechnology*)

3.1 Overview of the chapter

It is well-known fact that ZnO has been one of the highly studied wide bandgap II-VI materials by the scientific community specifically due to its potential in being used as exciton-related optical devices. Hence, realizing ways to increase the efficiency of these devices is important. We discuss a plasma treatment technique to enhance the near-band-edge (NBE) excitonic emission from ZnO based nanoribbons. We observed an enhancement of the NBE peak and simultaneous quenching of the visible emission peak resulting from the removal of surface traps on these ZnO nanoribbons. More importantly, we report here the associated ultrafast carrier dynamics resulting from this surface treatment. Femtosecond transient absorption spectroscopy was performed using pump-probe differential transmission measurements shedding new light to these improved dynamics with faster relaxation times. The knowledge obtained is important for improving the application of ZnO based opto-electronic devices.

3.2 Background of surface treatment on ZnO nanostructures

Different two-dimensional (2-D) and one-dimensional (1-D) nanostructures have stirred a great deal of interest in the scientific research owing to their novel electrical and optical properties. However,

the synthesis of these low-dimensional nanostructures from their bulk materials, introduce surface states or defects during the growth process, which enhances the non-radiative recombination by surface-mediated trapping thereby affecting its photoluminescence [49]. It is thereby important to improve the structural and optical qualities of these nanostructures for high performance device applications by the removal of these surface states.

ZnO, an interesting material with a large band gap (3.7 eV) and high excitonic energy (60 meV) at room temperature is an excellent candidate for opto-electronic devices [50-52]. Significant improvement in the near-band edge emission and removal of deep level emissions of ZnO has been previously achieved either using plasmon-mediated approach by sputter coating the nanostructures with different metals [53, 54] or surface passivation by plasma-assisted etching [26]. Argon ion milling [27] and polymer covering [28] are the other surface treatment methods that have also improved the PL by increasing the near band edge emission and simultaneously decreasing the visible emission. Although these reports have successfully demonstrated the improved optical emission from different ZnO nanostructures, what is presented here is the comparison of two different treatments on the same type of ZnO nanostructures and thereby analyze the advantage of one over the other.

We report on the post-growth surface treatment using Ar plasma on the as grown ZnO ribbons and analyzed its effect on the carrier dynamics of these plasma etched ribbons using pump-probe spectroscopy. Improved crystal qualities due to etching resulted in a faster relaxation towards equilibrium. These etched structures were further optically pumped for lasing using a streak-camera detector system. Improved material quality due to surface treatment resulted in lower random lasing threshold and highly efficient stimulated emission. In each of these cases, we have aimed to provide a comparison of the optical characteristics of the ZnO nanoribbons both before and after plasma etching treatment.

3.3 Experimental details

ZnO nanoribbons were synthesized by using the vapor transport mechanism in a home built Chemical Vapor Deposition (CVD) furnace. A mixture of high purity ZnO powder (99.999% Sigma Aldrich) and graphite powder with a mass ratio of 1:1 was used as the source material. This mixture in a quartz boat was placed at the center of a 2'' diameter tubular furnace as shown in figure 1. Another quartz boat containing the 5nm gold coated Si substrates was placed at the downstream of the furnace. The distance between the source and substrate was maintained at 2 cm. The furnace was heated at a ramping rate of 30 °C /min. Once the temperature reached 950 °C, Argon gas was introduced into the quartz tube. The growth time was maintained for 45 mins.

The morphology of the ZnO nanoribbons was analyzed using the Hitachi S3000N Scanning Electron Microscope (SEM). Raman measurements were done on the Raman Renishaw system using an excitation of 442 nm laser at room temperature in a back-scattering geometry.

Plasma treatment was performed in Ar atmosphere in a Hummer SEM coater system. The chamber pressure was pumped down to 30 mTorr. The mode selector switch was placed in "Plasma" mode. The etching was done by increasing the chamber pressure to 100 mTorr, with current set to 20 mA for 60 s. The same system was used for sputter coating with Au nanoparticles by keeping the mode selector switch to "DC plating" mode. The sample/Au target was used as the cathode in respective cases.

Photoluminescence spectroscopy (PL) was done using a 325 nm He-Cd excitation source. An ACTION SpectraPro spectrometer was utilized to analyze the scattered light from the ZnO nanoribbons. Transient absorption measurements were done using a pump probe spectroscopy setup. A regeneratively amplified Ti:sapphire laser (Newport Tsunami and SpitFire Pro) was used to generate both the pump and the probe pulse. The output of which is a 120fs pulse at 800 nm with a

5kHz repetition rate. 90% of this pulse was used to pump an Optical Parametric Amplifier (OPA: Newport TOPAS-C), the output of which was also a 120fs pulse at 325 nm. This served as the excitation source for our experiments. The remaining 10% of the pulse was passed down a variable delay line track before focusing onto a calcium fluoride crystal which generated a continuum probe pulse (340 nm-650 nm) for UV probing. A mechanical chopper synchronized with the regenerative amplifier was used to modulate the pump pulse at 2.5 kHz. This helps the spectrometer measure alternatively the probe transmittance, T_{on} and T_{off} , in presence and absence of the pump pulse respectively. A neutral density filter was used to vary the excitation energy of the pump pulse. For the optical pumping of laser, we used a streak camera system (Hamamatsu C5680) which was mounted on an Action SP2150 spectrograph. Photoluminescence measurements were done using a 35 fs amplified Ti:Sapphire laser (Spectra-Physics MaiTai oscillator and Spitfire Pro amplifier) at 325 nm which was operating at a rate of 2 kHz. The pulse energy was controlled using variable neutral density filter.

3.4 Results and discussion

3.4.1 Structural analysis of ZnO nanoribbons

In figure 16(a) is shown the SEM image of these as grown nanoribbons dispersed randomly on Si substrate. The length ranges from 100-150 μm . The width of the ribbons is typically between 2-5 μm , whereas, the thickness is around 200 nm. The random orientation of these as grown ZnO nanoribbons is also reflected in the Raman spectra shown in figure 16(b). Apart from the significant and strong E_2 high mode at 438 cm^{-1} , we observe another peak at 579 cm^{-1} . The Raman modes depends on the crystal orientation relative to the direction of propagation of light due to the crystal symmetry and the selection rules from the symmetry. Hence due to the random orientation of the ribbons, Raman scattering results in the quasi-phonon modes or mixed modes [55]. The frequencies of these mixed

modes have values intermediate between that of the pure A_1 and E_1 modes. The position of the peak at 579 cm^{-1} doesn't correspond neither to A_1 or E_1 modes, but to the longitudinal optical (LO) quasi-phonon modes of A_1 and E_1 . Mathematically these can be explained using Loudon's calculations and has been presented in detail in our earlier report [56]. We also observe another small Raman peak at 333.14 cm^{-1} . This mode is assigned to $E_2^{high}-E_2^{low}$ [57].

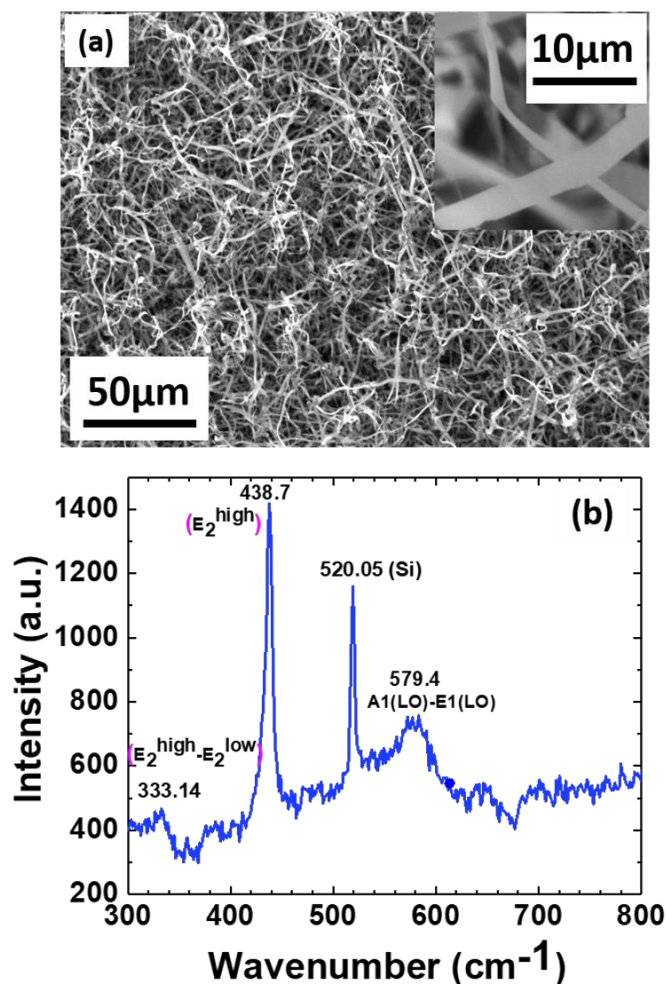


Figure 16 (a) SEM image of the randomly grown ZnO nanoribbons on Au coated Si substrate. The inset shows the SEM image of a magnified ribbon for better clarity of the thickness. (b) Raman spectrum of ZnO nanoribbons obtained using back-scattering geometry

3.4.2 Surface treatment of ZnO nanoribbons

The as-grown ZnO nanoribbons were subjected to two different types of surface treatments separately and the efficiency of were compared in terms of the emission properties of the ribbons. The two different types of treatments that were conducted were plasma etching using Ar and sputter coating with Au metallic nanoparticles. As mentioned earlier, the same setup was used for both the surface treatments. While the sample with ZnO nanoribbons served as the target during plasma etching, it was replaced with gold target in case of sputter coating. As the chamber is pumped down to a low pressure and Ar gas supply is turned on. As a live electrode is introduced into the low pressure Ar chamber thereby creating Ar plasma. These plasma ions with high energy then strike the target materials eroding the source material. In case of sputter coating, the target material Au releases neutral particles which when comes in contact with the sample and gets deposited.

3.4.3 Photoluminescence of surface treated ZnO nanoribbons

Figure 17(a) shows the PL spectra of these nanoribbons before and after the treatment with Ar plasma. The as grown sample shows a small near-band-edge (NBE) ultraviolet (UV) peak at 3.24eV and a large broad green visible emission peak centered at around 2.41eV. After the plasma treatment, we observe not only an enhancement in the UV peak but also quenching of the broad visible peak. Before analyzing these concurrent occurrences of the enhancement of the NBE peak and suppression of the visible peak, it is necessary to understand the origin of these peaks. While excitonic recombination results in the UV peak, there is no unanimous agreement on the exact nature of the visible emission. Due to the different surface to volume ratios for different nanostructures, spectral shifts in the visible range are expected owing to the different concentrations of defects on the surface of these structures. There has been quite a debate on the various attributions of the green visible peak. While several studies have cited singly ionized oxygen vacancies [34, 58, 59] to be the reason for the green emission,

there have been other hypothesis claiming zinc interstitials [60] and anti-site oxygen [61] as the root to the green emission in ZnO nanostructures. Whatever be the type of defects, the fact that surface treatments have been able to eradicate them, is a convincing indication that these defects are located mainly on the surface of these structures.

Upon photoexcitation of the as grown nanoribbon, the surface defects or the traps act as the alternate path for the recombination of the excited carrier. This results in the separation of electron-hole pairs, hence the exciton density decreases resulting in a weak NBE emission. The separated holes trapped by the surface states tunnel into defect centers in the mid-gap energy levels to optically activate the oxygen vacancies which emits the visible luminescence. The mechanism for the simultaneous occurrence of enhancement of NBE peak and quenching of the visible emission have been mainly attributed to the surface passivation by hydrogen resulting in the removal of the recombination centers in several reports [62, 63]. There could be a possibility of the incorporation of hydrogen either in the form of H₂ gas or moisture in our chamber due to increase in pressure from 30 mTorr to 100 mTorr. Under the high energy of plasma, this hydrogen molecule dissociates into H⁺ ion and diffuses into the ZnO. However, our sample is placed right in the path of the Ar plasma, hence there is a stronger possibility of collision induced removal of the surface traps. In either case, this plasma treatment results in the removal of these surface states, thereby increasing the density of excitons. Hence, we observe the enhancement of the UV peak. On the other hand, this also leaves behind less traps available for the capture of holes thereby reducing the visible peak.

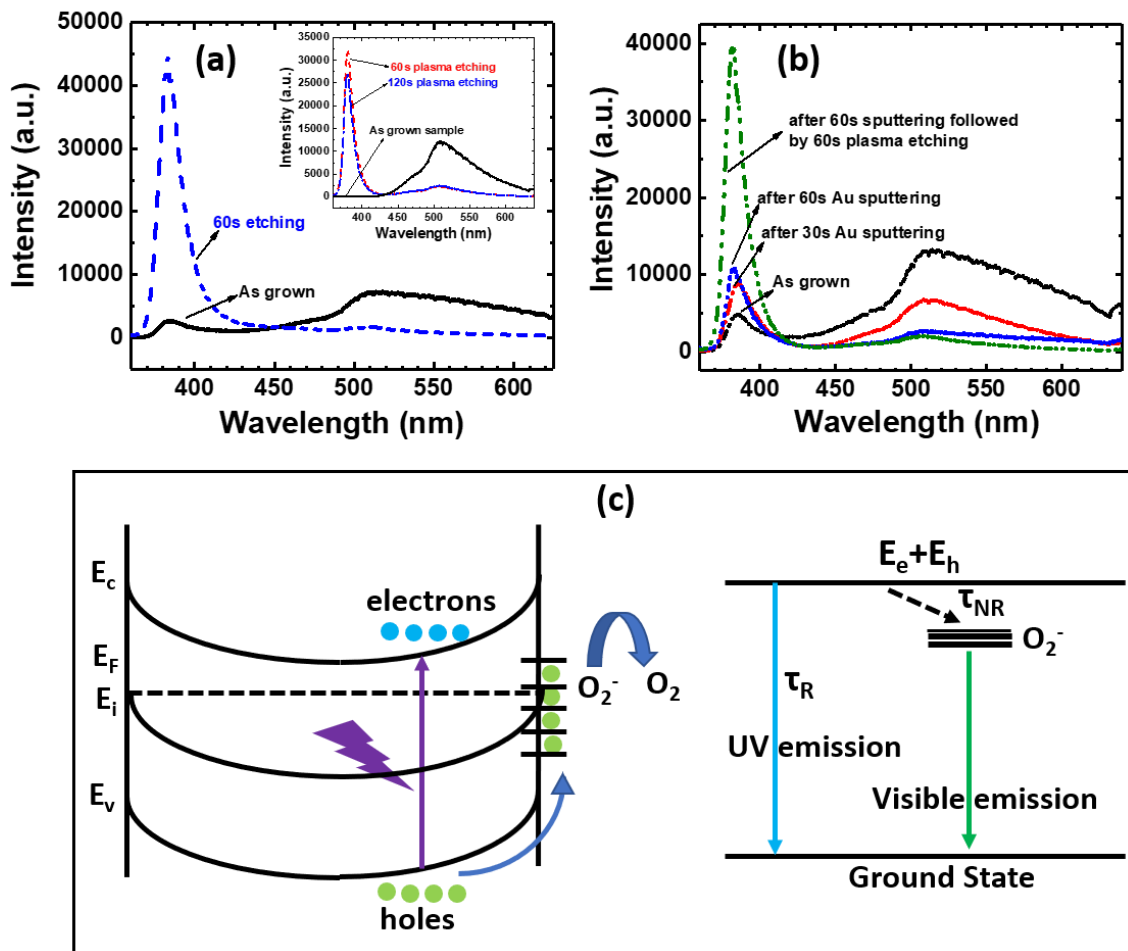


Figure 17 (a) Room Temperature PL spectra of the as grown and Ar-plasma treated ZnO nanoribbons. Removal of the surface states acting as the alternative de-excitation pathways resulted in the huge enhancement of the UV emission peak and simultaneous reduction in the visible emission peak. The inset shows the dependency of the UV peak intensity on the surface treatment time. Prolonged exposure of the nanostructures to the Ar plasma results in the degradation of the material quality. (b) Comparative plot of the room Temperature PL spectra before and after sputter coating the nanoribbons with Au metallic nanoparticles and Ar-plasma treatment. (c) Left image shows the energy band diagram of ZnO showing band bending and presence of surface traps. The right-hand side image shows the possible relaxation pathways for the carriers in ZnO.

The enhancement of the NBE peak and the suppression of the visible emission peak is dependent on both the energy of the plasma and the time duration of the plasma treatment. Since, the density of defects is different for different samples, hence the observed visible peak intensity is different in each case. The inset in figure 17(a) shows a sample with a large visible emission. However, by controlling the time for the surface treatment, it is possible to suppress the defect related emission to a large extent. On the other hand too much exposure to plasma is also detrimental for the material. Thus, increasing further the surface treatment starts to reduce the NBE peak. Hence, the exact reproducibility of the suppression of the visible peak is a function of the treatment time which in turn is proportional to the density of surface defects on the ZnO nanoribbons.

In figure 17(b) is shown the PL spectra of the ZnO nanofibers before and after sputter coating with gold (Au) metallic nanoparticles. This has been performed in the same set up where the Au metal target acts as the cathode instead of the sample itself unlike in the case of plasma etching. We observe that the relative enhancement in this case is comparatively less than that obtained by just plasma etching. This observation is similar to the earlier reported investigations [64, 65] on the effect of sputtering with metallic nanoparticles on the NBE PL indicating that the passivation of surface states plays a major role. There could be plasmonic effect leading to this enhancement due to sputter coating.

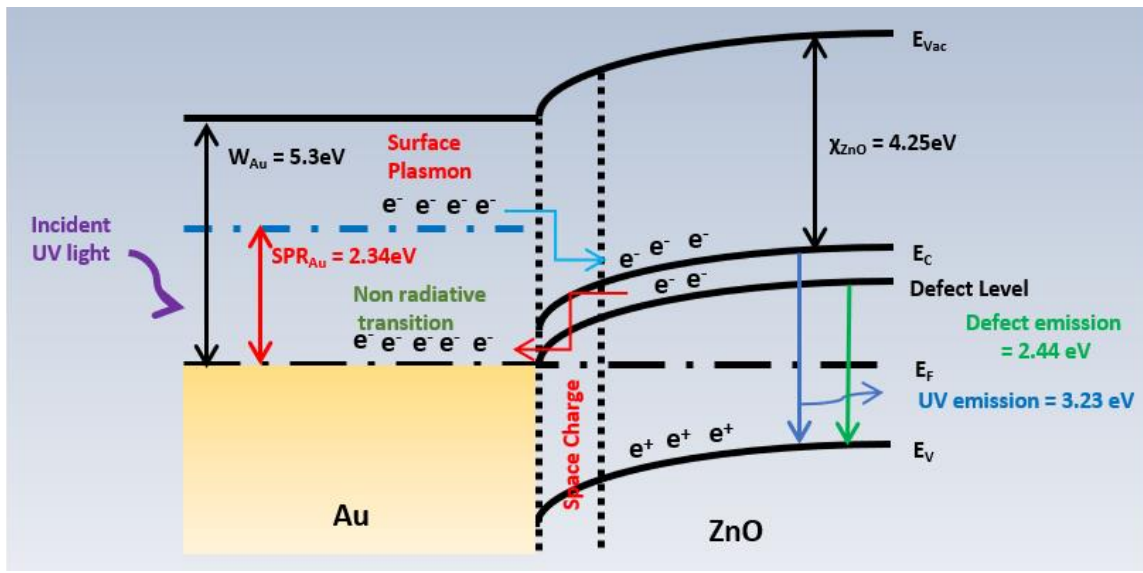


Figure 18 Effect of surface plasmon resonance on the emission of Au coated ZnO nanoribbons

When the nanoribbons are coated with Au NPs, accumulation of the electron cloud occurs at the interface of the nanoribbon and NP. This results in the band bending of ZnO towards Au. This in turn facilitates transfer of electrons from Au to ZnO conduction band. For our ZnO sample, the visible energy is $\sim 2.45\text{ eV}$. On the other hand, the SPR energy of Au NP is $\sim 2.34\text{ eV}$. Also, we can see from the band diagram that the energy of the defect states with respect to the vacuum level ($\sim 5\text{ eV}$) is almost close to that of the Au Fermi level ($\sim 5.3\text{ eV}$). Thus, electrons from the defect states in ZnO flow to the Fermi level of Au resulting in increased electron density in Au. These electrons get further energized to a higher energy state by surface plasmon waves. These resonant electrons are tunneled to the conduction band of ZnO thereby creating a stable equilibrium [66]. The increased electron density in the conduction band thus results in the enhanced PL peak for Au coated ZnO NRs. Therefore, the electrons in the defect levels end up in the conduction band of ZnO via Au due to surface plasmonic resonance. The reduction in the visible peak after Au coating can also be explained by the same phenomena having reverse effect. Owing to the transfer of the electrons from the defect

levels to the conduction band of ZnO, probability of non-radiative recombination of these trapped electrons with the holes in the valence band decreases. Hence, we see a reduction of peak intensity of the visible emission. Similar proposition of energy transfer due to SPR has been reported earlier for band-edge emission enhancement [67-69]. However, in our case, the effect of plasmonic surface resonance seems suppressed, as the effect of plasma during the sputtering can't also be denied.

3.4.4 Analysis of carrier dynamics and relaxation time of ZnO nanoribbons

Femtosecond pump-probe spectroscopy was utilized to investigate the ultrafast dynamics of the surface treated ZnO nanoribbons and compare with the as grown ones. A femtosecond laser pulse of 325 nm, used as the excitation source, induced a change in optical density of the nanoribbons. This change was probed across the excitonic resonance (385 nm) by another supercontinuum probe pulse (340 nm-650 nm) at different time delays. A detailed analysis of the ultrafast dynamics extracted from these measurements are presented here.

In figure 19(a) the spectral evolution of the ZnO surface treated nanoribbons at different time delays excited with a 325nm source having an energy of $764 \mu\text{J}/\text{cm}^2$ is shown. This is a measurement of the change in transmittance of the ZnO nanofibers as a function of wavelength at different time delays. At an early time (~ 100 fs), we observe a small dip at 380 nm corresponding to onset of bleaching of the excitons. After one complete excitation pulse, which is 125 fs, we notice a strong bleaching at 385 nm, where all the carriers from the valence band are excited to a higher energy state which can be either the conduction band or an exciton level leaving holes behind. With the gradual passage of time, the negative absorption peak decreases implying state filling, i.e. carriers from the conduction band starts to return to the equilibrium state. Thus, over a time delay of few ns, an exponential recovery of carrier occurs. Some of these carriers are then captured by the low-lying states before recombining in the valence band. This results in the broad visible spectrum. The defect states referred to here are some of the residual defects.

Figure 19(b) shows the evolution of the kinetics at the excitonic resonance under different pump-fluences of the ZnO surface treated nanoribbons. The relaxation time constants have been derived from the numerical fit to the experimental data. The decay generally involves two-particle process. Hence, we could successfully fit the combined data using a bi-exponential decay function. The measurement at the lowest pump fluence of $19 \mu\text{J}/\text{cm}^2$ shows relaxation with a fast component 300 ps and a longer decay component of 2.6 ns. While the non-radiative recombination results in the faster relaxation of the excited carriers, radiative recombination causes the slower decay. As we increased the pump fluence to $64 \mu\text{J}/\text{cm}^2$, the relaxation time constants obtained are 51 ps and 495 ps. With further increase, of pump fluence to $191 \mu\text{J}/\text{cm}^2$, the faster component decreases to 48 ps and the slower to 239 ps. The faster component is mostly due to the free excitonic decay, while the larger component is attributed to the bound excitonic decay [29]. Furthermore, we observed a faster decay of 8 ps along with a slower component of ~ 76 ps at the highest excitation of $764 \mu\text{J}/\text{cm}^2$, consistent with other studies [29, 30, 70]. Increasing the excitation density results in the generation of more carriers, which in turn decreases the lifetime of the excitons due to increased carrier scattering. Overall, increasing the pump intensity resulted in stronger bleaching and faster recovery of the carriers.

In figure 19(c) is shown the spectral behavior of ZnO nanoribbons before and after the plasma surface treatment. It shows the change in transient absorption peak position as a function of time delays at a high pump-fluence of $764 \mu\text{J}/\text{cm}^2$. We see a shift of the peak to lower energy in case of the plasma treated nanofibers which can be interpreted in terms of stimulated emission. While, our highest applied pump fluence resulted in this Stoke shift with reference to the ground-state bleaching with increasing probe delay for the Ar-plasma treated samples, the same pump fluence could not trigger any such effect for the as-grown sample due to poor surface morphology. Surface treatment results in the removal of majority of the defect centers thereby increasing the absorption and bleaching for

the optically allowed transitions. This results not only in a distinct red-shift of the transient absorption spectra but also a faster relaxation (figure 19(d)) in the surface treated samples as compared to the as grown ZnO nanoribbons.

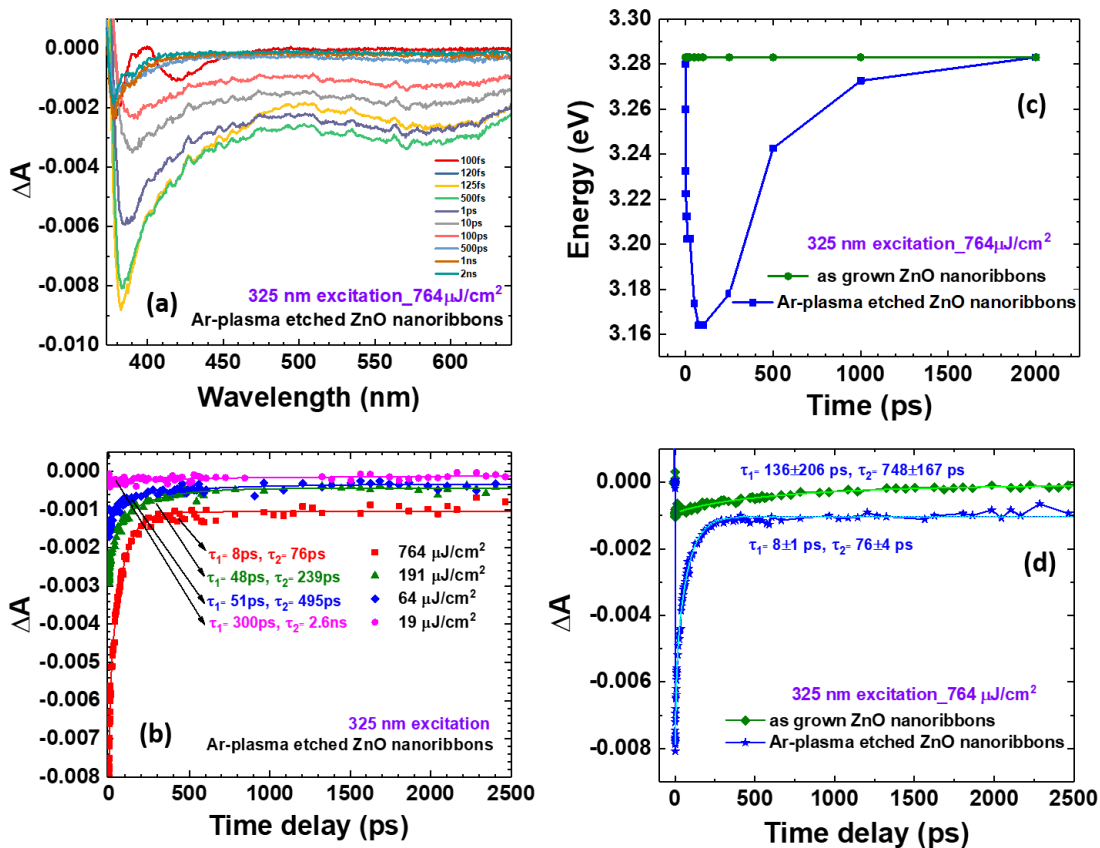


Figure 19 (a) Dynamics of the absorption spectrum at different probe delays following an excitation with a 325nm, 120fs, 600 μW pump pulse and (b) relaxation dynamics for different pump energy for plasma etched ZnO nanoribbons. Comparison of the (c) spectral behavior as function of different time delays and (d) temporal behavior of the nanofibers at the highest pump fluence before and after plasma treatment. Surface modification resulted in the faster relaxation dynamics

3.5 Conclusion

In conclusion, we have demonstrated a very easy and efficient approach to the improvement of the emission properties of ZnO nanofibers. We observed increase in the NBE emission and suppression of the visible emission peak by plasma etching the nanoribbons. We have performed pump-probe spectroscopy, the results and the detailed interpretation of which has been reported. In case of the plasma treated nanofibers, we have not only observed the complete bleaching of all the excitonic transitions, but also a considerable red-shift in the negative absorption peak corresponding to higher density of excitons with a faster relaxation dynamic compared to the as grown nanofibers. We therefore can posit that tailoring the surface emission properties and carrier dynamics significantly in ZnO based nanostructures is possible by simple and efficient surface plasma treatment.

\

4. STIMULATED EMISSION AND OPTICAL PUMPING OF LASING FROM ZINC OXIDE NANOSTRUCTURES: EFFECT OF MORPHOLOGY AND SURFACE TREATMENT ON THE THRESHOLD AND EFFICIENCY

(Abstract of this chapter is copied from my accepted presentation

“Stimulated emission and optical pumping of lasing from ZnO nanostructures: effect of morphology and surface treatment”, Ketaki Sarkar, Richard D Schaller, Michael A Stroschio and Mitra Dutta,

2017 Fall Meeting of the APS Prairie Section
November 11-12, 2017
University of Illinois at Chicago
Chicago, IL)

4.1 Overview of the chapter

Optical probing of ZnO nanostructures elucidates many insightful information of the carrier dynamics and recombination mechanisms. Morphology and surface conditions of these nanostructures have strong role to play in the surface mediated behavior of the excited carrier carriers. The concentration of defects on the surface in nanostructures has a strong effect on the emission properties of ZnO as has been discussed in earlier chapter. As the size of nanostructures decreases from the bulk, the surface to volume ratio increases thereby introducing traps, surface states and other scattering processes. Due to this sensitivity of structural factors and concentration of the defects, it is critical to study the evolution of the emission properties as a function of the morphology and any kind of surface treatment. In this chapter is discussed how surface morphology and improved surface quality has an impact on the transition from spontaneous emission to stimulated emission under high photo-excitation. Lasing from ZnO ribbons by optical pumping has also been discussed. The effect of surface treatment on the threshold and lasing efficiency has been highlighted. The underlying mechanism of the transition from spontaneous to stimulated emission and finally lasing has also been discussed in this chapter.

4.2 High-excitation photoluminescence from different ZnO nanostructures

Three different structures of ZnO were chosen to study the effect of morphology on Amplified Spontaneous Emission (ASE) under the influence of high excitation. As-grown ZnO nanowires, nanofibers and ribbons on Au/Si substrate were used for this specific study. It should be noted here that these three different nanostructures were achieved by changing the growth temperature which in turn changed the vapor pressure resulting in different morphologies.

Figure 20 shows the SEM images of the three different ZnO structures. As can be seen from the inset of the SEM images that while the width of the nanowires is roughly in the range of a few hundreds of nm, that of the nanofibers is around 1-2 μm , and for the ribbons the average width is more than 10 μm . Thus, the width of each of these structures are around one order of magnitude different from the other. These as-grown structures of ZnO were excited using a 325nm excitation under different excitation densities. These observations and their analysis is presented here.

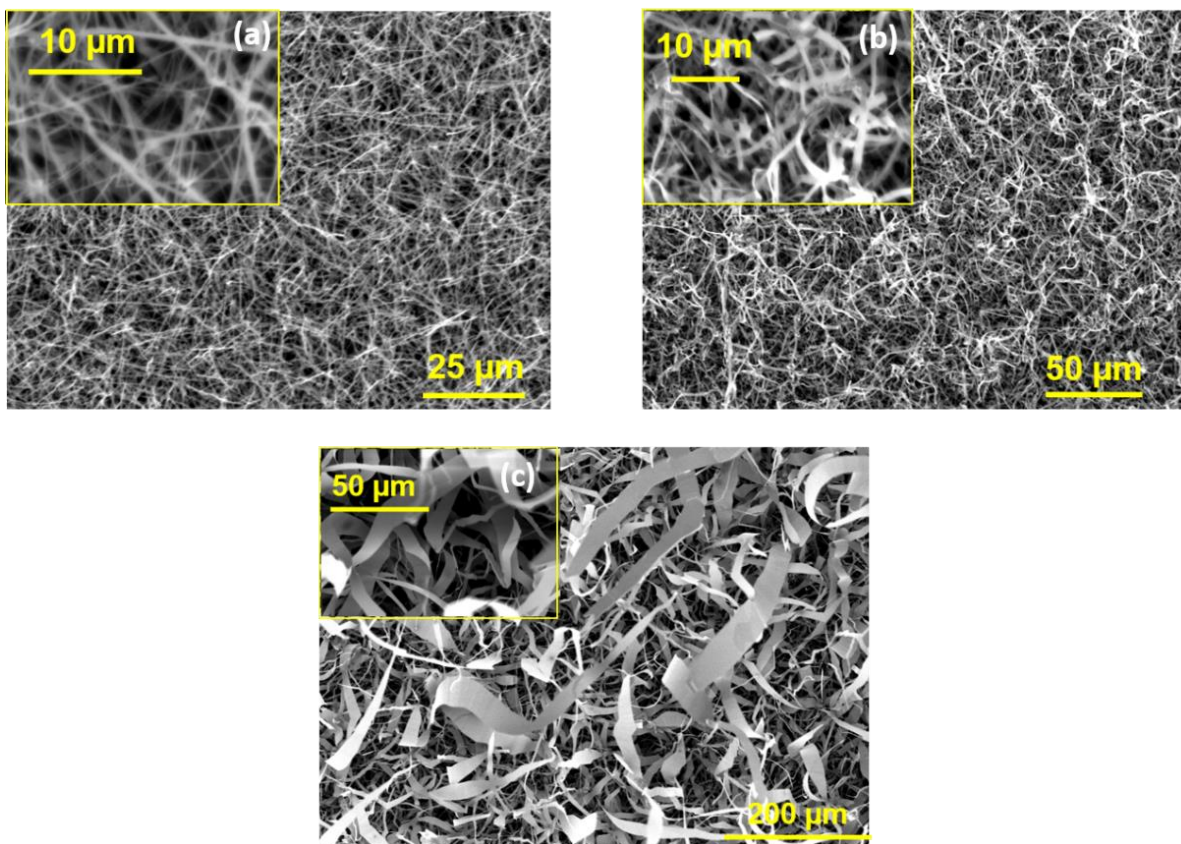


Figure 20 Scanning electron microscopy images of (a) ZnO nanowires, (b) ZnO nanofibers and (c) ZnO ribbons. The inset images in each of the figures shows the magnified structures.

4.2.1 Stimulated emission of different ZnO nanostructure

Figure 21 shows the near-band edge emission from ZnO nanowires, nanofibers and ribbons respectively under the influence of high excitation. As can be seen, when the excitation density is low, a broad spontaneous emission peak appears which can be verified by the fact that the peak intensity varies linearly with the pump power. When the excitation density starts increasing, a gradual narrowing of the PL peak is observed in all the cases at different values of the pump power. These narrow peaks have a very small FWHM which becomes more pronounced above the threshold. These narrow emission peak intensities vary non-linearly with the pumping power. This superlinear increase in the peak intensity accompanied by the sharpening of the PL peak with increase in the pump power

beyond a threshold value is a typical characteristic of stimulated emission. The emission thus changes from spontaneous to stimulated emission resulting from the increased exciton density at high pump power.

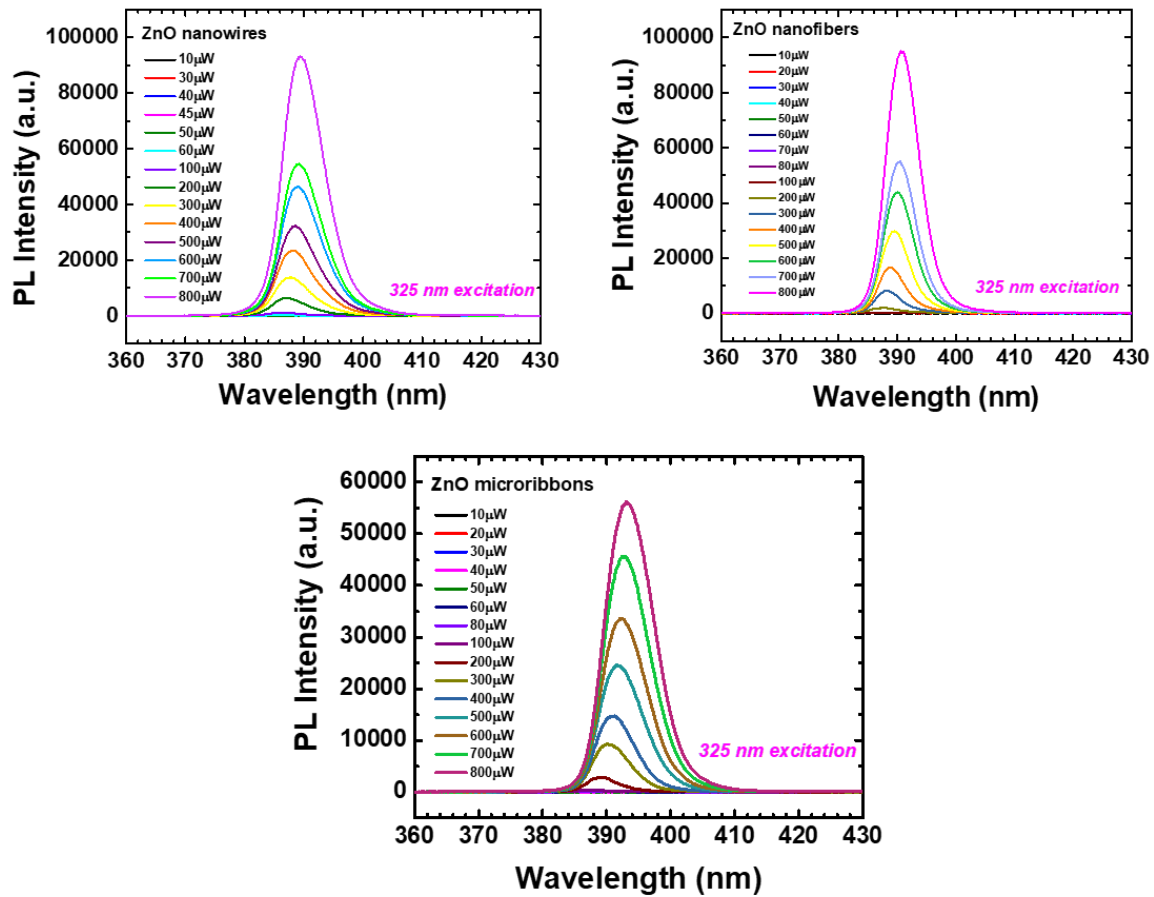


Figure 21 Photoluminescence spectra of (a) ZnO nanowire, (b) ZnO nanofibers and (c) ZnO ribbons measured using a 325nm excitation under different pump-fluence

4.2.2 Effect of morphology on the stimulated emission

Figure 22, show the log-log plots of integrated emission intensity vs the pump power. The dependency of the intensity as a function of the pump-fluence can be expressed as $I_{SE} = I_{ex}^\alpha$ [71]. Our analysis shows a value of $\alpha = 2.72$ for the ZnO micro-ribbons but decreased to $\alpha = 2.48$ for the nanofibers and $\alpha = 2.10$ for the nanowires. We know that for nanowires, the surface area to volume ratio is large and

hence have large number of surface state defects compared to larger micro-ribbons. These defects act as the non-radiative centers reduces the formation of a highly dense exciton population. As a result, the efficiency of the stimulated emission decreases from micro-ribbons to nanowires. On the other hand, due to smaller scattering length, the threshold of stimulated emission in nanowires is less than that in the microribbons.

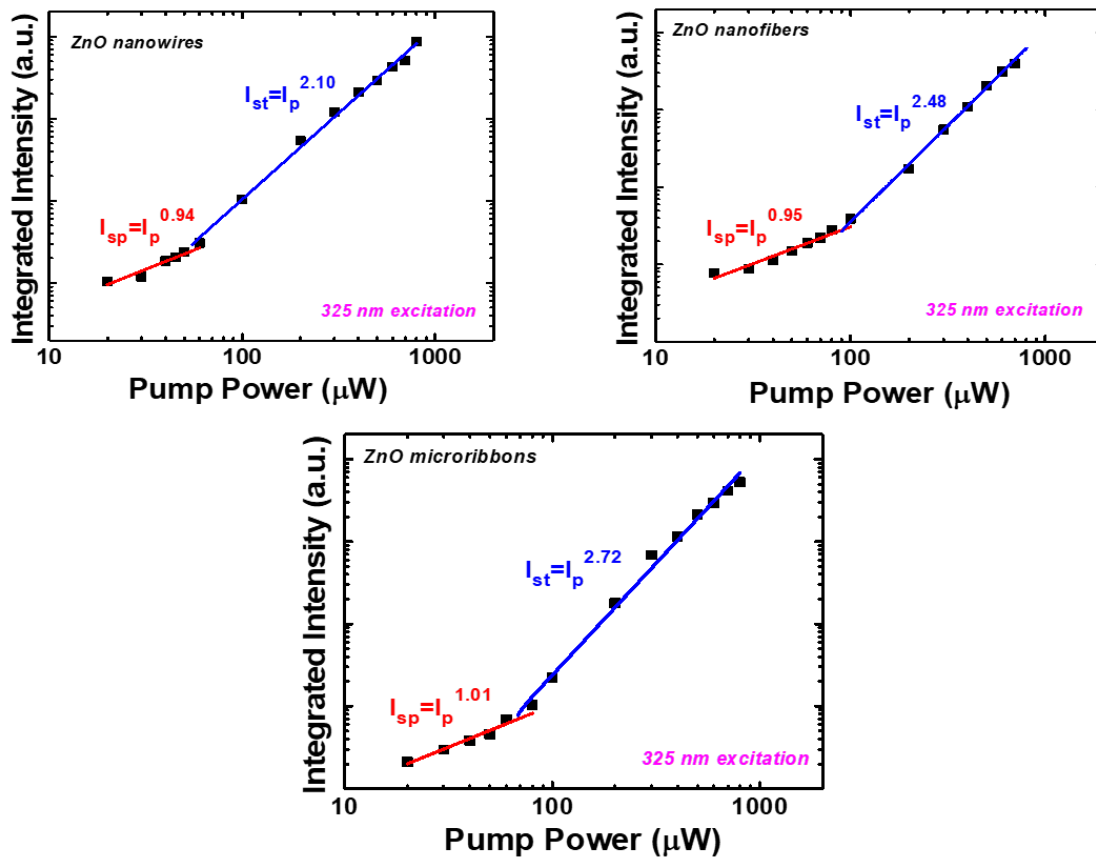


Figure 22 Logarithmic plot of integrated peak intensity vs Pump Power for (a) ZnO nanowire, (b) ZnO nanofibers and (c) ZnO nanoribbons

The case of ZnO ribbons is carefully chosen and analyzed in terms of the narrowing of the line width and the shift in the peak position. It is found that the superlinear increase in the peak intensity of the stimulated emission is accompanied by the narrowing of the linewidth from 134 meV to 54 meV

(figure 23). At a very high excitation, a shift of 69 meV is also in addition to the narrowing of the peak. The energy of a photon resulting from the exciton-exciton scattering can be expressed as [72]:

$$P_n = E_{ex} - E_{ex}^b (1 - 1/n^2) - 3/2KT, \quad (n=2,3,\dots)$$

where P_n is the photon energy, E_{ex} is the free-exciton emission energy (3.226 eV), E_{ex}^b is the excitonic binding energy (60 meV) and kT is the room temperature thermal energy. From the above equation theoretically, the difference in energy between the free-exciton peak and the exciton-exciton peak is obtained to be 83 meV, which is comparable with our experimental energy shift.

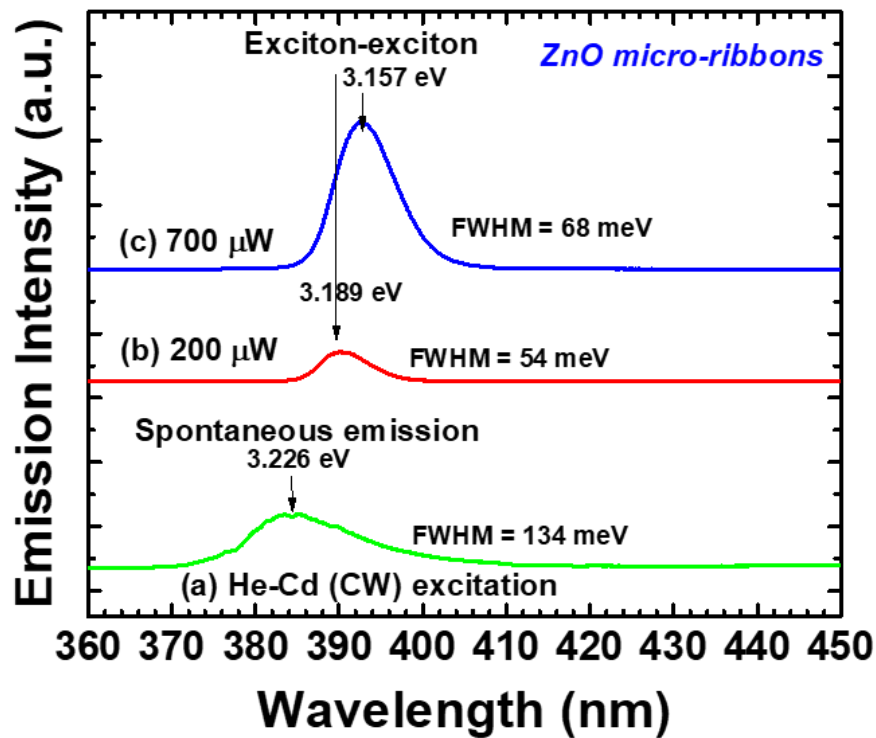


Figure 23 Evolution of PL spectra with pump power

4.3 Lasing from surface passivated ZnO nanoribbons

In this section is discussed how the improved carrier dynamics due to surface treatment have a direct effect on the threshold and efficiency of the random lasing from the material. The ZnO nanoribbons

has been chosen for this study based on the observation reported in the previous sections. A decrease in the lasing threshold and higher order superlinear dependence was observed from the lasing spectra after plasma etching of the ribbons.

4.3.1 Integrated peak intensity and pump fluence

We have observed and characterized luminescence from the as-grown ZnO nanoribbons and compared with that from the plasma etched ZnO nanoribbons both transferred onto quartz substrate. Figure 24(a) and figure 24(b) shows the evolution of luminescence peak with the increase in excitation energy for the ZnO nanoribbons before and after the surface treatment respectively. Due to large excitonic binding energy (60 meV) of ZnO, at lower excitation of the source, excitonic effects are prevalent resulting in broad spontaneous emission peaks. With the increase in excitation energy, exciton-exciton scattering increases, resulting in the appearance of the narrow PL peaks on the shoulder of the broad spontaneous emission peak. This exciton - exciton scattering is due to the creation of a high density of excitons. The appearance of these luminescence peaks with narrow linewidths confirms lasing. This random lasing resulted from the optical amplification due to multiple scattering in closed loops from the randomly oriented ZnO nanoribbons which act as the resonator. At further increased excitation energy, the density of the carriers increases more. As a result, the Coulomb interaction between these carriers results in the decrease in the excitonic binding energy due to screening. And eventually the excitons lose their character and transforms into electron-hole plasma (EHP) state [29]. This is accompanied by a gradual red-shift. This red-shift observed results from the band gap re-normalizations due to the many body effects of EHP recombination [70, 71]. Thus, while at low pump energy, the main process governing the lasing mechanism is exciton recombination, the one at high fluence can be attributed to EHP recombination. The latter implies a large density of carriers which creates population inversion and thus results in optical gain.

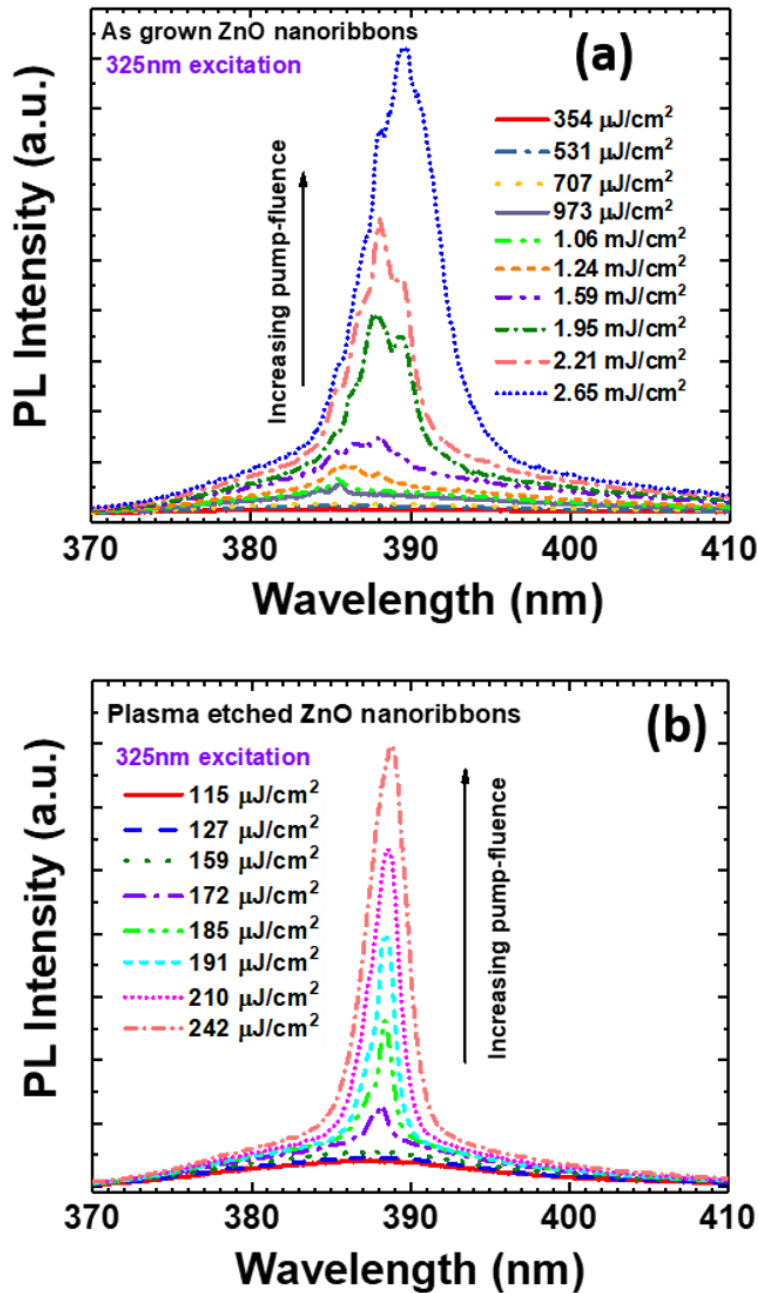


Figure 24 (a) and (b) Evolution of the emission spectra as a function of the excitation intensity in as grown and Ar plasma treated ZnO nanoribbons. Characteristics lasing spectra are observed in both the cases at high laser energy

4.3.2 Threshold and slope efficiency

Figure 25(a) and figure 25(b) shows the log-log plot of the integrated emission intensity versus excitation energy. In both the cases, it reflects the sharp transition from the broad spontaneous emission to sharp lasing. Below the threshold, the spontaneous emission intensity varied linearly with the laser energy. However, above the lasing threshold, the dependence becomes super linear as can be seen from the value of α in both the plots ($I_{SE} = I_{ex}^\alpha$). Our analysis shows that for the as grown sample the value of α is 2, the same nanoribbons after plasma treatment showed a higher order dependence of 2.9. Removal of the surface states after etching which otherwise acts as the non-radiative recombination centers, increases the probability of excitonic recombination and hence higher efficiency of stimulated emission. This is also reflected in the linewidths of the spectra where the peaks are narrower for the plasma treated samples as compared to the untreated ones. Furthermore, the threshold of lasing from these etched structures is seen to decrease to almost half that of the as-grown ribbons due to improved quality of the material of these nanoribbons after the plasma treatment.

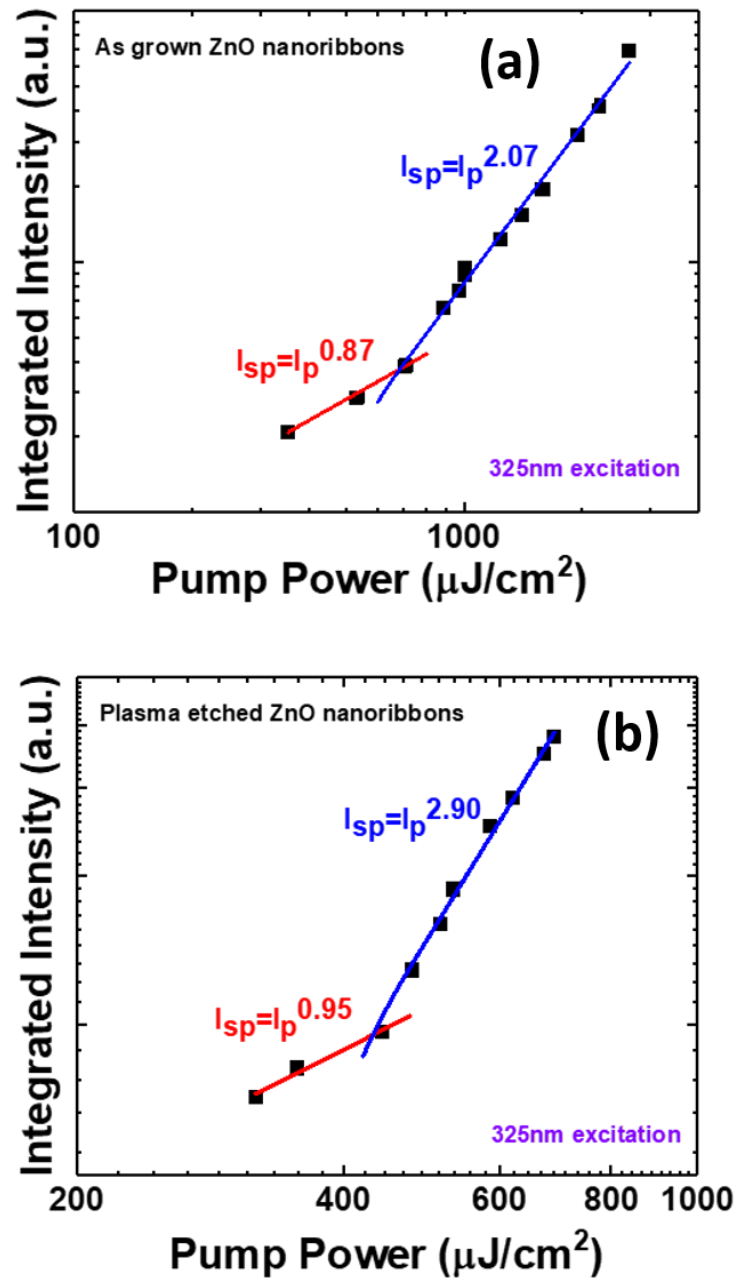


Figure 25 (a) and (b) log-log plot of the integrated peak intensity with the excitation energy showing the threshold behavior in either cases. Clearly, plasma treatment results in the decrease of the lasing threshold of the ZnO nanoribbons

4.3.3 Time-resolved photoluminescence

In figure 26 is shown how surface treatment affects the lifetimes of the excitons under different pump fluences mainly around the lasing threshold. We can see that the exciton lifetime is comparatively smaller in etched ribbons, hence leads to faster radiative decays near and above the lasing threshold, compared to the case of as-grown ribbons due to the presence of surface traps. Passivation helps in the removal of these traps thereby expediting the radiative decay process. We can also observe that the fast component in either cases shifts at a time period of ~ 7 - 10 ps earlier than the onset of lasing as we increase the pump-fluence beyond the threshold value. The abrupt change in the temporal behavior with just $\sim 15\%$ change in the pump fluence is possibly an indication of the fact that the mechanism of lasing changes from exciton-exciton to EHP recombination as has been verified by other scientific reports [29, 73, 74]. As we increase the excitation density, it results in the saturation of the population of the excitons. The time of around 7 ps ~ 10 ps is required for the exciton population to build. It results from the exciton interaction leading to excitonic scattering and hence formation of large concentration of excitons in the excited state. The shift of this fast-transient time close to the lasing threshold is more in case of these ZnO nanoribbons, since larger density of exciton population is required to achieve lasing in these kinds of structures.

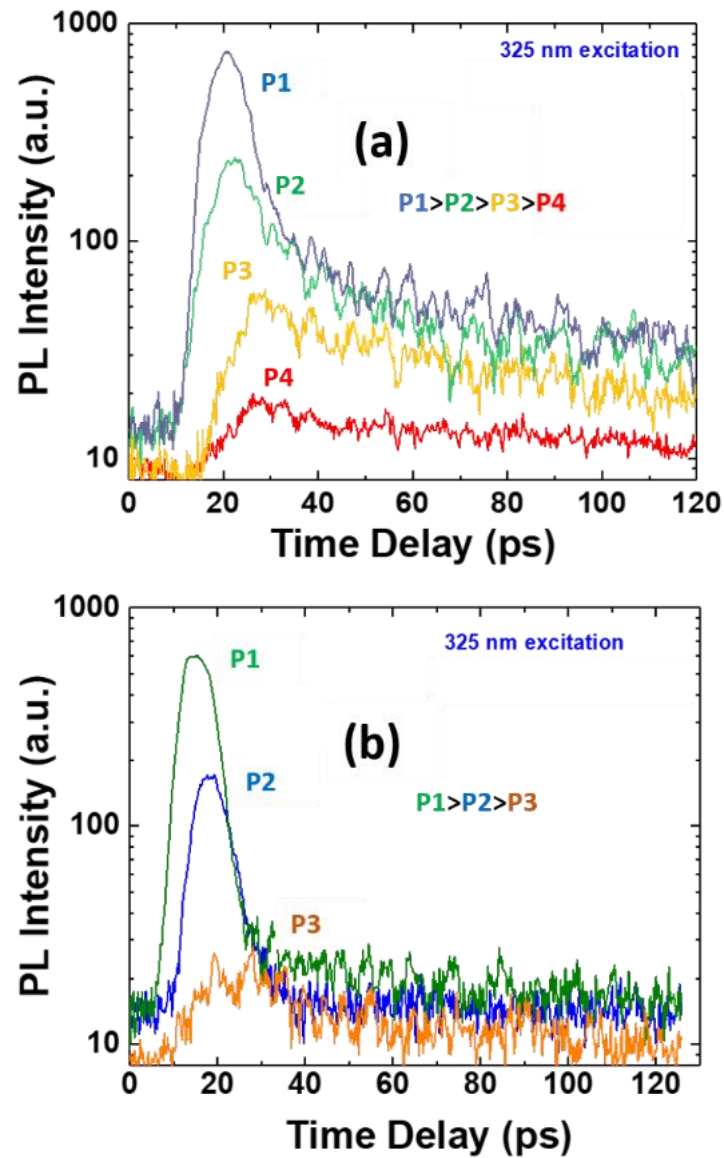


Figure 26 Time-resolved photoluminescence spectra of (a) as-grown ZnO nanoribbons and (b) etched ZnO nanoribbons respectively measured at different pump-fluences

4.4 Conclusion

In conclusion, this chapter emphasized the effect of morphology and surface passivation on the threshold and efficiency of the amplified spontaneous emission from ZnO nanostructures/microstructures. The PL emission peak intensity from ZnO ribbons showed the highest superlinear dependence on the pump power due to lower surface to volume ratio as compared to ZnO nanowires and nanofibers. The underlying principle of high concentration of exciton recombination to induced stimulated emission has also been discussed. Removal of surface traps due to Ar plasma etching and its effect on the lasing threshold and emission efficiency has been explained. Finally, time-resolved photoluminescence revealed faster decay dynamics near lasing threshold for the surface treated nanostructures.

5. STUDY OF AN ENSEMBLE OF INDIUM OXIDE AND ZINC OXIDE NANOSTRUCTURES

(This chapter is entirely copied from my published paper with the following citation

Ref. [56] “Characterization of Co-existing In₂O₃-ZnO Nanostructures, K. Sarkar, S. Mukherjee, S. Farid, A. Nicholls, M. A. Stroschio, M. Dutta, *Journal of Elec Materi* (2017) 46: 5848.)

5.1 Overview of the chapter

In this study, we report the simultaneous growth of both In₂O₃ and ZnO nanostructures on the same substrate when attempting to achieve heavily Zn doped In₂O₃ nanowires with Zn. These oxide structures were synthesized by vapor-liquid-solid (VLS) growth. Scanning electron microscope (SEM) imaging and TEM (Transmission Electron Microscope) shows the presence of nanostructures with different morphologies while Energy-dispersive x-ray (EDX) and x-ray photoelectron spectroscopy (XPS) study confirms the elemental structure. Room temperature photoluminescence (PL) study reveals the presence of oxygen vacancies and surface defects in the structures. Emission related to free and bound excitons as well as the donor-acceptor transitions were observed using temperature dependent photoluminescence. Raman spectroscopy measurement using 442 nm non-resonant excitation sources shows the presence of four phonon modes associated with cubic In₂O₃ lattice structure along with the observation of the dominant E_2^{high} and quasi-longitudinal optical (LO) phonon modes associated with wurtzite ZnO. We find that the introduction of high zinc content results in the formation of ZnO nanowires in addition to the In₂O₃ nanowires, and not the formation of a highly doped In₂O₃ nanowires.

5.2 Background of the doped indium oxide nanowires

One-dimensional nanostructures are of great interest through the past decade for their novel properties as well as building block for sensors and nanoscale devices. Amongst them, oxide based semiconductor nanowires such as ZnO, In₂O₃ and SnO₂ have been explored. The properties of such

oxide based structures and devices can be altered significantly by doping them with various metallic species or by forming alloys. Doping results in the change in carrier concentration in the nanostructures and thus can be utilized to tune the electrical properties while alloying can modify the optical properties. Indium oxide when doped with Zn or Sn is a promising candidate for its applications in gas sensing [75], transparent contacts [76, 39] and as active component in FETs [77]. Several researchers have studied the highly soluble (8%) Sn-doped In_2O_3 nanostructure [78]. However, to the best of our knowledge, only a few studies have been reported on zinc doped In_2O_3 nanostructures. Prior studies show that the maximum doping that can be achieved with Zn in In_2O_3 is 2% [79-80]. We also assume that the atomic size difference of In^{3+} and Zn^{2+} being quite large (18.4%) could be a cause for the practical difficulty in obtaining highly doped of Zn in In_2O_3 .

We have attempted to grow highly doped In_2O_3 nanowires with Zn by incorporating a higher percentage atomic weight of Zn. We present our structural and optical studies and our understanding of the nanostructures grown.

5.3 Growth of co-existing In_2O_3 and ZnO nanowires

Vapor Liquid Solid (VLS) is an inexpensive growth procedure that is useful for growth over large areas and allows for doping of different metals with controlled parameters. In this study electron-beam evaporation was used to deposit 3 nm of Au film on n-type $\langle 100 \rangle$ Si substrate. Indium oxide (99.99% purity) and graphite (99.998% purity) powders were mixed in a ratio of 4:1 ratio by weight for the growth of the indium oxide nanowires. In order to achieve high doping, 15% by weight of the zinc oxide powder was added to the mixture of the indium oxide and graphite powder. This was then thoroughly mixed in a centrifuge operating at 1000 rpm. The powder was then placed in an alumina quartz boat at the center of the quartz tube of a horizontal tube furnace. The Au-coated Si substrates were placed in another alumina boat downstream at a distance of 2~5 cm from the source. The furnace was heated up at a rate of ~ 20 °C/min. The growth was performed at ambient pressure at a temperature

of 900-950 °C for 40-50 mins with Argon (Ar, 99.999%) as a carrier gas. Following the growth, the furnace was allowed to cool down to room temperature before bringing out the samples.

The morphology of these as-grown nanostructures was studied using the JEOL 6320F Scanning electron microscope (SEM). Transmission Electron Microscopy (TEM) and Energy dispersive x-ray (EDX) was done using JEOL JEM 3010 transmission electron microscope to study individual nanowires and their elemental constitution. Analysis of the composition of the nanostructures was done using x-ray photoelectron spectroscopy (XPS). XPS data were collected using a Kratos AXIS-165 spectrometer. The excitation source used was a monochromatic Al K α source ($h\nu = 1486.6$ eV) with an anode voltage of 15 kV and emission current of 10 mA. The pass energy used for this measurement was 20 eV with a step size of 0.1 eV. We studied the photoluminescence (PL) spectroscopy using an ACTON Spectra Pro 2500 spectrometer with HeCd laser (325nm) as the excitation source. Variable temperature photoluminescence measurements were carried out in a Janis He-cryostat system. Raman scattering was done in a backscattering geometry using a laser excitation of 442 nm.

5.4 Morphology of the as grown nanowires

Figure 27(a) gives the SEM image of pure In₂O₃ nanowires having diameter in the range between 200-300 nm and lengths varying from 50-100 μ m. With Zn powder added to the precursor during growth, the image (figure 27(b)) shows the resultant nanostructures consisting of larger diameter In₂O₃ and smaller diameter ZnO nanowires as verified using TEM and EDX analysis. The image also shows the presence of some additional ZnO fibrous structures.

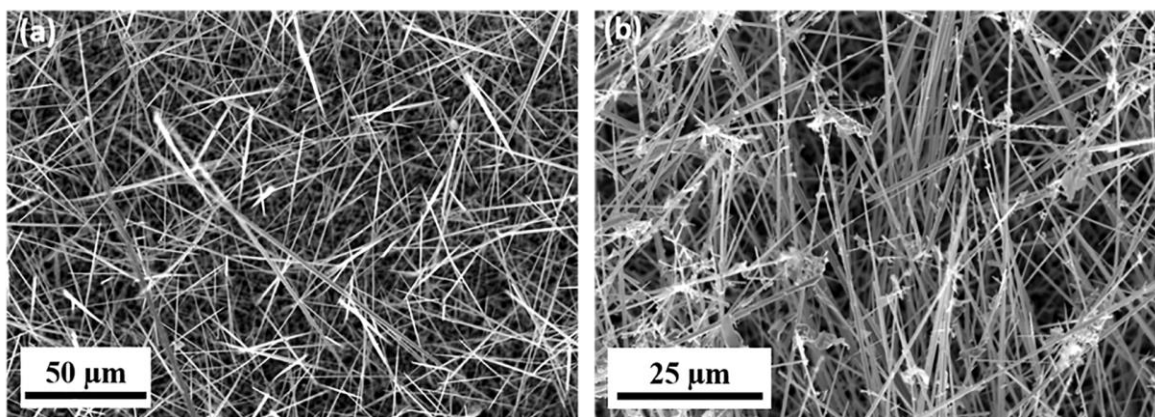


Figure 27 (a) SEM image of the In_2O_3 nanowires, (b) SEM image of an ensemble of In_2O_3 -ZnO nanowires with additional ZnO fibrous structures.

The morphology of individual nanowires and nanofibers were studied using TEM analysis. Figure 28(a) shows the bright-field TEM image of In_2O_3 nanowires with a diameter of around 300nm. The inset TEM image shows a typical In_2O_3 nanowire with Au nanoparticle on the top. Figure 28(b) shows the representative TEM image of ZnO nanowires with a diameter of around 150nm. The EDX spectra in figure 28(c) on the In_2O_3 nanowire shows presence of In and O. The inset image shows the presence of Au precursor at the tip of the nanowire. EDX on the ZnO nanowire is shown in figure 28(d). A general representation of the additional fibrous structures distributed unevenly on the nanowires is shown in the TEM image in figure 29(a). While the thicker nanowire is In_2O_3 as seen from EDX spectra (figure 29(b)), the fibrous material consists of ZnO as revealed in the spectra in figure 29(c). The small In peak in the EDX spectra of the ZnO nanofiber is due to the scattering from the larger In_2O_3 nanowire above it. The conditions for the growth of In_2O_3 and ZnO being similar [81, 82], the formation of these additional nanofibers with the introduction of zinc during growth perhaps results from the change of the surface free energy due to strain induced by the Au-In-Zn ternary phase [82]. Thus, from the TEM microstructural analysis, it can be seen that the In_2O_3 exists separately from the ZnO nanowires. This has been verified later using PL and Raman as well.

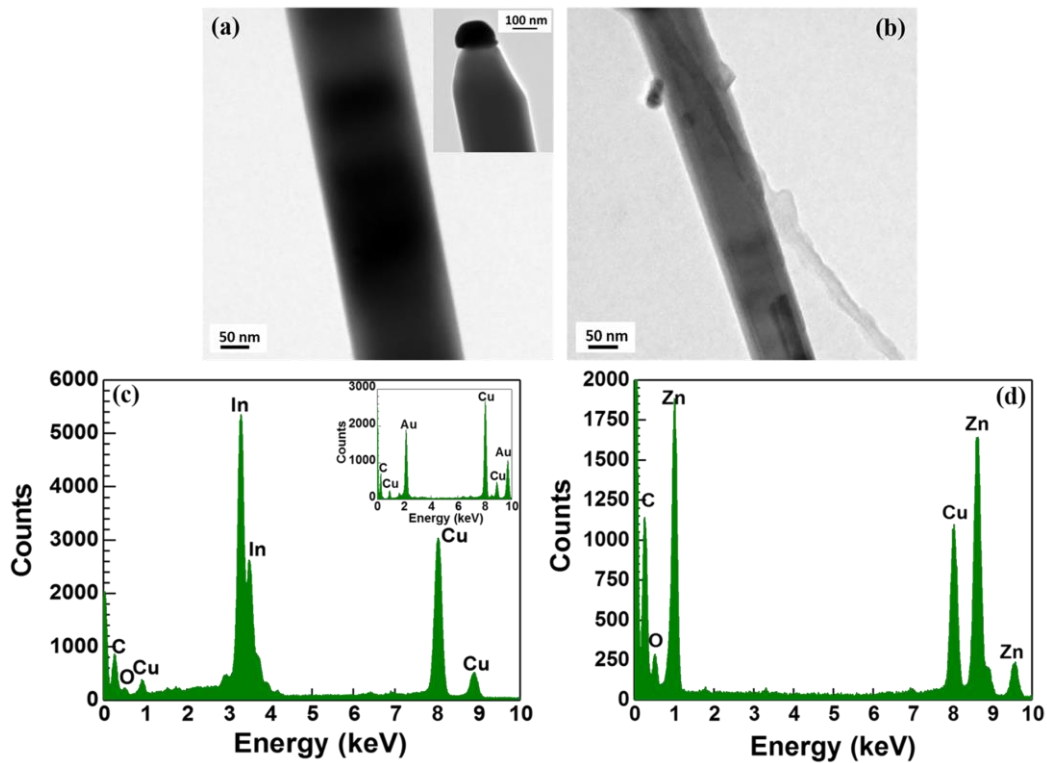


Figure 28 (a) TEM image of the In₂O₃ nanowires. The gold tip at the top of the nanowire is shown in the inset image, (b) TEM image of the ZnO nanowires (c) the EDX spectra of the stem of the In₂O₃ nanowires and of the Au tip (inset image), (d) the EDX spectra of ZnO nanowires.

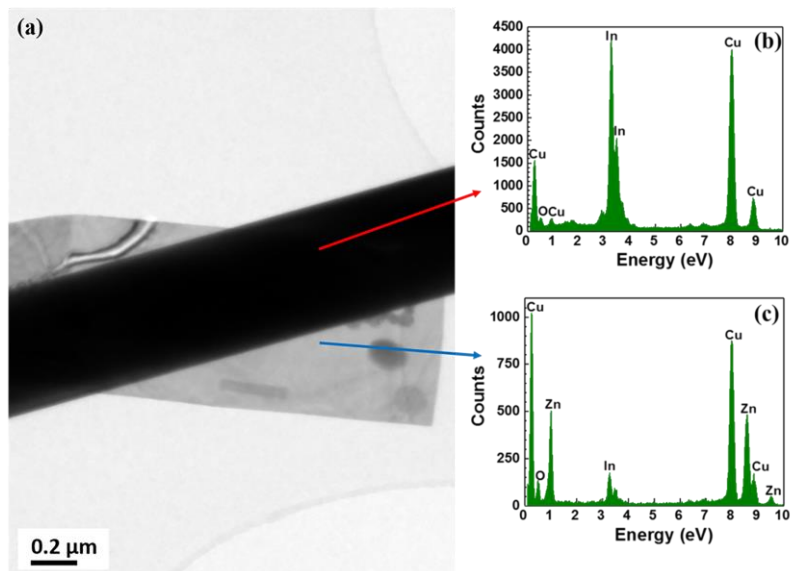


Figure 29 (a) TEM image of the In₂O₃ nanowires with ZnO nanofibers. (b) EDX spectra of the In₂O₃ nanowires (c) EDX spectra of the ZnO nanofibers

5.5 Elemental analysis of the nanowires

In figure 30(a) is shown the XPS spectra for C1s with a peak position at 285.33 eV. This binding energy for C1s was used as the calibration for the XPS spectrum. The carbon was due to extrinsic contamination from the carbon tape on the XPS sample holder. O1s has two symmetric peaks shown in figure 30(b) associated with two different values of binding energies. While the low binding energy peak at 530.21 eV is associated with O^{2-} species in the oxide lattice, the high binding energy peak at 531.88 eV associated with the oxygen vacancy or defects [83, 84]. The XPS spectra for In in figure 30(c) shows two distinct lines of In3d_{5/2} and In3d_{3/2} having binding energies 444.69 eV and 451.94 eV respectively. The spatial gap between the two lines is equal to 7.56 eV which matches with reference value for In₂O₃ [85]. The Zn 2p spectrum has two peaks with binding energies 1022.11 eV and 1046.78 eV corresponding to the Zn2p_{3/2} and Zn2p_{1/2} lines as shown in figure 30(d).

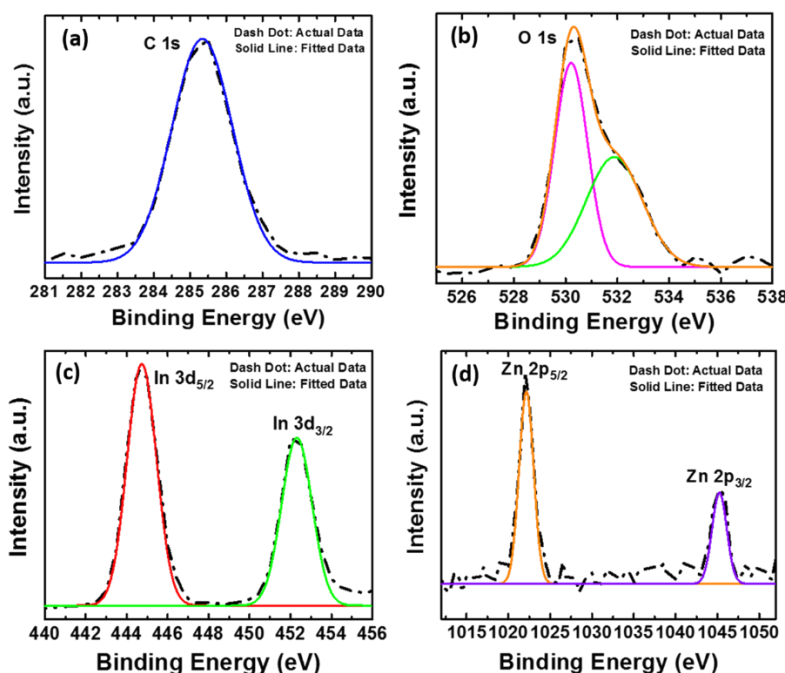


Figure 30 XPS spectra of the In₂O₃-ZnO nanostructures showing both measured and fitted data. (a) High resolution spectrum of C1s with a peak at 285.33 eV, (b) high resolution spectrum of O1s with peaks at 530.21 eV and 531.88 eV, (c) high resolution spectrum of In3d_{5/2} and In3d_{3/2} with peaks at 444.69 eV and 451.94 eV, and (d) high resolution spectrum Zn2p_{3/2} and Zn2p_{1/2} with peaks at 1022.11 eV and 1046.78 eV

5.6 Photoluminescence studies on the co-existing nanowires

Studies show that In_2O_3 has a direct band gap of 3.75 eV and indirect gap of 2.9 eV [86]. As a result, the band-to-band transition or the exciton is not expected to be observed in PL. The visible emissions are due to surface defects and oxygen vacancies caused by incomplete oxidation during VLS growth, which introduces energy levels in the band gap. However, in case of the In_2O_3 any emission higher than its indirect gap i.e. 2.9 eV cannot result from vacancies or defects. Electrons which are excited to energies between 2.9 eV and 3.75 eV or higher encounter scattering from defects or phonons to the lowest point in the conduction band and results in phonon or defect assisted transitions.

5.6.1 Room temperature photoluminescence spectroscopy

In figure 30, the room temperature PL spectrum of In_2O_3 shows a broad visible peak with an orange emission at 2.02 eV as seen in prior work [87, 88]. For the samples grown with the added zinc, a weak emission at 3.25 eV along with a strong green visible peak at 2.39 eV (figure 31). There is also the small orange luminescence peak in addition to the dominant green emission peak. We have observed similar near UV emission from ZnO nanowires and nanofibers in our previous work [89, 90]. The green emission could possibly be from neutral, singly or doubly ionized oxygen vacancies which can be in the ZnO [91, 92].

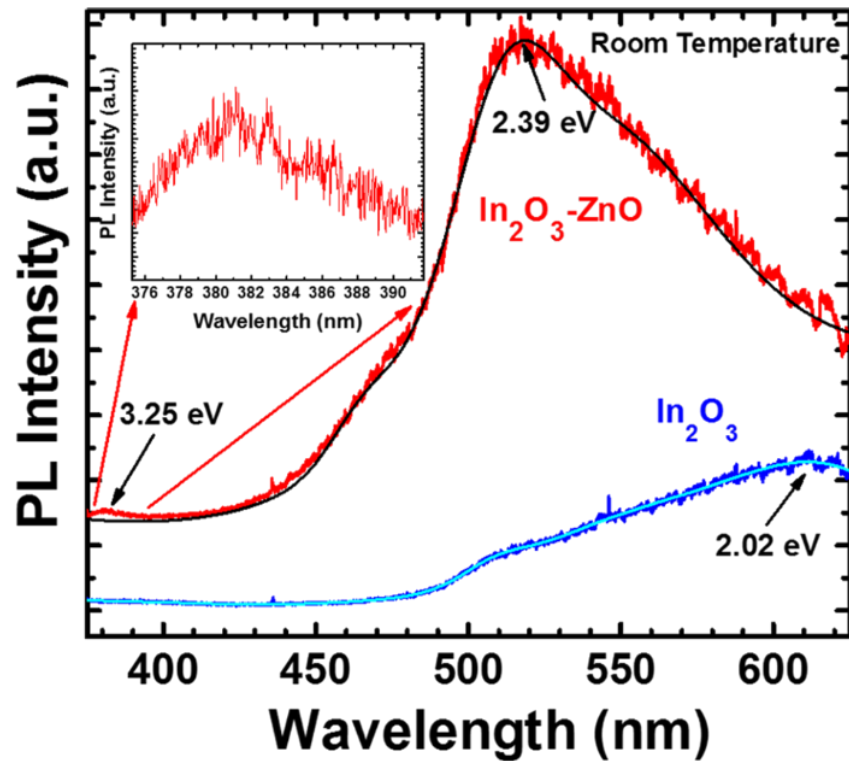


Figure 31 Room temperature photoluminescence spectra of In_2O_3 nanowire and $\text{In}_2\text{O}_3\text{-ZnO}$ nanostructures; both the curves have been fit using Gaussians. The magnified peak of the near UV emission at the bandgap of ZnO is shown in the inset image

5.6.2 High-temperature photoluminescence spectroscopy

The temperature-dependent (30K-100K) PL measurements conducted on the pure In_2O_3 nanowires are shown in figure 32(a). A series of broad orange luminescence peaks which decrease as the temperature increases can be seen. Figure 32(b) has the results from similar experiments on the $\text{In}_2\text{O}_3\text{-ZnO}$ samples. The right inset in figure 32(b) is the de-convoluted peaks associated with the features of the 3.25eV emission. There are 3 major peaks and one small peak on the higher energy side. The wide peak at 3.30 eV is assigned to the donor to acceptor pair (DAP) recombination. The strong peak at 3.35 eV is due to the emission from the bound exciton to neutral donors (D^0X). We also see a very small free-exciton peak at 3.36 eV, which disappears completely at temperatures above

50K. Another broad peak centered at 3.07 eV is also observed, the origin of which is unclear. With increase in temperature, we see a red shift in the D°X peak along with decrease in peak intensities for both DAP and D°X. While the red shift is due to the change in band gap with temperature, the decrease of peak intensity of D°X with temperature results from the thermal dissociation of the bound exciton into a neutral-donor and a free-exciton [93]. This presence of the UV peak at 3.25 eV at room temperature or 3.36 eV at low temperatures (30K) near the band gap of ZnO and not near either the direct or indirect gap of In₂O₃ indicates the presence of ZnO rather than Zn present as a dopant or alloy of InZnO.

The intensity dependence of visible emission peak at 2.02 V for In₂O₃ and that of the wide broad band peak at 3.07 eV are shown in the left inset of figure 32(a) and figure 32(b), where the rectangles show the experimental data, the dotted line is the fitted curve obtained using Arrhenius equation. Using a single quenching channel in the Arrhenius plot, the activation energies obtained from the slope were 12.17 meV and 13.77 meV for the respective emissions from In₂O₃ and ZnO nanowires. This indicates that the shallow donor levels are being quenched with the increase in temperature.

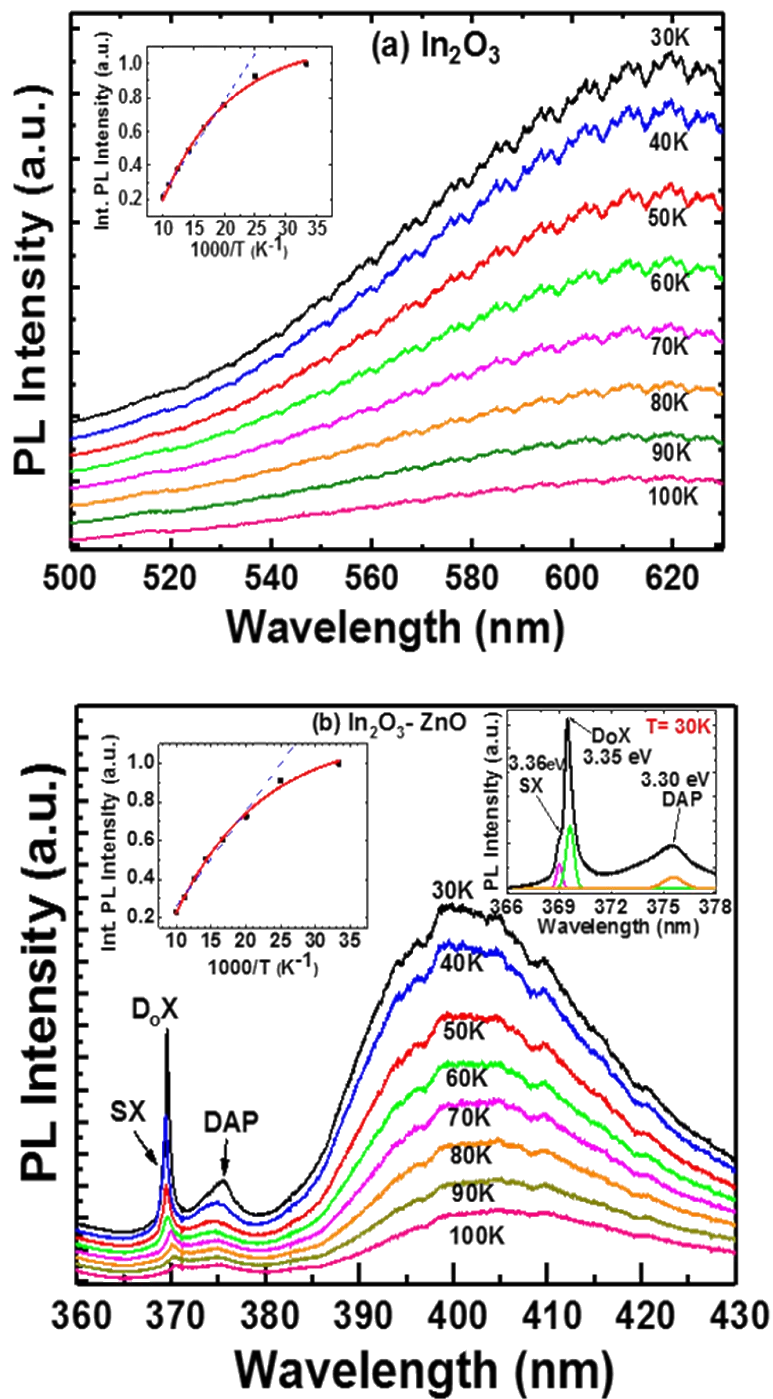


Figure 32 Low temperature PL spectra of (a) In_2O_3 nanowires, and (b) In_2O_3 -ZnO nanostructures. The left inset image in (a) and (b) are the integrated PL intensities as functions of temperature. In the right inset image in (b) is shown the resolved UV peaks at 30K for better peak identification

5.7 Raman spectroscopy measurements

The Raman spectrum for single crystalline In_2O_3 at room temperature is shown in figure 33(a). Four vibrational modes at 308 cm^{-1} , 389 cm^{-1} , 493 cm^{-1} and 627 cm^{-1} of E_g , F_{2g} , A_g and F_{2g} symmetries respectively suggesting In_2O_3 with cubic structure. While the phonon modes at 308 cm^{-1} , 493 cm^{-1} and 627 cm^{-1} are commonly observed; an additional mode at 389 cm^{-1} with F_{2g} symmetry has been reported rarely [94]. The Raman active modes for cubic In_2O_3 crystal consist of $4A_g$, $4E_g$ and $14F_g$ modes [95]. When Zn is incorporated in the samples, we observe an additional non-polar mode at 438 cm^{-1} and polar mode at 580 cm^{-1} as shown in figure 33(b). The phonon mode frequency at 638 cm^{-1} is red shifted in comparison to the pure In_2O_3 nanowires and is believed to be caused by the superposition of two different modes with A_g and F_{2g} symmetry. The Raman active optical modes for wurtzite ZnO crystal are A_1 , E_1 and two E_2 modes [96]. In case of our sample while the E_{high}^2 at 438 cm^{-1} is certainly the dominant peak in the spectrum, the mode frequency at 580 cm^{-1} differs from A_1 or the E_1 modes reported in literature [97]. The random orientation of these ZnO nanostructures leads to the interaction of the $A_1(LO)$ and $E_1(LO)$ modes which results in the quasi phonon modes with frequencies lying between those of pure $A_1(LO)$ and pure $E_1(LO)$.

Using Loudon's model [55], we can calculate the frequency of this quasi- LO phonon mode as follows:

$$\omega_q^2(LO) = \omega_{A_1}^2(LO)\cos^2\alpha + \omega_{E_1}^2(LO)\sin^2\alpha \quad (1)$$

where α is the angle of propagation of the phonon with respect to the c-axis of the crystal. Eq. (1) can be expressed as follows:

$$\omega_q^2(LO) = \omega_o^2 \left[1 + \frac{\omega_{A_1}^2(LO) - \omega_o^2}{\omega_o^2} \cos^2\alpha + \frac{\omega_{E_1}^2(LO) - \omega_o^2}{\omega_o^2} \sin^2\alpha \right] \quad (2)$$

Where, ω_o is the average quasi-mode frequency as shown latter. By expanding Eq. (2) and neglecting the higher order terms, the quasi- LO phono mode frequency can be expressed as:

$$\langle \omega_q(LO) \rangle = \omega_o \left[1 + \frac{1}{3} \frac{\omega_{A_1}^2(LO) - \omega_o^2}{\omega_o^2} + \frac{1}{6} \frac{\omega_{E_1}^2(LO) - \omega_o^2}{\omega_o^2} \right] \quad (3)$$

Choosing the value of ω_o in a way that the last two terms in Eq. (3) are eliminated, and the average quasi-mode frequency can be written as,

$$\langle \omega_q(LO) \rangle^2 = \omega_o^2 = \left[\frac{2\omega_{A_1}^2(LO) + \omega_{E_1}^2(LO)}{3} \right] \quad (4)$$

Inserting the values of $A_1(LO)$ and $E_1(LO)$ in Eq. (4) to be 574 cm^{-1} and 590 cm^{-1} as reported in literature [97], the resultant frequency of the LO quasi-phonon mode is 579.38 cm^{-1} which is almost identical to the peak (580 cm^{-1}) we observed. Similarly, if we calculate the quasi-mode frequency for TO phonons using values from literature [97] which are 378 cm^{-1} and 410 cm^{-1} for $A_1(TO)$ and $E_1(TO)$ respectively, the resultant value is 388.96 cm^{-1} which is also very close to the peak that we observe at 390 cm^{-1} . This peak at 390 cm^{-1} could be either due to $A_1(TO)$ - $E_1(TO)$ quasi-phonon mode from the wurtzite ZnO or the phonon mode with F_{2g} symmetry from cubic In_2O_3 . The observation of the dominant E_{high}^2 mode along with these quasi phonon modes is similar to that observed in prior studies on ZnO [17], thus confirming the formation of ZnO as randomly oriented nanowires along with In_2O_3 nanowires when zinc powder is introduced during growth.

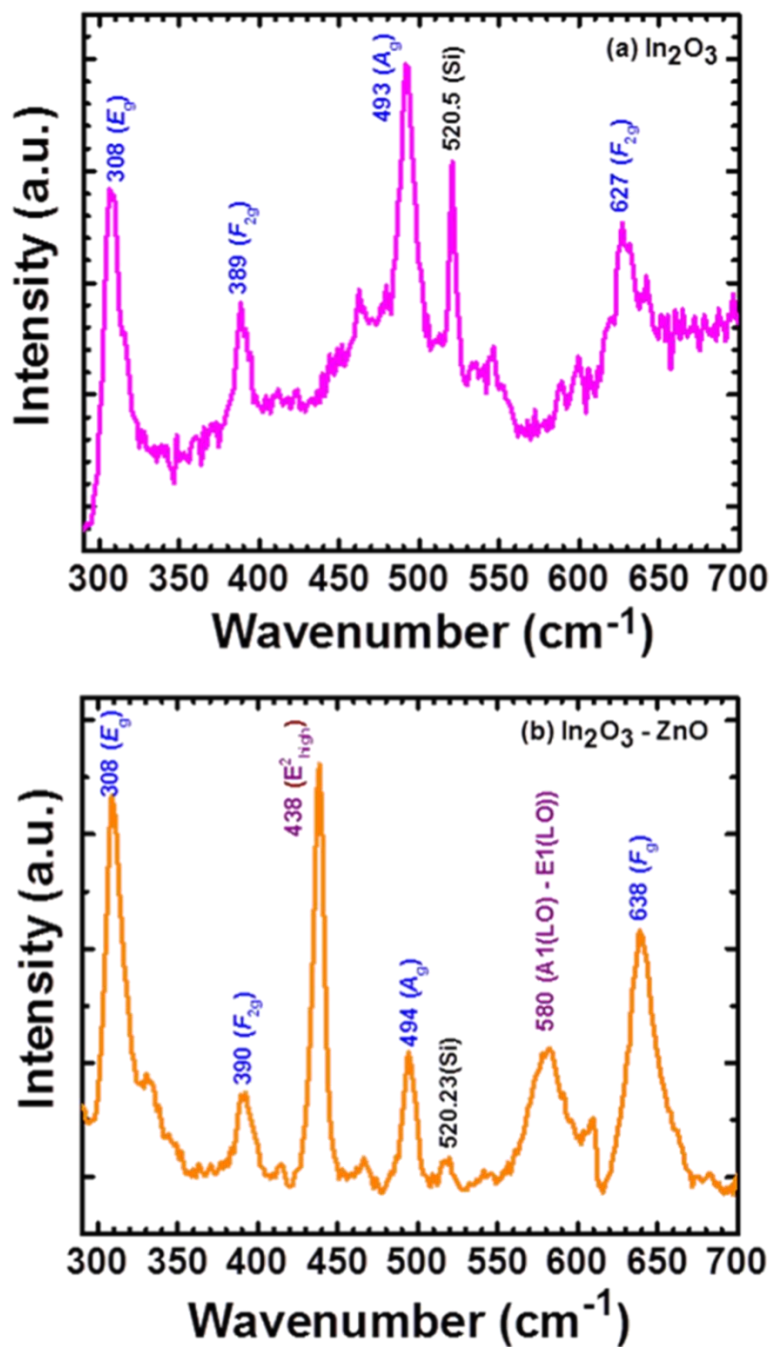


Figure 33 Room temperature Raman spectra of (a) In_2O_3 showing distinct modes of the cubic crystal, and (b) In_2O_3 -ZnO with additional non-polar and quasi LO phonon modes of the polycrystalline wurtzite crystal of ZnO nanowires in addition to the vibrational modes from cubic In_2O_3 nanowires.

5.8 Conclusion

In summary, we have grown and studied the ensemble of In_2O_3 and ZnO nanowires on the same substrate in the same growth. The optical and structural characterization showed the presence of both In_2O_3 and ZnO . TEM microstructural analysis indicated that two distinctly different nanowires of In_2O_3 and ZnO were formed with the introduction of high zinc ratio during the growth, with ZnO nanofibers coating the nanowires in some cases. EDX analysis showed that we did not achieve either heavy doping nor was there any alloying. This was further confirmed by the optical studies which showed similar results. Raman study indicates cubic structure of In_2O_3 nanowires as well the spectra that is the signature of randomly oriented nanowires of ZnO . From these results, we see that the introduction of the high zinc ratio in the growth did not result in high doping but in the formation of co-existing ZnO nanowires and nanofibers in addition to the In_2O_3 nanowires.

6. OPTICAL PHONON MODES FROM A SHORT PERIOD ALUMINIUM NITRIDE/GALLIUM NITRIDE SUPERLATTICE

(Portion of this chapter is copied from my manuscript to be submitted to *Superlattices and Microstructures*)

“Raman analysis of phonon modes in a short period AlN/GaN superlattice”, Ketaki Sarkar, Debopam Datta, David J Gosztola, Michael A Stroschio and Mitra Dutta.

6.1 Overview of the chapter

It is a quite a well-known fact that AlN/GaN based optoelectronic devices is one of the intriguing areas of the research community. Exploring and optimizing the structure is the prelude to commercialization of an efficient device. While there are several aspects that need to be considered while designing these structures, it is equally important to study their lattice dynamics or related electron-phonon interactions specific to the interface of these heterostructures which results in additional optical phonon modes known as interface phonon modes. In this study, the framework of the dielectric continuum model has been utilized to compare and analyze the optical phonon modes obtained from experimental Raman scattering measurements on unstrained AlN/GaN superlattice using backscattering geometry. We have observed the localized $E_2(\text{high})$, $A_1(\text{LO})$ and the $E_1(\text{TO})$ from the superlattice measurement at frequencies shifted from their bulk values. In addition, we have also identified additional spread of interface phonon modes in the TO range resulting from the superlattice. Contribution from the underlying $\text{Al}_x\text{Ga}_{1-x}\text{N}$ ternary in the Raman spectrum has also been observed and analyzed. A temperature calibration was done based on Stokes/anti-Stokes ratio of $E_2(\text{high})$ and $A_1(\text{LO})$ using Raman spectroscopy in a broad operating temperature range. A good agreement between the experimental results and theoretically calculated calibration plot predicted using Bose-Einstein statistics was obtained.

6.2 Background on AlN/GaN based superlattice

AlN and GaN based semiconductors, owing to their large electronic band gap are interesting materials for the fabrication of blue and UV laser and as electronic devices with operation in high temperature and power regime [98, 99]. Specially, the optical properties of films consisting of short period superlattice(SL) structures with alternating layers of AlN/GaN can be tailored for optimization of SL based optoelectronics device applications. Although they exist in both zinc blende and wurtzite form, the study of the optical phonons in case of the latter is more intriguing due to the dielectric anisotropy resulting from the lower symmetry.

According to the dielectric continuum model and Loudon's model for uniaxial crystal, there are five different types of modes in a wurtzite multilayered heterostructures: propagating, confined, quasi-confined, interface and half-space modes [100]. There are several reported works on theoretical studies of wurtzite nitride superlattice which have investigated the polar optical vibrations [100, 101], and some experimental studies on the angular dispersion modes from these wurtzite heterostructures/superlattices [102-103]. However, very few experimental work [104, 105] have been reported so far for very short period superlattice structures possibly due to the dependence of the interface phonons on the material quality of the superlattices. In this study we discuss on the experimentally obtained phonon modes using Raman Spectroscopy with back scattering geometry from a very short period superlattice consisting of alternating layers of AlN and GaN each with a thickness of 0.75 nm and its underlying diffused layer of AlN and GaN. We have extended the transfer matrix method discussed by SeGi Yu et al [101] involving simple transfer matrix multiplication for the derivation of potential and finally the dispersion relation to our AlN/GaN superlattice. The Stokes/anti-Stokes ratio of the

infra-red active $E_2(\text{high})$ and $A_1(\text{LO})$ mode was also measured as a function of high temperature and compared with theoretical estimation using Bose-Einstein statistics.

6.3 Experimental details

A short period AlN/GaN based superlattice on (0001) sapphire (16mm \pm 0.5mm) were obtained from University wafers. The resulting heterostructure grown on top of a thick GaN buffer layer was carefully analyzed using high resolution scanning transmission electron microscopy (HRSTEM). JEOL JEM-ARM200CF STEM and Oxford Energy Dispersive X-ray (EDX) spectroscopy were used for acquiring the cross-sectional images and the elemental constituents respectively. Figure 34(a) shows the presence of a thin AlN cap layer with thickness of \sim 4 nm at the top of the structure. Below this thin AlN layer lies the alternating layers of AlN/GaN which forms the superlattice. We can observe around 4 periods of alternating GaN and AlN layers each 3 monolayers (\sim 0.75 nm) thick in the STEM image. The underlying region below the superlattice is a diffused structure of AlN and GaN ($\text{Al}_x\text{Ga}_{1-x}\text{N}$) where the Ga concentration increases towards the GaN buffer layer as can be seen from the distribution of elements in figure 34(b). The total thickness of this layer is around \sim 8 nm.

Room-temperature Raman spectroscopy measurements were done in a Renishaw inVia Reflex Raman system using a 514 nm excitation. The laser spot was around 1 μm while the resolution of the system was close to 1cm^{-1} . The measurements were done in back scattering geometry where the growth direction of the SL, i.e. the c-axis, was kept parallel to the z-direction. For the high-temperature measurement, the same Raman system integrated with a temperature controlled hot stage was used. The excitation source energy being less than the band gap of GaN, the effect of any laser heating or absorption during probing the structure has therefore been neglected.

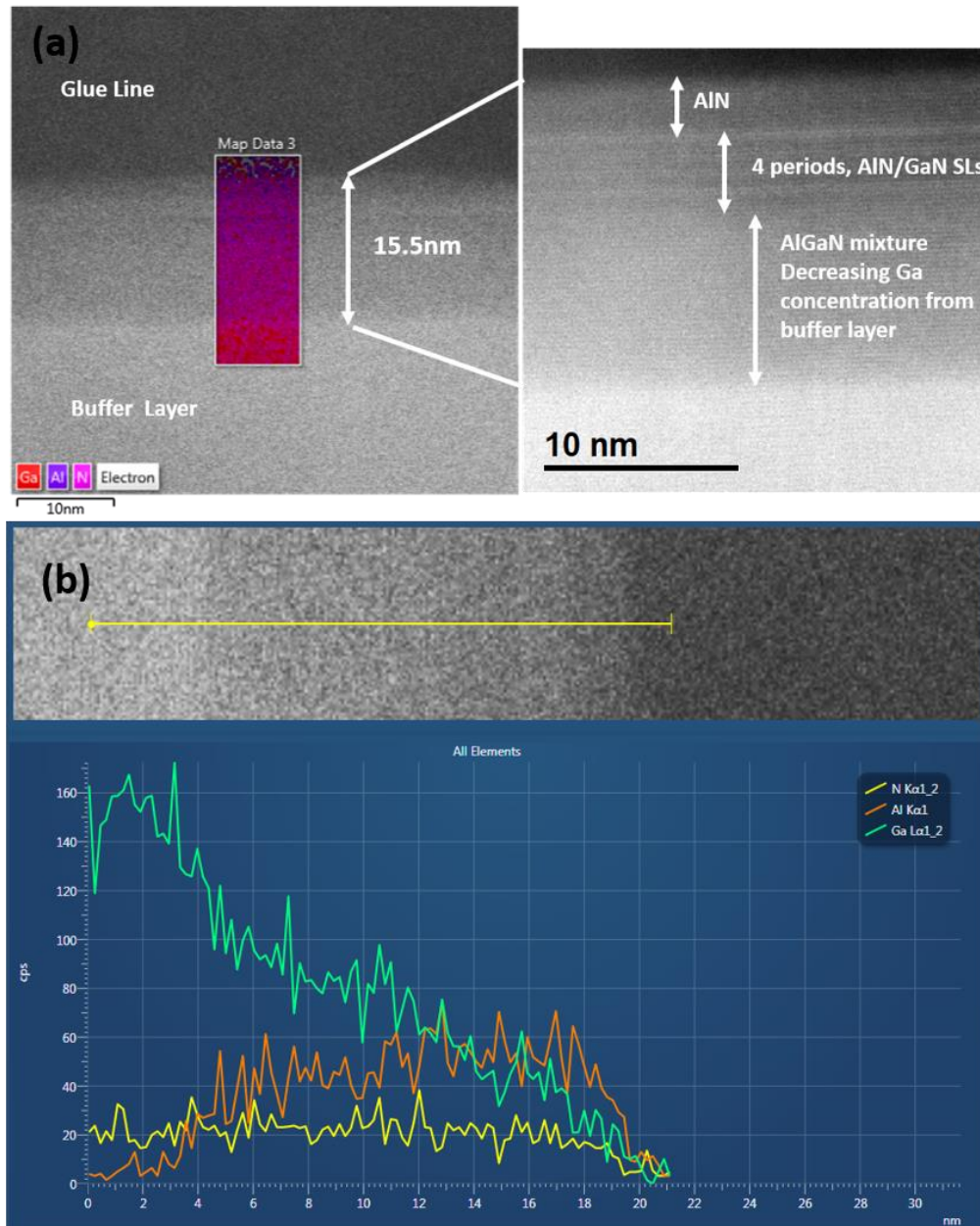


Figure 34 (a) HRSTEM images of the AlN and GaN based heterostructure after growth showing the presence of a thin AlN cap layer followed by the 4 period AlN/GaN superlattice and finally a mixture of AlN and GaN where the Ga composition increases towards the GaN buffer layer, (b) distribution of all elements across the top heterostructure.

6.4 Results and discussions

6.4.1 Raman spectroscopy on short period superlattice

When a semiconducting material is surrounded by another having different dielectric constants, their interface between them is the reason for the interface modes. Interestingly, the linewidth and frequencies of these interface phonons have dependency on the dielectric constant of the surrounding material. Thus, nanomaterials with interlayers are expected to demonstrate strong interface modes as compared to the bulk phonon modes. These interfaces between two heterolayers are the most important contributing factor for creation of additional phonons and have a potential role to play in the distribution of this heat. In general, identification of SL phonon modes is complicated by the fact that the formation of a superlattice leads to zone folding along the z-axis i.e. the growth direction [106]. The estimation of the additional modes is therefore based on the theoretical calculations. The values of the zone center frequencies for the theoretical modeling have been referred from P. Perlin *et al* [107] which defines the boundary of these interface phonon spread in the theoretical dispersion curve shown in figure 35(b). It is also a well-established fact that A_1 and E_2 have manifested one-mode and two-mode behavior respectively in ternary nitride based structures [104, 108]. The presence of the underlying ternary $Al_xGa_{1-x}N$ formed by diffusion and intermixing of the superlattice layers during growth or during the sample preparation for the TEM appears to contribute to the phonon spectra observed in Fig 35.

Figure 35(a) shows the Raman spectra obtained from the GaN/AlN superlattice under back scattering geometry using an excitation of 2.41eV. The features at 572, 673 and 735 cm^{-1} obey the selection rules for $E_2(high)$, $E_1(TO)$ and $A_1(LO)$. Moreover, their relative intensities and proximity to

the frequencies from the unstrained bulk GaN and AlN [103] suggests that these observed modes could be the localized modes from the SL as explained in other research reports [102, 109]. According to literature [102, 110], the slight shifts in the frequencies can be associated to elastic strain introduced during growth. The Raman spectra also shows additional peaks in the TO region from 580-660 cm^{-1} . If observed carefully and compared with the theoretically obtained dispersion curve for the interface phonons, it can be seen that the frequency spread matches that of the theoretically obtained IF phonon modes in the TO range. However, the proximity of the interface phonon modes with that of the one-mode and two-modes behavior of $\text{Al}_x\text{Ga}_{1-x}\text{N}$ ternary in addition to the fact that sapphire have a rich phonon spectrum in the similar range, makes it difficult to assign the Raman modes unambiguously. The composition of the underlying diffused layer of $\text{Al}_x\text{Ga}_{1-x}\text{N}$ being unknown, the assignment of the peak at 643 cm^{-1} is difficult. Although the frequency falls in the $IF(TO)$ range, the possibility of it as the E_2 mode from the $\text{Al}_x\text{Ga}_{1-x}\text{N}$ cannot therefore be ruled out. Since, E_2 shows a two-mode behavior, so, while 643 cm^{-1} is one of two set of frequencies, the other could be any of the modes on the high frequency side of 572 cm^{-1} , although an accurate assignment could not be done at this stage and needs further study. On the other hand, the feature at 602 cm^{-1} can be attributed to interface phonon based on the close agreement with the asymmetric nature along with the peak position as reported by M. Dutta et al [104]. We also observed broad shoulder on the high frequency side of the $A_1(LO)$. This could result from the one mode behavior of the $A_1(LO)$ from the $\text{Al}_x\text{Ga}_{1-x}\text{N}$ layer. Overall, the Raman spectrum obtained from the structure as revealed by the STEM images, shows evidence of interface phonons along with the optical modes from the superlattice and the one-mode behavior of $A_1(LO)$ from the thin underlying ternary of $\text{Al}_x\text{Ga}_{1-x}\text{N}$. However, the two-mode behavior for E_2 could not be observed.

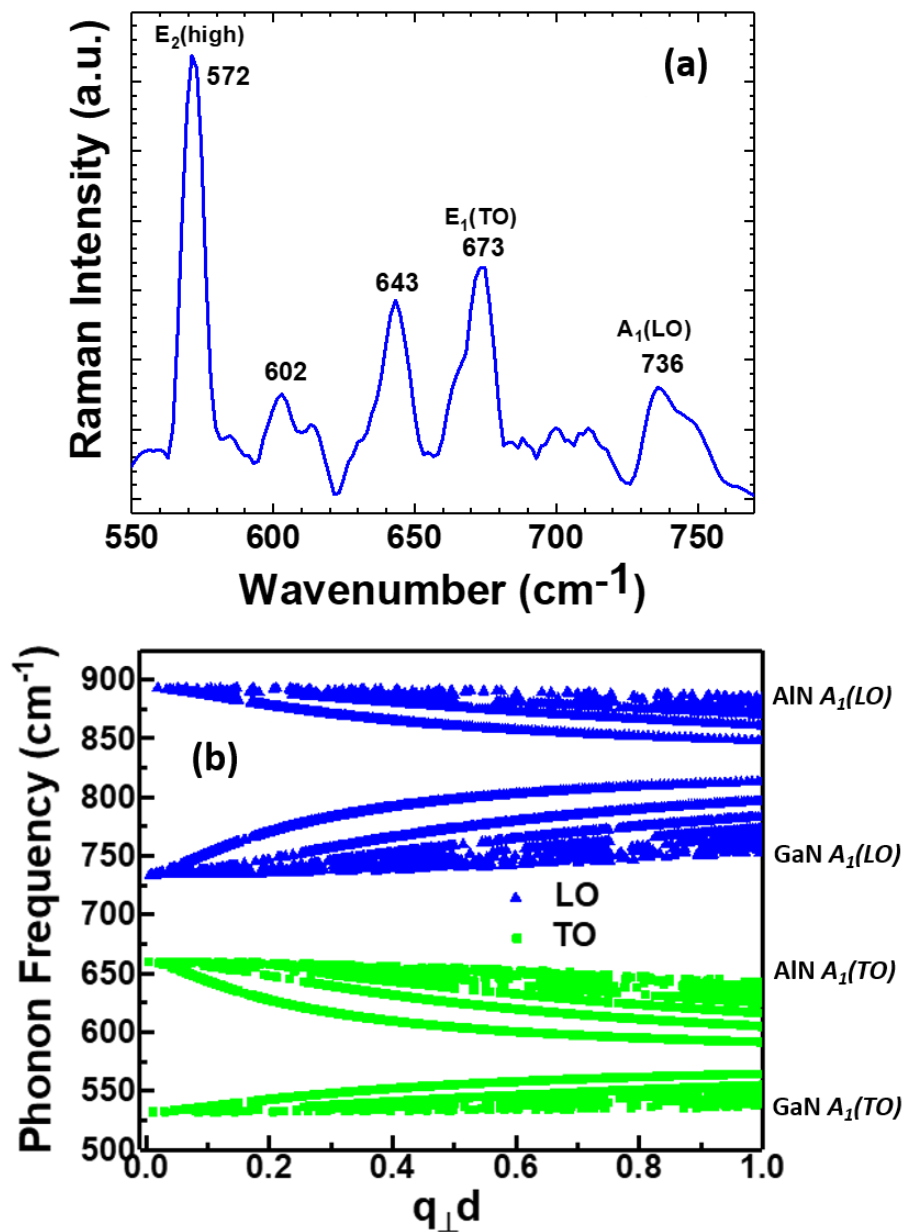


Figure 35 (a) Raman spectra of the AlN/GaN superlattice with a 514 nm excitation under back scattering geometry (b) Theoretically obtained dispersion curve for the same structure using Dielectric Continuum Model.

6.4.2 Temperature Calibration using Raman Spectroscopy

In a typical HEMT, electric field which exists across the gate, accelerates electrons with high energy. It is well known that such hot electrons emit phonons with high efficiency in polar materials when the electron energy exceeds the phonon energy. The absorption or the emission rate of these phonons depends on the energy of the electrons. In case of highly energetic electrons, the emission rate exceeds the absorption rate, resulting in the transmission of energy of the electrons into the lattice, thereby radiating optical phonons. The hot phonons resulting from these energetic electrons are localized in the region dominated by flow of electrons. Due to small group velocity, these optical phonons do not propagate over large distances and their eventual decay into acoustic phonons generates heat. It is well known that such heating and hot spots limit transistor performance. So, it is important in these kinds of devices to control the heat. It is also important to extract the exact temperature profile in order to monitor the device performance.

Raman spectroscopy is one of the widely used methods to deduce the temperature dependence of the lattice vibrations since the effect of temperature is reflected on phonon vibrations. Approaches like measuring the linewidths or shift in frequencies or the ratio of Stokes/anti-Stokes have been reported for extracting the temperature [111, 112]. In this study, the ratio of Stokes/anti-Stokes peak intensities for precisely calibrating the Raman response in the temperature range of interest has been measured. The resulting experimental calibration curve thus obtained has been verified using the theoretical plot as predicted by Bose-Einstein statistics. Generally, the strongest mode is used to determine the temperature which is the $E_2(\text{high})$. However, as $A_1(\text{LO})$ is an infrared active mode which can produce large polarization and electric field resulting in a strong carrier-optical-phonon scattering and hence

more efficiently relaxing the temperature of hot phonons [113], this mode was also chosen for extracting the temperature along with $E_2(high)$.

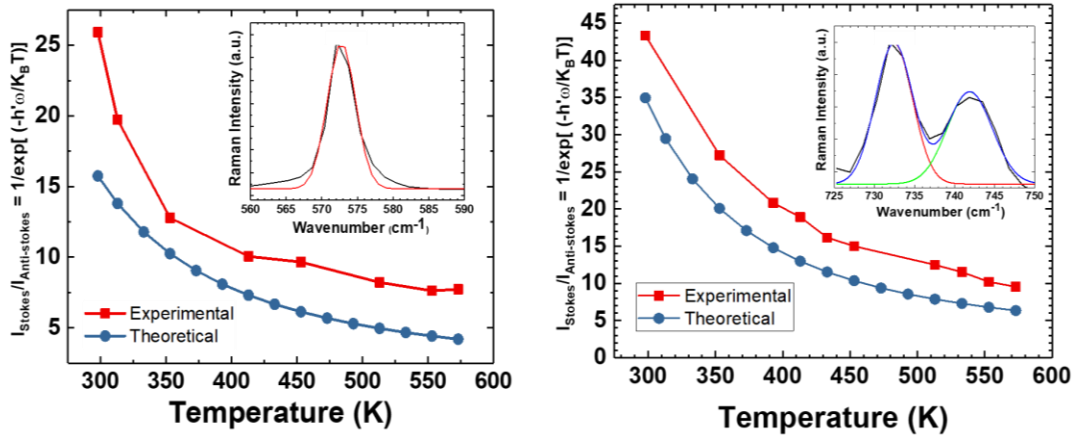


Figure 36 Theoretical and experimental plot of Stokes/Anti-stokes ratio of $E_2(high)$ (left image) and $A_1(LO)$ (right image) as a function of temperature. The inset image shows the gaussian fitted peak of $E_2(high)$ and the deconvoluted peak of $A_1(LO)$ on the Stokes side.

In Raman scattering, phonons may be either emitted or absorbed. These processes are referred to as Stokes and anti-Stokes processes. Following conservation of energy, in case of Stokes process, there is a transfer of energy from the photons to the material (creation), while for anti-Stokes, energy is transferred from material to the photons (annihilation). The ratio of intensities of the Stokes and anti-Stokes lines can be predicted using Bose-Einstein Statistics. Since, the anti-Stokes and Stokes corresponds to the absorption and emission of an optical phonon, their ratio is given by [114]:

$$\frac{I_{AS}}{I_S} = \frac{N_0}{N_0 + 1}$$

Where, N_0 is the equilibrium number of the optical phonon with frequency ω .

$$\text{Since, } N_0 = \left(\exp\left(\frac{\hbar\omega}{k_B T}\right) - 1 \right)^{-1}$$

Therefore, $\frac{I_{AS}}{I_S} = \exp\left(-\frac{\hbar\omega}{K_B T}\right)$

In figure 36 is shown both the theoretical and experimentally obtained temperature calibration curve. The slight deviation in the experimental curve can be attributed to the laser heating or improper distribution of temperature across the sample while heating the sample stage. Nevertheless, this intensity ratio being independent of any stress component [115], it is indeed a very useful and reliable technique for measuring all stress independent temperatures.

6.5 Conclusion

A short period AlN/GaN superlattice with an underlying ternary of $\text{Al}_x\text{Ga}_{1-x}\text{N}$ has been studied using Raman Spectroscopy. The features obtained from the measurements have been identified and assigned to the optical phonon modes from the superlattice structure and the diffused layer of AlN and GaN. It was observed that the Raman spectra from the SL contains modes close in frequency with that of their bulk counterparts along with some additional modes which however are not present in the bulk and has been attributed to the interface phonon modes and phonon modes from the alloy. In addition, Raman spectroscopy, being a non-invasive tool was utilized to measure the temperature dependence of the Stokes/anti-Stokes ratio of the $A_1(LO)$ and $E_2(\text{high})$ mode. This in turn would facilitate accurate modeling and extraction of the temperature distribution in a real device.

7. OPTICAL PROPERTIES OF A SHORT PERIOD ALUMINIUM NITRIDE/GALLIUM NITRIDE SUPERLATTICE UNDER HIGH-EXCITATION AND HIGH TEMPERATURE

7.1 Overview of the chapter

It is quite a well-known fact that AlN/GaN quantum wells and superlattices have been explored for their applications in infrared optoelectronics devices based on intrasubband transitions [116, 117], ultraviolet light emitting devices over a wide range (210nm to 365nm) [118, 119], high electron mobility transistors (HEMT) [120, 121]. The conduction band offset of AlN and GaN is quite large (~2 eV), and thus by optimally controlling the thickness of the layers of these superlattices & heterostructures, it is possible to engineer the operating wavelength of these related devices [122]. These AlN/GaN based devices generally operate both at high temperature and high power. Intense excitation photoluminescence is usually used to study several high-injection devices to explain the underlying device physics. It is therefore relevant and important to study the dynamic behavior of different superlattice/heterostructures both from the aspect of controlling and improving the electrical and optical properties under high excitation and high temperature. Photoluminescence experiments are critical when it comes to interpreting a PL spectrum for understanding carrier dynamics, specially under high-excitation which leads to generation of non-equilibrium electron-holes concentration. In this study a short period AlN/GaN superlattice grown on a thick (800nm) GaN buffer layer deposited a thin 16nm AlN nucleation layer on a sapphire substrate, is excited with high optical injection and its optical properties have been carefully analyzed. The high resistivity GaN buffer layer is used to ensure total pinch off, low losses at high frequencies and right amount of saturation of drain-source

current in a standard HEMT. On the other hand the thin AlN layer is used to reduce strain relaxation along with cracking or defect formation. While at low excitation, the spectra consist of an emission peak from the superlattice, at high excitation a strong low energy peak appears which can be attributed to near band edge emission from the thick underlying GaN buffer layer. Carrier temperature under different excitation densities have been extracted from high energy tail of the PL spectra and analyzed. Furthermore, temperature dependent PL measurements conducted utilizes the radiative recombination model to study the recombination mechanisms.

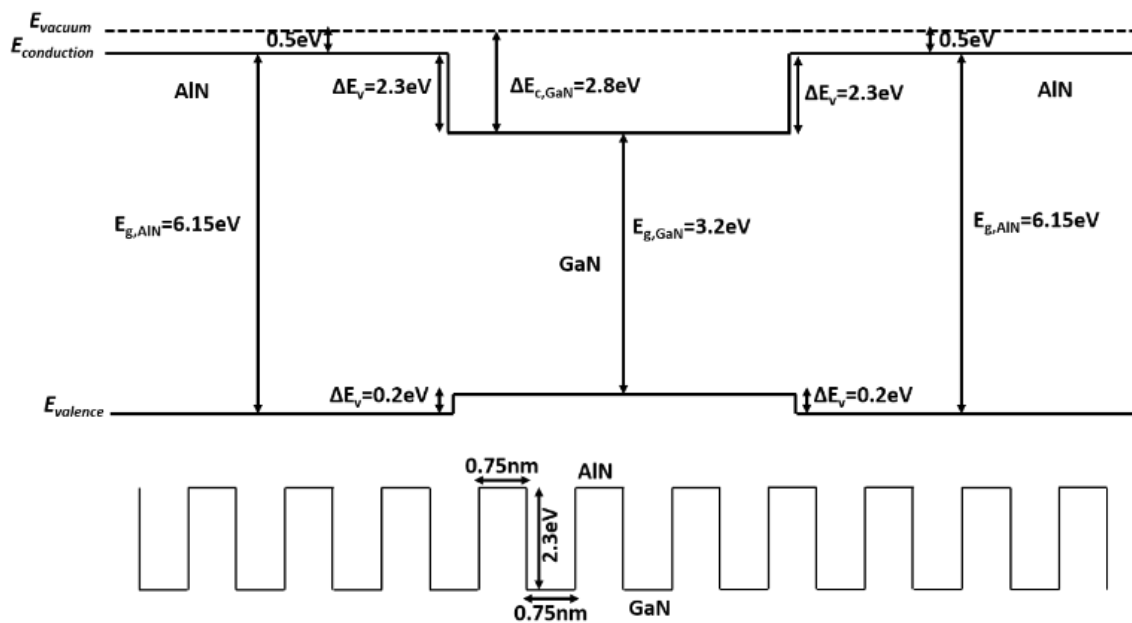


Figure 37 Energy band diagram of a AlN/GaN superlattice showing the offset of conduction and valence band. The energies are calculated with reference to the vacuum energy level which has been set to zero.

7.2 Results and discussions

When a semiconductor is excited with an energy ($h\nu$) greater than the band gap (E_g) of the material, it results in the generation of excess energy (ΔE_e) which is given by

$$\Delta E_e = (h\nu - E_g) * (1 + m_e/m_h)^{-1}$$

where, m_e is the electron effective mass and m_h is the effective masses of holes. It should be noted that while the photoexcited carriers resides in the high energy tail, the rest of the electrons are located at the bottom of the conduction band and are in quasi-equilibrium condition thereby forming electron gas. This photoexcited energetic carriers relax towards a lower energy state by two competing mechanisms i.e. electron-electron scattering and electron-phonon scattering. Under high excitation this relaxation thus leads to generation of hot electrons and phonons [125]. Reviewing the behavior of the SL under such intense excitation and extracting the carrier temperature from it is discussed next.

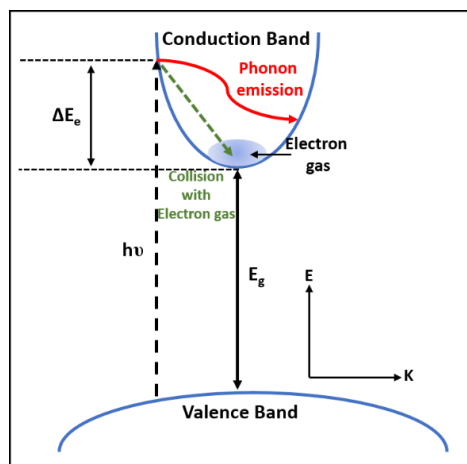


Figure 38 Schematic diagram of different relaxation process under photoexcitation of $h\nu > E_g$

7.2.1 Photoluminescence under high excitation density

Absorption causes the intensity of the light to decay at a rate determined by the material's absorption coefficient α which is a function of wavelength and temperature, but for constant α , intensity I decays exponentially with depth z governed by the Beer–Lambert law [126],

$$I(z) = I_0 e^{-\alpha z}$$

Thus, the penetration depth of an excitation source in any material is primarily dependent on the wavelength of the source. However, increasing the power of these laser source also increase the depth of excitation and allow investigation of a greater depth for the sample. Photoluminescence spectroscopy was carried out to investigate the optical properties of the SL structure. The samples were excited at the edge with a 120fs, 2kHz, 325nm laser source. What is initially observed at lower power in an emission peak at 3.42eV from the top of the superlattice as can be seen from figure 39. This peak from the SLs can be attributed to the interband transitions from the minibands of the superlattice [127, 128]. However, as the power density is increased, the penetration depth of the laser source reaches more into the thick GaN buffer layer. Therefore, an additional low energy peak at 3.36eV is observed with intensity smaller than the original 3.42eV peak. The intensity of this low energy peaks increases further and beyond the emission line from the SLs with increasing excitation density. A gradual red-shift from of this PL peak originating from the GaN buffer is also noticed which can be attributed to band gap renormalization as has been reported in several other studies [129,130]. Similar behavior has also been reported for ZnO epitaxial layers or thin films [131,132]. Although high excitation results in the saturation of any defect states alongside the fact that electronic states are screened by non-equilibrium carriers, the contribution of bound excitonic recombination to this low energy peak cannot be totally ruled out. Bound exciton peaks are generally characterized by

well-defined sharp lines in the spectra with narrow linewidths [133]. However, lattice mismatch resulting in the inhomogeneous distribution of strain might lead to the larger line widths of the peaks. The inset of figure 39 shows the PL spectra on the same sample but excited at the center. It is interesting to observe that the PL emission peak originating from the SLs are stronger than that from the buffer layer for the same excitation density compared to the one excited at the edge. Clearly at the edge of the sample, the thickness of the superlattice is comparatively smaller than the center region which is why stronger peaks are observed from the buffer layer in the former case.

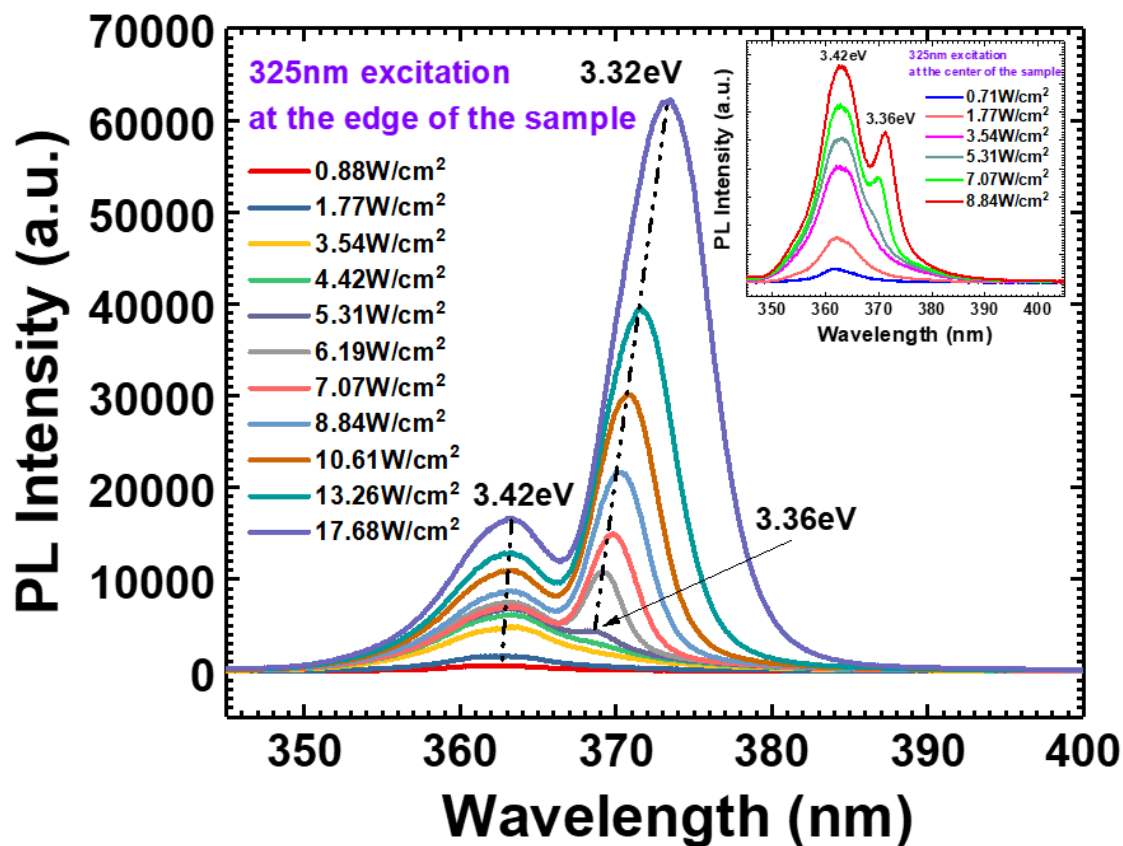


Figure 39 Photoluminescence spectra of AlN/GaN SL at different excitation power with the sample excited at the edge. The inset image shows PL spectra when excited at the center of the sample.

7.2.2 Electron temperature from photoluminescence spectra

Under non-equilibrium condition, if the rate of electron-electron collision is greater than the rate of phonon emission, the population of electron in the electron gas relaxes towards a Maxwell distribution. This distribution can be represented by a temperature T_e [134]. Figure 40 shows the room-temperature photoluminescence spectra measured at different excitation power of the 325nm laser. As can be seen from the spectra, the high energy tail of each of the PL curve varies exponentially as a function of the wavelength, implying the effect of hot-carrier. The following relation is used to express the high-energy tail of a PL spectra:

$$I_{PL} \sim \exp^{-(E-E_g)/KbT}$$

At high photo-excitation, the denominator in the exponential power, represents the kinetic energy of the thermalized electrons and the electron temperature T_e can be extracted.

The carrier temperatures are deduced for each excitation density from the slope of the linear fit of the high energy tail of the photoluminescence spectra. We observe that the carrier temperature increases up to 975K linearly with increase in excitation due to the existence of hot-carrier population, however for power higher than 5 W/cm² a gradual decrease in the temperature of the electrons is observed. These can be explained by analyzing the definitive point of the origin of the PL emission line. Electrons are more confined in the superlattice which is why with increasing excitation density an increase in carrier temperature is observed. It should be noted that the drop in the carrier temperature in figure 40 corresponds to the value of the excitation density for which the emission from the GaN buffer layer shows up in figure 39. Clearly at that threshold value of the power density, the laser intrudes into the buffer layer, thereby distributing the carrier temperature into the buffer layer and emitting a low energy PL peak simultaneously. Thus, a decrease in carrier temperature is observed.

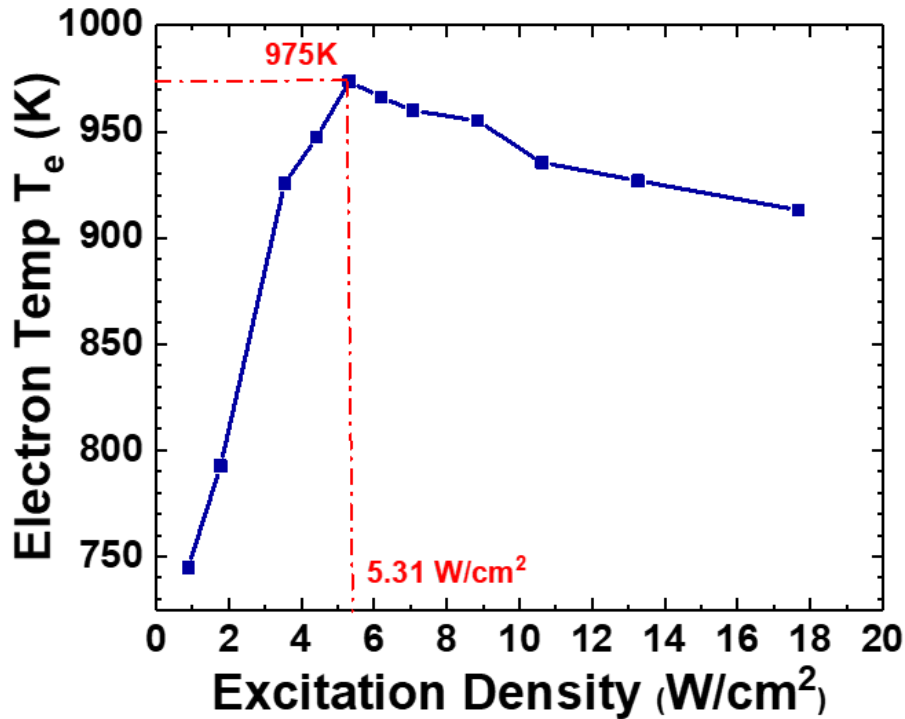


Figure 40 Evolution of the carrier temperature as a function of the laser power

7.2.3 High-temperature PL at different high-power excitation

In this section we discuss about the characteristics of the high temperature PL spectra from the SL by using the radiative recombination model [135]. This model can be expressed as,

$$I_{\text{PL}} = \gamma I_{\text{laser}}^{\alpha},$$

where I_{PL} is the PL intensity, I_{laser} is the excitation intensity, γ is the efficiency of emission and the value of α is used to determine if the nature of recombination is excitonic or band gap recombination. According to this model, if the value of the exponent is 1, then the origin of the light emission from PL is free-excitonic recombination. However, if the value equals 2, then it is the free electron hole recombination i.e. the band gap recombination. For any values of α between 1 and 2, there can be

contribution from both free excitons and free carriers. The purpose of this measurement is thus to gain the understanding of the radiative recombination dynamics of the SL at various high temperatures.

The integrated peak intensity versus laser power obtained from the PL spectra at different temperature to understand the recombination mechanism has been plotted and shown in figure 42. It shows various PL spectra obtained at temperatures from room temperature to all the way up to 150°C for a laser power density of around 4 W/cm². By fitting this data, the value of the exponent α is obtained for different temperatures. As can be seen that it increases from 1.5 to 1.6 as we increase the temperature from room temperature to 150°C. While at room temperature it can be said that free excitonic recombination is more prevalent, however at high temperature, the likelihood of exciton-exciton scattering increases. Because of the small thickness of the superlattice layer, the density of exciton required for exciton-exciton scattering is less, hence conceivable at lower excitation density as compared to a thick epitaxial GaN layer. The shift of the luminescence peak to lower energy as observed from the figure 41 with increase in temperature can be attributed to the thermalization process.

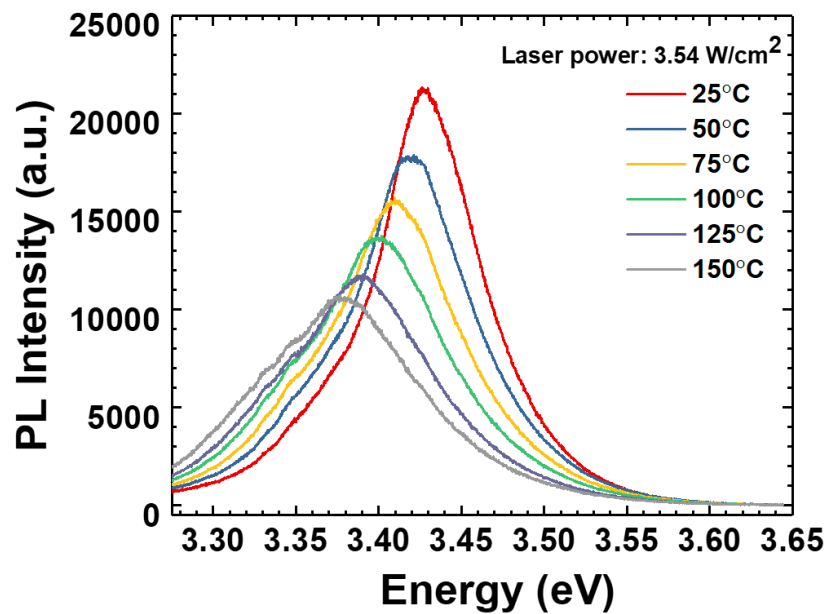


Figure 41 Photoluminescence from SL with 325nm excitation at different high temperatures

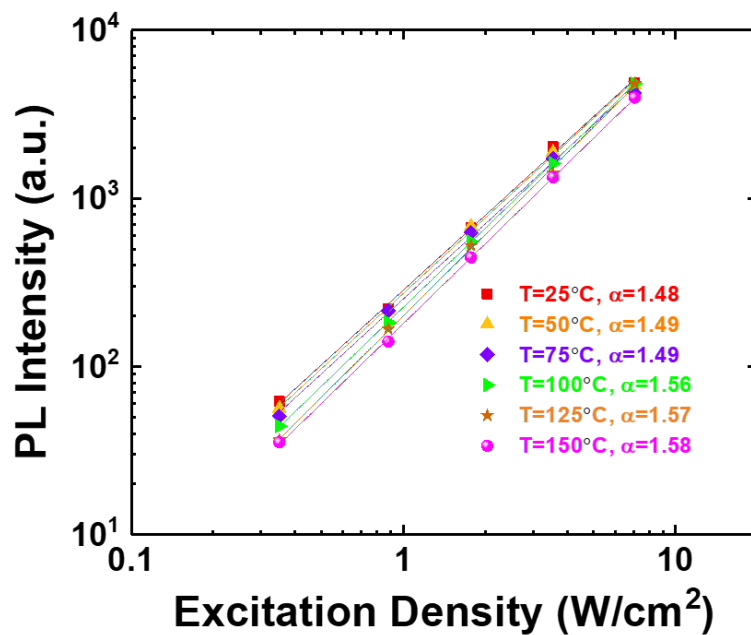


Figure 42 Log-log plot of integrated PL intensity as a function of the laser power at different temperatures

7.3 Time-resolved photoluminescence of SL layer as a function of pump power

As much as understanding the dynamics of any semiconductor is imperative, the knowledge of relaxation time constants is equally important. In the figure below, we have showed time resolved measurements on the SL under different photoexcitation. We have tried to only probe in the shorter time constant range to analyze the faster relaxation time constants. As can be noticed from figure 43, with increase in excitation power, the carriers relax faster towards equilibrium. As we increase the power density from $4\text{W}/\text{cm}^2$ to $10\text{W}/\text{cm}^2$, we see the calculated time constants to decrease from 55ps to 9ps. These time constants are related to the different radiative recombination mechanisms existing at different power densities. With increase in photoexcitation, exciton-exciton scattering increases, thereby the carrier lifetime decreases, hence recombine faster.

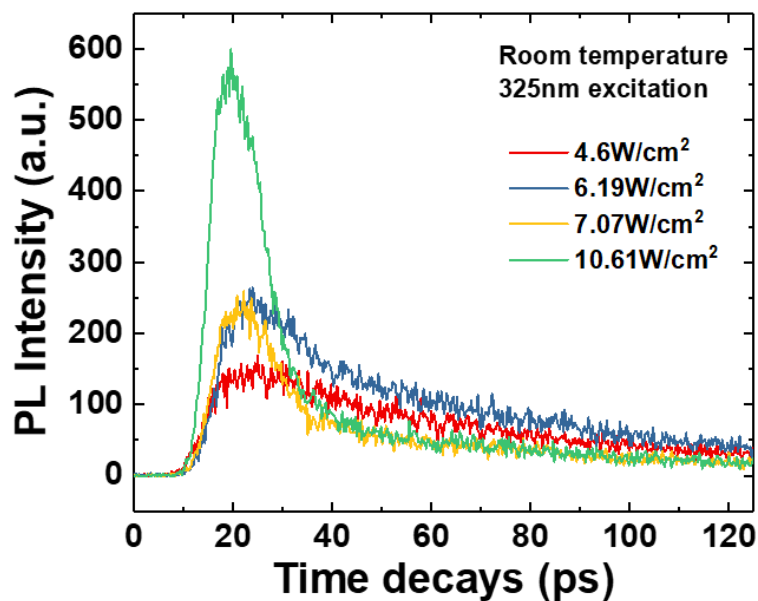


Figure 43 Time resolved photoluminescence spectra measured at room temperature under different excitation intensity

7.4 Conclusion

In summary we have studied the PL of a very short period superlattice applicable for a HEMT device. At high excitation, the peak at the long wavelength is attributed to the band edge emission from the GaN buffer layer, while the shorter wavelength is related to the PL emission from the superlattice. High-energy tail of the PL spectra has been used to measure the distribution of the hot electrons and have been characterized using the parameter T_e . The dependence of the relaxation mechanism on excitation power has been identified and represented. The fact that high excitation implies penetration of the laser deeper into the buffer layer, it results both in the additional low energy PL peak and decrease in the carrier temperature. Under intense excitation, exciton-exciton scattering has been identified to be the dominating process based on the radiative recombination model at different high temperatures.

8. CONCLUSION AND FUTURE WORK

8.1 Conclusion

The principle conclusion drawn from this dissertation can be broadly categorized into two major parts – (a) Studying the carrier dynamics and emission properties of wide band gap zinc oxide nanostructures under the influence of surface treatments and morphology variation, and (b) Optical characterization of a very short period AlN/GaN based superlattice with vision of improving the heating of this structure related devices.

- (a) ZnO nanowires grown using VLS mechanism in an ambient pressure CVD furnace were subjected to surface treatments of two kinds. In the first method, these nanostructures were plasma etched using Ar-plasma in an SEM coater system. In another method, these as - grown nanostructures were sputter coated with metallic nanoparticles in the same system. The resulting near band edge emission from these nanostructures after undergoing these two separate treatments respectively were studied and analyzed. It was observed that in case of plasma etching, by controlling the etching time, the near band edge emission peak can be enhanced considerably while suppressing the visible emission peak simultaneously. The associated mechanism of removal of surface traps which otherwise acts as the non-radiative recombination center have been identified and discussed. While, the sputter coating also resulted in improved NBE emission, it was however found to be trickier in terms of controlling the size and distribution of the nanoparticles on the surface of these ZnO nanostructures. Nevertheless, using the same tool for two different approaches to improving the surface emission properties was quite intriguing. The analysis of the underlying cause of

the suppression of the visible emission due to plasma etching also substantiated the fact that they were caused by surface traps or defects rather than intrinsic oxygen vacancies. Overall the first part of the study reflected the fact that how a simple, cost-efficient method can significantly alter the emission from ZnO which indeed finds applications in several optoelectronic devices.

Furthermore, the study of carrier dynamics using transient absorption spectroscopy in a pump-probe spectroscopy set-up was done to reflect more on the improved optical properties of the surface treated ZnO structures. Utilizing the fact, that pump-probe is a 2-dimensional spectroscopic technique, it was possible to fetch both the spectral and temporal information from the spectra of these ZnO nanostructures. The experimental results from these measurements at different pump fluence showed how surface treatment improved the carrier dynamics as reflected from the increased exciton density and faster relaxation time. These also showed a potential of these surface treated nanostructures to be studied for optical pumping of lasing which was discussed next. A comparative study on the lasing property between the as-grown and plasma treated ZnO nanoribbons transferred on quartz substrate was done. Higher efficiency and lower threshold due to greater density of excitons was observed in the latter case. Adding to the same study was another comparative work on effect of morphology on the intensity of stimulated emission and threshold of the same. Quite obviously it was found that ZnO micro-ribbons with low surface to volume ratio showed higher value for x where x can be defined in term of the laser power (I_p) and stimulated intensity (I_{sp}) as $I_{sp}=I_p^x$. This was because, it had a lower number of surface traps hence larger density of excitons. Conversely, the lower dimensional structures like nanowires and

nanofibers showed a smaller value of x . On the other hand, owing to the requirement for larger pump power to achieve high density of excitons for stimulated emission, the micro-ribbons had a larger threshold.

Another independent study involving In_2O_3 and ZnO was also done where, In_2O_3 nanowires were attempted with doping a higher percentage of Zn. The fact that the growth resulted in co-existing In_2O_3 - ZnO nanowires instead of highly Zn doped In_2O_3 was verified by different characterization techniques. While, SEM and TEM studies gave a visual image of the co-existing nature, EDX and XPS measurements showed the presence of individual In, Zn and O. Finally, spectra obtained photoluminescence spectroscopy and Raman spectroscopy individually established the fact that the structures were existing separately and not as highly-doped structures.

- (b) GaN and AlN are one of the highly studied materials of group III nitrides. What is interesting, is that the dispersion curve of the heterostructures of these materials is overlapped versions of the individual curves of GaN and AlN resulting in different lattice dynamics. A short period AlN/GaN superlattice with an underlying AlGaIn ternary grown on a GaN buffer layer on a Sapphire substrate excited with a 514nm laser source resulted in a Raman spectrum consisting of several modes. The significant modes of $E_2(\text{high})$, $A_1(\text{LO})$ and $E_1(\text{TO})$ were observed Stokes shifted than the original modes of the characterizing bulk material i.e. GaN and AlN. These modes originated from the SL structure and are believed to be a function of the composition and structure of the superlattice. The additional band of peak in the mid-frequency regions from 560 to 660 cm^{-1} were associated with the interface phonon modes from these heterostructures based on the theoretical modeling on this short period superlattice

and literature review and from the one-mode and two-mode phonons of the underlying binary structure. The Stokes/anti-Stokes ratio of the infra-red active $A_1(LO)$ mode was measured as a function of high temperature. Although, the extensive nature of the measurement of Stokes/anti-Stokes ratio including the long integration time makes it a tedious job, however the simplistic theory makes it a useful method in the extraction of temperature using this stress-independent Raman measurement. A close agreement between the theoretical and experimental plot was obtained for the $A_1(LO)$ mode which is believed to provide a good calibration platform for temperature measurement on future devices based on this superlattice structure.

The same structure was further subjected to high density photo-excitation and high-temperature to understand the optical behavior of the superlattice. At lower laser density spontaneous emission peaks from the superlattice were observed. However, after a certain threshold value of the power density, a low energy peak corresponding to the near band edge emission from the lower GaN buffer layer was observed. This was observed simultaneously with a drop in the carrier temperature due to distribution of the heat in to the thick buffer layer at high laser power. This behavior highlights the cut-off range of the excitation density for this specific short period AlN/GaN superlattice before it can protrude into the underlying layers. Transition of the photoluminescence peak of the SL from free-exciton to exciton-exciton was observed with increasing temperature. Overall, a general idea about the emission from the SL has been projected in this specific work which is believed to be helpful for future work on device applications based on this short period superlattice structure.

8.2 Future Work

Based on the main conclusion drawn from the thesis, the following ideas can be recommended for the continuation of this research work. These future works are briefly outlined as follows:

- While photonics lasers based on ZnO has been extensively studied, the work on plasmonic lasers based on surface plasmon resonance of metallic nanoparticles on ZnO is relatively new. Metals like Au, Ag or Al have been utilized for the fabrication of plasmonic lasers with ZnO. In this regard and going with the flow with the work described in the first part of this thesis, some more developments can be contributed to this field. One of such ideas could be to fabricate and demonstrate this plasmonic lasers using the plasma etched ZnO nanostructures and simultaneously doing a comparative study using different metals.
- An interesting continuation to the work described in Chapter 5 would be to demonstrate those co-existing structures as gas sensors. Both ZnO and In_2O_3 have been tested individually for gas sensing. But to look at their heterostructures or something like what described in this thesis in perspective of enhanced gas sensing and lowered detection limit could be intriguing.
- The idea of a superlattice structure for a HEMT as discussed in Chapter 6 & 7 was to have interface phonon modes for smearing the heat out of the channel. However, one drawback for having multiple interfaces is the more resistance, hence lower thermal conductivity and lower transport velocity of the acoustic phonons. This means slower and less transport of heat. Thus, one recommendation for future work could be to design a quantum well structure but having an AlN layer right below the location of 2DEG or hotspot i.e. a standard AlGaN/AlN/GaN structure with back gating perhaps so that the property of interface phonons for good heat transport can be utilized without compromising the thermal conductivity or velocity.

APPENDICES

APPENDIX A

Chapter 3, Page 26-34 and 36-39 have been reproduced from my own article submitted to *Nanotechnology*:

“Ultrafast carrier dynamics and optical pumping of lasing from Ar plasma treated ZnO nanoribbons”, Ketaki Sarkar, Souvik Mukherjee, Gary Wiederrecht, Richard D Schaller, David J Gosztola, Michael A Stroschio and Mitra Dutta, (currently under review).

Chapter 4, Page 40, has been reproduced from my accepted presentation at 2017 Fall Meeting of the APS Prairie Section, November 11-12, 2017, University of Illinois at Chicago, Chicago, IL

“Stimulated emission and optical pumping of lasing from ZnO nanostructures: effect of morphology and surface treatment”, Ketaki Sarkar, Richard D Schaller, Michael A Stroschio and Mitra Dutta.

Chapter 5, Page 53-66, has been reproduced from my own published article in *Journal of Electronic Materials* as:

“Characterization of Co-existing In₂O₃-ZnO Nanostructures, Characterization of Co-existing In₂O₃-ZnO Nanostructures”, K. Sarkar, S. Mukherjee, S. Farid, A. Nicholls, M. A. Stroschio, M. Dutta, *Journal of Elec Materi* (2017) 46: 5848.

Chapter 6, Page 67-76, has been reproduced closely from my own article to be submitted to *Superlattices and Microstructures* as:

“Raman analysis of phonon modes in a short period AlN/GaN superlattice”, Ketaki Sarkar, Debopam Datta, David J Gosztola, Michael A Stroschio and Mitra Dutta.

APPENDIX B

11/17/2017

RightsLink Printable License

SPRINGER LICENSE TERMS AND CONDITIONS

Nov 17, 2017

This Agreement between University of Illinois at Chicago -- Ketaki Sarkar ("You") and Springer ("Springer") consists of your license details and the terms and conditions provided by Springer and Copyright Clearance Center.

License Number	4231410365744
License date	Nov 17, 2017
Licensed Content Publisher	Springer
Licensed Content Publication	Journal of Electronic Materials
Licensed Content Title	Characterization of Co-existing In ₂ O ₃ -ZnO Nanostructures
Licensed Content Author	K. Sarkar, S. Mukherjee, S. Farid et al
Licensed Content Date	Jan 1, 2017
Licensed Content Volume	46
Licensed Content Issue	10
Type of Use	Thesis/Dissertation
Portion	Full text
Number of copies	1
Author of this Springer article	Yes and you are a contributor of the new work
Order reference number	
Title of your thesis / dissertation	Study of Wide-Band Gap Oxide and Nitride Based Semiconductors: Characterization and Device Physics
Expected completion date	Dec 2017
Estimated size(pages)	130
Requestor Location	University of Illinois at Chicago 851 South Morgan St M/C 154 1020 SEO CHICAGO, IL 60607 United States Attn: University of Illinois at Chicago
Billing Type	Invoice
Billing Address	University of Illinois at Chicago 851 South Morgan St M/C 154 1020 SEO CHICAGO, IL 60607 United States Attn: University of Illinois at Chicago
Total	0.00 USD
Terms and Conditions	

Introduction

The publisher for this copyrighted material is Springer. By clicking "accept" in connection

APPENDIX B (continued)

11/17/2017

RightsLink Printable License

with completing this licensing transaction, you agree that the following terms and conditions apply to this transaction (along with the Billing and Payment terms and conditions established by Copyright Clearance Center, Inc. ("CCC"), at the time that you opened your Rightslink account and that are available at any time at <http://myaccount.copyright.com>).

Limited License

With reference to your request to reuse material on which Springer controls the copyright, permission is granted for the use indicated in your enquiry under the following conditions:

- Licenses are for one-time use only with a maximum distribution equal to the number stated in your request.

- Springer material represents original material which does not carry references to other sources. If the material in question appears with a credit to another source, this permission is not valid and authorization has to be obtained from the original copyright holder.

- This permission

- is non-exclusive
- is only valid if no personal rights, trademarks, or competitive products are infringed.
- explicitly excludes the right for derivatives.
- Springer does not supply original artwork or content.

- According to the format which you have selected, the following conditions apply accordingly:

• **Print and Electronic:** This License include use in electronic form provided it is password protected, on intranet, or CD-Rom/DVD or E-book/E-journal. It may not be republished in electronic open access.

• **Print:** This License excludes use in electronic form.

• **Electronic:** This License only pertains to use in electronic form provided it is password protected, on intranet, or CD-Rom/DVD or E-book/E-journal. It may not be republished in electronic open access.

For any electronic use not mentioned, please contact Springer at permissions.springer@spi-global.com.

- Although Springer controls the copyright to the material and is entitled to negotiate on rights, this license is only valid subject to courtesy information to the author (address is given in the article/chapter).

- If you are an STM Signatory or your work will be published by an STM Signatory and you are requesting to reuse figures/tables/illustrations or single text extracts, permission is granted according to STM Permissions Guidelines: <http://www.stm-assoc.org/permissions-guidelines/>

For any electronic use not mentioned in the Guidelines, please contact Springer at permissions.springer@spi-global.com. If you request to reuse more content than stipulated in the STM Permissions Guidelines, you will be charged a permission fee for the excess content.

Permission is valid upon payment of the fee as indicated in the licensing process. If permission is granted free of charge on this occasion, that does not prejudice any rights we might have to charge for reproduction of our copyrighted material in the future.

-If your request is for reuse in a Thesis, permission is granted free of charge under the following conditions:

This license is valid for one-time use only for the purpose of defending your thesis and with a maximum of 100 extra copies in paper. If the thesis is going to be published, permission needs to be reobtained.

- includes use in an electronic form, provided it is an author-created version of the thesis on his/her own website and his/her university's repository, including UMI (according to the definition on the Sherpa website: <http://www.sherpa.ac.uk/romeo/>);

- is subject to courtesy information to the co-author or corresponding author.

Geographic Rights: Scope

Licenses may be exercised anywhere in the world.

APPENDIX B (continued)

11/17/2017

RightsLink Printable License

Altering/Modifying Material: Not Permitted

Figures, tables, and illustrations may be altered minimally to serve your work. You may not alter or modify text in any manner. Abbreviations, additions, deletions and/or any other alterations shall be made only with prior written authorization of the author(s).

Reservation of Rights

Springer reserves all rights not specifically granted in the combination of (i) the license details provided by you and accepted in the course of this licensing transaction and (ii) these terms and conditions and (iii) CCC's Billing and Payment terms and conditions.

License Contingent on Payment

While you may exercise the rights licensed immediately upon issuance of the license at the end of the licensing process for the transaction, provided that you have disclosed complete and accurate details of your proposed use, no license is finally effective unless and until full payment is received from you (either by Springer or by CCC) as provided in CCC's Billing and Payment terms and conditions. If full payment is not received by the date due, then any license preliminarily granted shall be deemed automatically revoked and shall be void as if never granted. Further, in the event that you breach any of these terms and conditions or any of CCC's Billing and Payment terms and conditions, the license is automatically revoked and shall be void as if never granted. Use of materials as described in a revoked license, as well as any use of the materials beyond the scope of an unrevoked license, may constitute copyright infringement and Springer reserves the right to take any and all action to protect its copyright in the materials.

Copyright Notice: Disclaimer

You must include the following copyright and permission notice in connection with any reproduction of the licensed material:

"Springer book/journal title, chapter/article title, volume, year of publication, page, name(s) of author(s), (original copyright notice as given in the publication in which the material was originally published) "With permission of Springer"

In case of use of a graph or illustration, the caption of the graph or illustration must be included, as it is indicated in the original publication.

Warranties: None

Springer makes no representations or warranties with respect to the licensed material and adopts on its own behalf the limitations and disclaimers established by CCC on its behalf in its Billing and Payment terms and conditions for this licensing transaction.

Indemnity

You hereby indemnify and agree to hold harmless Springer and CCC, and their respective officers, directors, employees and agents, from and against any and all claims arising out of your use of the licensed material other than as specifically authorized pursuant to this license.

No Transfer of License

This license is personal to you and may not be sublicensed, assigned, or transferred by you without Springer's written permission.

No Amendment Except in Writing

This license may not be amended except in a writing signed by both parties (or, in the case of Springer, by CCC on Springer's behalf).

Objection to Contrary Terms

Springer hereby objects to any terms contained in any purchase order, acknowledgment, check endorsement or other writing prepared by you, which terms are inconsistent with these terms and conditions or CCC's Billing and Payment terms and conditions. These terms and conditions, together with CCC's Billing and Payment terms and conditions (which are incorporated herein), comprise the entire agreement between you and Springer (and CCC) concerning this licensing transaction. In the event of any conflict between your obligations established by these terms and conditions and those established by CCC's Billing and Payment terms and conditions, these terms and conditions shall control.

APPENDIX B (continued)

11/17/2017

RightsLink Printable License

Jurisdiction

All disputes that may arise in connection with this present License, or the breach thereof, shall be settled exclusively by arbitration, to be held in the Federal Republic of Germany, in accordance with German law.

Other conditions:

V 12AUG2015

Questions? customer@copyright.com or +1-855-239-3415 (toll free in the US) or +1-978-646-2777.

CITED LITERATURE

- [1] C. N. R. Rao, A. Muller, A. K. Cheetham “The Chemistry of Nanomaterials- Synthesis, Properties and Applications” *Wiley-VCH Verlag GmbH & Co. KGaA*, 2004.
- [2] Cui, Y., Zhong, Z., Wang, D., Wang, W. U., & Lieber, C. M. “High performance silicon nanowire field effect transistors” *Nano letters*, 3(2), 149-152, 2003.
- [3] C. Thelander, P. Agarwal, S. Brongersma, J. Eymery, L. F. Feiner, A. Forchel, M. Scheffler, W. Riess, B. J. Ohlsson, U. Gösele, and L. Samuelson, “Nanowire-based one-dimensional electronics” *Materials Today*, vol. 9, p. 28, 2006.
- [4] M. C. McApline, H. Ahmad, D. Wang and J. R. Heath, “Highly ordered nanowire arrays on plastic substrates for ultrasensitive flexible chemical sensors” *Nature Materials*, vol. 6, p. 379, 2007.
- [5] Chen, X., Wong, C. K., Yuan, C. A., & Zhang, G. (2013). “Nanowire-based gas sensors” *Sensors and Actuators B: Chemical*, 177, 178-195, 2013.
- [6] Kind, H., Yan, H., Messer, B., Law, M., & Yang, P. “Nanowire ultraviolet photodetectors and optical switches” *Advanced materials*, 14(2), 158, 2002.
- [7] Bae, S.-H., Lee, S., Koo, H., Lin, L., Jo, B. H., Park, C. and Wang, Z. L. “The Memristive Properties of a Single VO₂ Nanowire with Switching Controlled by Self-Heating” *Adv. Mater.*, 25: 5098–5103, 2013.
- [8] Johnson, J. C., Choi, H. J., Knutsen, K. P., Schaller, R. D., Yang, P., & Saykally, R. J. “Single gallium nitride nanowire lasers” *Nature materials*,1(2), 106-110, 2002.
- [9] Justin C. Johnson, Heon-Jin Choi, Kelly P. Knutsen, Richard D. Schaller, Peidong Yang & Richard J. Saykally, “Single gallium nitride nanowire lasers” *Nature Materials* 1, 106 - 110 (2002).

CITED LITERATURE (continued)

- [10] Lu, W., & Lieber, C. M. "Nanoelectronics from the bottom up" *Nature materials*, 6(11),841-850, 2007.
- [11] Farid. S, "Characterization of CdTe Based Photodetectors, ZnO Nanowires and Nanostructures for Photonic Applications" (Doctoral dissertation, University of Illinois at Chicago).
- [12] Silicon Carbide: Smaller, Faster, Tougher. IEEE Spectrum, October 2011.
- [13] Jun Suda, "Special issue on wide-bandgap semiconductor power electronics" *Semicond. Sci. Technol.* 31 (2016) 030301.
- [14] Wang, Z. L. "Zinc oxide nanostructures: growth, properties and applications". *Journal of Physics: Condensed Matter*, 16(25), R829, 2004.
- [15] Johnson W., Piner E.L. "GaN HEMT Technology. In: Pearton S. (eds) GaN and Zn based Materials and Devices" *Springer Series in Materials Science*, vol 156. Springer, Berlin, Heidelberg, 2012.
- [16] Arnold M S, Avouris Ph, Pan Z W and Wang Z L, J. "Field-Effect Transistors Based on Single Semiconducting Oxide Nanobelts" *Phys. Chem. B* 107 659, 2003.
- [17] Alla Tereshchenko, Mikhael Bechelany, Roman Viter, Volodymyr Khranovskyy, Valentyn Smyntyna, Nikolay Starodub, Rositza Yakimova, "Optical biosensors based on ZnO nanostructures: advantages and perspectives" *Sensors and Actuators B: Chemical*, Volume 229, Pages 664-677, 2016.
- [18] Bian X, Jin H, Wang X, Dong S, Chen G, Luo J. K, Deen M. Jamal, Qi B, "UV sensing using film bulk acoustic resonators based on Au/n-ZnO/piezoelectric-ZnO/Al structure" *Scientific Reports* 5, Article number: 9123, 2015.

CITED LITERATURE (continued)

- [19] Tsukazaki, A., Ohtomo, A., Onuma, T., Ohtani, M., Makino, T., Sumiya, M., ... & Kawasaki, M., "Repeated temperature modulation epitaxy for p-type doping" *Nature materials*, 4(1), 42-46, 2005.
- [20] Sunandan Baruah and Joydeep Dutta, "Hydrothermal growth of ZnO nanostructures" *Sci. Technol. Adv. Mater.* 10 013001, 2009.
- [21] Baek Hyun Kim & Jae W. Kwon, "Metal Catalyst for Low-Temperature Growth of Controlled Zinc Oxide Nanowires on Arbitrary Substrates" *Scientific Reports* 4, Article number: 4379, 2014.
- [22] Mohammad R. Alenezi, Simon J. Henley & S. R. P. Silva, "On-chip Fabrication of High Performance Nanostructured ZnO UV Detectors" *Scientific Reports* 5, Article number: 8516, 2015.
- [23] Zhengrong R. Tian, James A. Voigt, Jun Liu¹, Bonnie Mckenzie, Matthew J. Mcdermott, Mark A. Rodriguez, Hiromi Konishi and Huifang Xu, "Complex and oriented ZnO nanostructures" *Nature Materials* 2, 821 – 826, 2003.
- [24] Justin C. Johnson, Haoquan Yan, Richard D. Schaller, Louis H. Haber, Richard J. Saykally and Peidong Yang, "Single Nanowire Lasers" *J. Phys. Chem. B*, Vol. 105, No. 46, 11389, 2001.
- [25] Xiangfeng Duan, Yu Huang, Ritesh Agarwal & Charles M. Lieber, "Single-nanowire electrically driven lasers" *Nature* Vol, 421, 16 January 2003.
- [26] Baratto C, Comini E, Ferroni M, Faglia G and Sberveglieri G, "Plasma-induced enhancement of UV photoluminescence in ZnO nanowires" *Cryst Eng Comm.* 15 7981, 2013.
- [27] Yadian B, Chen R, Liu H, Sun H, Liu Q, Gan C L, Kun Z, Zhao C, Zhu B and Huang Y "Significant enhancement of UV emission in ZnO nanorods subject to Ga⁺ ion beam irradiation" *Nano Res.* 8 6 1857–1864, 2015.

CITED LITERATURE (continued)

- [28] Liu K W, Chen R, Xing G Z, Wu T and Sun H D, "Photoluminescence characteristics of high quality ZnO nanowires and its enhancement by polymer covering" *Appl. Phys. Lett.* 96 023111, 2010.
- [29] Johnson J C, Knutsen K P, Yan H, Law M, Zhang Y, Yang P and Saykally R J, "Ultrafast Carrier Dynamics in Single ZnO Nanowire and Nanoribbon Lasers" *Nano Lett.* 4 2 197-204, 2004.
- [30] Mehl B P, Kirschbrown J R, Gabriel M M, House R L and Papanikolas J M, "Pump-Probe Microscopy Spatially Resolved Carrier Dynamics in ZnO rods" *J. Phys. Chem. B* 117 4390-4398, 2013.
- [31] T. Shih, E. Mazur, J.-P. Richters, J. Gutowski, and T. Voss, "Ultrafast exciton dynamics in ZnO: Excitonic versus electron-hole plasma lasing" *Journal of Applied Physics* 109, 043504, 2011.
- [32] Tobias Voss, Jan-Peter Richters, and Apurba Dev, "Surface effects and nonlinear optical properties of ZnO nanowires" *Phys. Status Solidi B* 247, No. 10, 2476-2487, 2010.
- [33] Ney H. Moreira, Ba'lint Aradi, Andreia L. da Rosa, and Thomas Frauenheim, "Native Defects in ZnO Nanowires: Atomic Relaxations, Relative Stability, and Defect Healing with Organic Acids" *J. Phys. Chem. C*, 114, 18860-18865, 2010.
- [34] Ü. Özgür, Ya. I. Alivov, C. Liu, A. Teke, M. A. Reshchikov, S. Doğan, V. Avrutin, S.-J. Cho, and H. Morkoç, "A comprehensive review of ZnO materials and devices" *Journal of Applied Physics*, 98, 041301, 2005.
- [35] Zhiyong Fan and Jia G. Lu, "Zinc Oxide Nanostructures: Synthesis and Properties" *Journal of Nanoscience and Nanotechnology*, Vol.5, 1-13, 2005.
- [36] W. F. Zhang, Z. B. He, G. D. Yuan, J. S. Jie, L. B. Luo, X. J. Zhang, Z. H. Chen, C. S. Lee, W. J. Zhang, and S. T. Lee, "High-performance, fully transparent, and flexible zinc-doped indium oxide nanowire transistors" *Applied Physics Letters* 94, 123103, 2009.

CITED LITERATURE (continued)

- [37] Z. P. Wei, D. L. Guo, B. Liu, R. Chen, L. M. Wong, W. F. Yang, S. J. Wang, H. D. Sun and T. Wu, "Ultraviolet light emission and excitonic fine structures in ultrathin single-crystalline indium oxide nanowires" *Applied Physics Letters* 96, 031902, 2010.
- [38] C. L. Hsin, J. H. He, and L. J. Chen, "Modulation of photoemission spectra of In_2O_3 nanowires by the variation in Zn doping level" *Applied Physics Letters* 88, 063111, 2006.
- [39] J. Gao, R. Chen, D.H. Li, L. Jiang, J.C. Ye, X.C. Ma, X.D. Chen, Q.H. Xiong, H.D. Sun, and T. Wu, "UV light emitting transparent conducting tin-doped indium oxide (ITO) nanowires", *Nanotechnology*, 22, 195706, 2011.
- [40] K. Santra and C.K. Sarkar, "Energy-loss rate of hot carriers in semiconductors with nonequilibrium phonon distribution in the extreme quantum limit at low temperatures" *Phys. Rev. B*, 47, 3598, 1993.
- [41] N. Bannov, V. Aristov, V. Mitin, and M. A. Stroscio, "Electron relaxation times due to the deformation-potential interaction of electrons with confined acoustic phonons in a free-standing quantum well" *Phys. Rev. B* 51, 9930 – Published 15 April 1995.
- [42] R. Mickevicius, V. Mitin, V. Kochelap, M. A. Stroscio, and G. J. Iafrate, "Radiation of acoustic phonons from quantum wires" *J. Appl. Phys.* 77(10), 5095, 1995.
- [43] A. R. Bhatt, K. W. Kim, M. A. Stroscio, G. J. Iafrate, M. Dutta, H. L. Grubin, R. Haque, and X. T. Zhu, "Reduction of interface phonon modes using metal-semiconductor heterostructures" *J. Appl. Phys.* 73, 2338, 1993.
- [44] K. W. Kim, M. A. Littlejohn, M. A. Stroscio, and G. J. Iafrate, "Transition from LO-phonon to SO-phonon scattering in mesoscale structures" *Semicond. Sci. Technol.* 7, B49, 1992.
- [45] H.-P. Lee¹, J. Perozek¹, L. D. Rosario & C. Bayram, "Investigation of AlGaN/GaN high electron mobility transistor structures on 200-mm silicon (111) substrates employing different buffer layer configurations" *Scientific Reports* 6, Article number: 37588, 2016.

CITED LITERATURE (continued)

- [46] Makoto Miyoshi, Takashi Egawa, Hiroyasu Ishikawa, Kei-Ichiro Asai, Tomohiko Shibata, Mitsuhiro Tanaka, and Osamu Oda, "Nanostructural characterization and two-dimensional electron-gas properties in highmobility heterostructures grown on epitaxial AlN/sapphire templates" *Journal of Applied Physics* 98, 063713, 2005.
- [47] Cao Guozhong, "Nanostructures and Nanomaterials: Synthesis, Properties and Applications" *World Scientific*, 2004.
- [48] A. Anderson, "The Raman effect", Vol. 1: *Principles*, *Marcel Dekker Inc.*, New York, 1971.
- [49] Liao Z M, Zhang H Z, Zhou Y B, Xua J, Zhang J M and Yua D P, "Surface effects on photoluminescence of single ZnO nanowires" *Physics Letters A* 372 4505–4509, 2009.
- [50] Huang M H, Mao S, Feick H, Yan H, Wu Y, Kind H, Weber E, Russo R and Yang P "Room-Temperature Ultraviolet Nanowire Nanolasers" *Science* 292 5523 1897-1899, 2001.
- [51] Soci C, Zhang A, Xiang B, Dayeh S A, Aplin D P R, Park J, Bao X Y, Lo Y H and Wang D, "ZnO Nanowire UV Photodetectors with High Internal Gain" *Nano Lett.* 7 4 1003-1009, 2007.
- [52] Kind H, Yan H, Messer B, Law M and Yang P, "Nanowire Ultraviolet Photodetectors and Optical Switches" *Adv. Mater.* 14 2 158-160, 2002.
- [53] Cheng C W, Sie E J, Liu B, Huan C H A, Sum T C, Sun H D and Fan H J, "Surface plasmon enhanced band edge luminescence of ZnO nanorods by capping Au nanoparticles" *Applied Physics Letters* 96 071107, 2010.
- [54] Lin J M, Lin H Y, Cheng C L and Chen Y F, "Giant enhancement of bandgap emission of ZnO nanorods by platinum nanoparticles" *Nanotechnology* 17 4391–4394, 2006.

CITED LITERATURE (continued)

- [55] Bergman L, Dutta M, and Nemanich R J “Raman Scattering Spectroscopy and Analyses of III-V Nitride-Based Materials” *Raman Scattering in Materials Science* ed. Weber W H and Merlin R (Berlin: Springer-Verlag) 42 273–313, 2000.
- [56] Sarkar K, Mukherjee S, Farid S, Nicholls A, Stroschio M A and Dutta M, “Characterization of Co-existing In₂O₃-ZnO Nanostructures” *Journal of Electronic Material* 46 10 5848-5854, 2017.
- [57] Lupan O, Chow L, Ono L K, Cuenya B R, Chai G, Khallaf H, Park S and Schulte A, “Synthesis and Characterization of Ag- or Sb-Doped ZnO Nanorods by a Facile Hydrothermal Route” *J. Phys.Chem.* 114 12401-12408, 2010.
- [58] Janotti A and Van de Walle C G, “Native point defects in ZnO” *Physical Review B* 76 165202, 2007.
- [59] Farid S, Mukherjee S, Sarkar K, Mazouchi M, Stroschio M A and Dutta M, “Enhanced optical properties due to indium incorporation in zinc oxide nanowires” *Appl. Phys. Lett.* 108 021106, 2016.
- [60] Janotti A and Van de Walle C G, “Fundamentals of zinc oxide as a Semiconductor” *Rep. Prog. Phys.* 72 126501, 2009.
- [61] Lin B, Fu Z and Jia Y, “Green luminescent center in undoped zinc oxide films deposited on silicon substrates” *Appl. Phys. Lett.* 79 943, 2001.
- [62] Chen C, He H, Lu Y, Wu K and Ye Z, “Surface Passivation Effect on the Photoluminescence of ZnO nanorods” *ACS Appl. Mater. Interfaces* 5 6354–6359, 2013.
- [63] Dev A, Niepelt R, Richters J P, Ronning C and Voss T, “Stable enhancement of near-band-edge emission of ZnO nws by hydrogen incorporation” *Nanotechnology* 21 065709, 2010.

CITED LITERATURE (continued)

- [64] Dev A, Richters J P, Sartor J, Kalt H, Gutowski J and Voss T, "Enhancement of the near-band-edge photoluminescence of ZnO nanowires: Important role of hydrogen incorporation versus plasmon resonances" *Appl. Phys. Lett.* 98 131111, 2011.
- [65] Purahmad M, Stroschio M A and Dutta M, "Strong Enhancement of Near-Band-Edge Photoluminescence of ZnO Nanowires Decorated with Sputtered Metallic Nanoparticles" *Journal of Electronic Material* 43 3 740-745, 2014.
- [66] Myung-Ki Lee, Tae Geun Kim, Woong Kim and Yun-Mo Sung, "Surface Plasmon Resonance (SPR) Electron and Energy Transfer in Noble Metal-Zinc Oxide Composite Nanocrystals" *J. Phys. Chem. C*, 112, 10079-10082, 2008.
- [67] C. W. Cheng, E. J. Sie, B. Liu, C. H. A. Huan, T. C. Sum, H. D. Sun, and H. J. Fan, "Surface plasmon enhanced band edge luminescence of ZnO nanorods by capping Au nanoparticles" *Applied Physics Letters* 96, 071107, 2010.
- [68] T Chen, G Z Xing, Z Zhang, H Y Chen and T Wu, "Tailoring the photoluminescence of ZnO nanowires using Au nanoparticles" *Nanotechnology*, 19, 435711, 2008.
- [69] Narendar Gogurla, Arun Kumar Sinha, Sumita Santra, Santanu Manna & Samit Kumar Ray, "Multifunctional Au-ZnO Plasmonic Nanostructures for Enhanced UV Photodetector and Room Temperature NO Sensing Devices" *Scientific Reports*, 4, 6483, 2014.
- [70] Song J K, Willer U, Szarko J M, Leone S R, Li S and Zhao Y, "Ultrafast Upconversion Probing of Lasing Dynamics in Single ZnO Nanowire Lasers" *J. Phys. Chem. C* 112 1679-1684, 2008.
- [71] Bagnall D M, Chen Y F, Zhu Z, Yao T, Koyama S, Shen M Y and Goto T, "Optically pumped lasing of ZnO at room temperature" *Appl. Phys. Lett.* 70, 2230, 1997.
- [72] C. Kligshirn, "The Luminescence of ZnO under High One- and Two-Quantum Excitation" *Phys. Status Solidi B* 71, 547, 1975.

CITED LITERATURE (continued)

- [73] W. M. Kwok, Y. H. Leung, A. B. Djurišić, W. K. Chan, and D. L. Phillips, "Time-resolved photoluminescence study of the stimulated emission in ZnO nanoneedles" *Appl. Phys. Lett.* 87, 093108, 2005.
- [74] Marcel Wille, Chris Sturm, Tom Michalsky, Robert Röder, Carsten Ronning, Rüdiger Schmidt-Grundl and Marius Grundmann, "Carrier density driven lasing dynamics in ZnO nanowires" *Nanotechnology* 27, 225702, 2016.
- [75] N. Singh, A. Ponzoni, E. Comini, P.S. Lee, "Chemical sensing investigations on Zn–In₂O₃ nanowires" *Sens. Actuators, B* 171, 244, 2012.
- [76] W.F. Zhang, Z.B. He, G.D. Yuan, J.S. Jie, L.B. Luo, X.J. Zhang, Z.H. Chen, C.S. Lee, W.J. Zhang, S.T. Lee, "High-performance, fully transparent, and flexible zinc-doped indium oxide nanowire transistors" *Appl. Phys. Lett.* 94, 123103, 2009.
- [77] W. Zhang, J. Jie, Z. He, S. Tao, X. Fan, Y. Zhou, G. Yuan, L. Luo, W. Zhang, C.S. Lee, S.T. Lee, "Single zinc-doped indium oxide nanowire as driving transistor for organic light-emitting diode" *Appl. Phys. Lett.* 92, 153312, 2008.
- [78] D.D. Edwards, T.O. Mason, "Subsolidus Phase Relations in the Ga₂O₃–In₂O₃–SnO₂ System" *J. Am. Ceram. Soc.* 81, 3285, 1998.
- [79] A. Ambrosini, S. Malo, K.R. Poeppelmeier, M.A. Lane, C.R. Kannewurf, T.O. Mason, "Zinc Doping in Cosubstituted In_{2-2x}Sn_xZn_xO_{3-δ}" *Chem. Mater.* 14, 58, 2002.
- [80] T. Moriga, D.D. Edwards, T.O. Mason, G.B. Palmer, K.R. Poeppelmeier, J.L. Schindler, C.R. Kannewurf, I. Nakabayashi, "Phase Relationships and Physical Properties of Homologous Compounds in the Zinc Oxide–Indium Oxide System" *J. Am. Ceram. Soc.* 81, 1310, 1998.
- [81] N. Singh, T. Zhang, P.S. Lee, "The temperature-controlled growth of In₂O₃ nanowires, nanotowers and ultra-long layered nanorods" *Nanotechnology*. 20, 195605, 2009.

CITED LITERATURE (continued)

- [82] H.J. Fan, B. Fuhrmann, R. Scholz, C. Himcinschi, A. Berger, H. Leipner, A. Dadgar, A. Krost, S. Christiansen, U. Gösele, M. Zacharias, "Vapour-transport-deposition growth of ZnO nanostructures: switch between c-axial wires and a-axial belts by indium doping" *Nanotechnology*. 17, S231, 2006.
- [83] X. Zhang, J. Qin, Y. Xue, P. Yu, B. Zhang, L. Wang, R. Liu, "Effect of aspect ratio and surface defects on the photocatalytic activity of ZnO nanorods" *Sci. Rep.* 4, 4596, 2014.
- [84] J.H. Zheng, Q. Jiang, J.S. Lian, "Synthesis and optical properties of flower-like ZnO nanorods by thermal evaporation method" *Appl. Surf. Sci.* 257, 5083, 2011.
- [85] X.C. Wu, J.M. Hong, Z.J. Han, Y.R. Tao, Chem. "Fabrication and photoluminescence characteristics of single crystalline In₂O₃ nanowires" *Phys. Lett.* 373, 28, 2003.
- [86] A. Walsh A, J.L. Da Silva, S.H. Wei, C. Körber, A. Klein, L.F. Piper, A. DeMasi, K.E. Smith, G. Panaccione, P. Torelli, D.J. Payne, "Nature of the Band Gap of In₂O₃ Revealed by First-Principles Calculations" *Phys. Rev. Lett.* 100, 167402, 2008.
- [87] P. Gali, F.L. Kuo, N. Shepherd, U. Philipose, "Role of oxygen vacancies in visible emission in indium oxide nanowires" *Semicond. Sci. Technol.* 27, 015015, 2012.
- [88] S.K. Chong, S.N. Azizan, K.W. Chan, H.Q. Nguyen, W.S. Chiu, Z. Aspanut, C.F. Dee, S.A. Rahman, "Structure deformation of indium oxide from nanoparticles into nanostructured polycrystalline films" *Nanoscale Res. Lett.* 8, 1, 2013.
- [89] S. Farid, S. Mukherjee, K. Sarkar, M. Mazouchi, M.A. Stroschio, M. Dutta, "Enhanced optical properties due to indium incorporation in zinc oxide nanowires" *Appl. Phys. Lett.* 108, 021106, 2016.
- [90] B. Sen, M. Stroschio, M. Dutta, "Photoluminescence and Raman Spectroscopy of Polycrystalline ZnO nanofibers" *J. Electron. Mater.* 40, 2015, 2011.

CITED LITERATURE (continued)

- [91] Z.M. Liao, H.Z. Zhang, Y.B. Zhou, J. Xu, J.M. Zhang, D.P. Yu, "Surface effects on photoluminescence of single ZnO nanowires" *Phys. Lett. A* 372, 4505, 2008.
- [92] J.D. Ye, S.L. Gu, F. Qin, S.M. Zhu, S.M. Liu, X. Zhou, W. Liu, L.Q. Hu, R. Zhang, Y. Shi, Y.D. Zheng, "Correlation between green luminescence and morphology evolution in ZnO films" *Appl. Phys. A* 81, 759, 2005.
- [93] D.W. Hamby, D.A. Lucca, M.J. Klopstein, G. Cantwell, "Temperature dependent exciton photoluminescence of bulk ZnO" *J. Appl. Phys.* 93, 3214, 2003.
- [94] B.R. Garcia-Domene, H.M. Ortiz, O. Gomis, J.A. Sans, F.J. Manjón, A. Muñoz, P. Rodríguez-Hernández, S.N. Achary, D. Errandonea, D. Martínez-García, A.H. Romero, "High-pressure lattice dynamical study of bulk and nanocrystalline In₂O₃" *J. Appl. Phys.* 112, 123511, 2012.
- [95] C. Kranert, R. Schmidt-Grund, M. Grundmann, "Raman active phonon modes of cubic In₂O₃" *Phys. Status Solidi Rapid Res. Lett.* 8, 554, 2014.
- [96] C.A. Arguello, D.L. Rousseau, S.P.S. Porto, "First-Order Raman Effect in Wurtzite-Type Crystals" *Phys. Rev.* 181, 1351, 1969.
- [97] R. Cuscó, E. Alarcón-Lladó, J. Ibanez, L. Artús, J. Jiménez, B. Wang, M.J. Callahan, "Temperature dependence of Raman scattering in ZnO" *Phys. Rev. B* 75, 165202, 2007.
- [98] H. Morkoc, S. Strite, G. B. Gao, M. E. Lin, B. Sverdlov, and M Burns, "Large-band-gap SiC, III-V nitride, and II-VI ZnSe-based semiconductor device technologies" *J. Appl. Phys.* 76, 1363, 1994.
- [99] K. Gurnett and T. Adams, "Considerations for GaN-powered base stations" *III-Vs Review* 19, 20, 2006.

CITED LITERATURE (continued)

- [100] J. J. Shi, "Interface optical-phonon modes and electron-interface-phonon interactions in wurtzite GaN/AlN quantum wells" *Phys. Rev. B* 68, 165335, 2003.
- [101] SeGi Yu, K. W. Kim, Michael A. Stroscio, G. J. Iafrate, J.-P. Sun, and G. I. Haddad, "Transfer matrix method for interface optical-phonon modes in multiple-interface heterostructure systems" *Journal of Applied Physics* 82, 3363, 1997.
- [102] J. Gleize, J. Frandon, F. Demangeot, M. A. Renucci, M. Kuball, J. M. Hayes, F. Widmann, and B. Daudin, "Angular dispersion of polar phonons in a hexagonal GaN-AlN Superlattice" *Matter. Sci. & Eng. B* 82, 27, 2001.
- [103] J. Gleize, F. Demangeot, J. Frandon, and M. A. Renucci, F. Widmann and B. Daudin, "Phonons in a strained hexagonal GaN-AlN superlattice" *Applied Physics Letters* volume 74, number 5 1 February 1999.
- [104] M. Dutta, D. Alexon, L. Bergman, R. J. Nemanich, R. Dupuis, K.W. Kim, S. Kominrenko and M, Stroscio, "Phonons in III-V nitrides: Confined phonons and interface phonons" *Physica E*, Vol 11 277-280 2001.
- [105] C. Piquier, J. Frandon, F. Demangeot, M. Smirnov, A. Sarua, M. Kuball, E. Monroy and B. Daudin, "Behavior of phonons in short period GaN-AlN superlattices" *Phys. Stat. Sol. (c)* 1, No. 11, 2706-2710, 2004.
- [106] V. Darakchieva, E. Valcheva, and P. P. Paskov, M. Schubert, T. Paskova and B. Monemar, H. Amano and I. Akasaki, "Phonon mode behavior in strained wurtzite AlN/GaN superlattices" *Physical Review B* 71, 115329, 2005.
- [107] P. Perlin, A. Polian, and T. Suski, "Raman-scattering studies of aluminum nitride at high pressure" *Phys. Rev. B* 47, 2874, 1993.

CITED LITERATURE (continued)

- [108] SeGi Yu and K. W. Kim, Leah Bergman, Mitra Dutta, Michael A. Stroscio, and John M. Zavada, “Long-wavelength optical phonons in ternary nitride-based crystals” *Physical Review B, Condensed Matter and Materials Physics, Third Series*, Volume 58, Number 23 15 December 1998.
- [109] V. Yu. Davydov, A. N. Smirnov, M. B. Smirnov, S. V. Karpov, I. N. Goncharuk, R. N. Kyutt, M. V. Baidakova, A.V. Sakharov, E. E. Zavarin, W. V. Lundin, H. Harima, and K. Kisoda, “Lattice dynamics and Raman spectra of strained hexagonal GaN/AlN and GaN/AlGaN superlattices” *Phys. Stat. Sol. (c) 0*, No. 7, 2035–2038, 2003.
- [110] V. Yu. Davydov, N. S. Averkiev, I. N. Goncharuk, D. K. Nelson, I. P. Nikitina, A. S. Polkovnikov, A. N. Smirnov, M. A. Jacobson, and O. K. Semchinova, “Raman and photoluminescence studies of biaxial strain in GaN epitaxial layers grown on 6H–SiC” *J. Appl. Phys.* **82**, 5097, 1997.
- [111] Andrei Sarua, Hangfeng Ji, Martin Kuball, Michael J. Uren, Trevor Martin, Keith P. Hilton, and Richard S. Balmer, “Integrated Micro-Raman/Infrared Thermography Probe for Monitoring of Self-Heating in AlGaIn/GaN Transistor Structures” *IEEE Transactions On Electron Devices*, vol. 53, no. 10, October 2006.
- [112] T. Beechem, A. Christensen, S. Graham, and D. Green, “Micro-Raman thermometry in the presence of complex stresses in GaN devices” *Journal of Applied Physics* 103, 124501, 2008.
- [113] Stroscio, M. A., & Dutta, M. (2001). “Phonons in nanostructures” *Cambridge University Press*, 2001.
- [114] T. R. Hart, R. L. Aggarwal, and B. Lax, “Temperature dependence of Raman scattering in silicon,” *Phys. Rev. B, Condens. Matter*, vol. 1, no. 2, pp. 638–643, Jan. 1970.
- [115] G. Burns, F. Dacol, J. C. Marinace, B. A. Scott, and E. Burstein, “Raman scattering in thin-film waveguides” *Appl. Phys. Lett.* 22, 356, 1973.

CITED LITERATURE (continued)

- [116] G. Chen, X.Q. Wang, X. Rong, P. Wang, F.J. Xu, N. Tang, Z.X. Qin, Y.H. Chen & B. Shen, “Intersubband Transition in GaN/InGaN Multiple Quantum Wells” *Scientific Reports* 5, Article Number: 11485, 2015.
- [117] Holmstrom, P. “Electroabsorption modulator using intersubband transition in GaN-AlGaN-AlN step quantum wells” *IEEE Journal of Quantum Electronics* 42, 810, 2006.
- [118] S. Nakamura, S.F Chichibu, “Introduction to Nitride Semiconductor Blue Lasers and Light Emitting Diodes” *Taylor and Francis*, London, 2000.
- [119] A. Žukauskas, M.S. S. Nakamura, S.F Chichibu, “Introduction to Nitride Semiconductor Blue Lasers and Light Emitting Diodes” *Taylor and Francis*, London, 2000.
- [120] J. Xie, J. H. Leach, X. Ni, M. Wu, R. Shimada, Ü. Özgür, and H. Morkoç, “Electron mobility in InGaN channel heterostructure field effect transistor structures with different barriers” *Appl. Phys. Lett.* 91, 262102, 2007.
- [121] M. Miyoshi, T. Egawa, H. Ishikawa, K.-I. Asai, T. Shibata, M. Tanaka, and O. Oda, “Nanostructural characterization and two-dimensional electron-gas properties in high-mobility AlGaN/AlN/GaN/AlGaN/AlN/GaN heterostructures grown on epitaxial AlN/sapphire templates” *J. Appl. Phys.* 98, 063713, 2005.
- [122] K. Kishino, A. Kikuchi, H. Kanazawa, and T. Tachibana, “Intersubband transition in $(\text{GaN})_m/(\text{AlN})_n(\text{GaN})_m/(\text{AlN})_n$ superlattices in the wavelength range from 1.08 to 1.61 μm ” *Appl. Phys. Lett.* 81, 1234 (2002).
- [123] S. Tanaka, H. Kobayashi, H. Saito, and S. Shionoya, “Luminescence of High Density Electron-Hole Plasma in GaAs” *J. Phys. Soc. Jpn.* 49, 1051 ~1980.
- [124] C. B. A. L. Guillaume, J. M. Debever, and F. Salivan, “Radiative Recombination in Highly Excited CdS” *Phys. Rev.* 177, 567, 1969.

CITED LITERATURE (continued)

- [125] Jagdeep Shah, "Hot electrons and phonons under high intensity photoexcitation of semiconductors" *Solid-State Electronics*, Vol. 21. pp. 43-93, 1978.
- [126] Mayerhöfer, Thomas G.; Mutschke, Harald; Popp, Jürgen, "Employing Theories Far beyond Their Limits—The Case of the (Boguer-) Beer–Lambert Law". *ChemPhysChem*. 17: 1948–1955, 2016.
- [127] M Esmaeili, M Sabooni, H Haratizadeh, P P Paskov, B Monemar, P O Holz, S Kamiyama and M Iwaya, "Optical properties of GaN/AlGaIn QW nanostructures with different well and barrier widths" *J. Phys.: Condens. Matter* 19, 356218, 2007.
- [128] C. Mietze, E. A. DeCuir, Jr., M. O. Manasreh, K. Lischka, and D. J. As, "Inter- and intrasubband spectroscopy of cubic AlN/GaN superlattices grown by molecular beam epitaxy on 3C-SiC" *Phys. Status Solidi C* 7, No. 1, 64–67, 2010.
- [129] S. Juršėnas, G. Kurilėik, G. Tamulaitis, and A. Źukauskas R. Gaska and M. S. Shur M. A. Khan and J. W. Yang, "Dynamic behavior of hot-electron–hole plasma in highly excited GaN epilayers" *Appl. Phys. Lett.* 76, 2388, 2000.
- [130] S. Juršėnas, N. Kurilėik, G. Kurilėik, A. Źukauskas, P. Prystawko, M. Leszcynski, T. Suski, P. Perlin, I. Grzegory, and S. Porowski, "Decay of stimulated and spontaneous emission in highly excited homoepitaxial GaN" *Appl. Phys. Lett.* 78, 3776, 2001.
- [131] Aishi Yamamoto, Takeo Kido, Takenari Goto, Yefan Chen, Takafumi Yao, and Atsuo Kasuya, "Dynamics of photoexcited carriers in ZnO epitaxial thin films" *Applied Physics Letters* 75, 469, 1999.
- [132] J. Takeda, H. Jinnouchi, S. Kurita, Y. F. Chen, and T. Yao, "Dynamics of Photoexcited High Density Carriers in ZnO Epitaxial Thin Films" *Phys. Stat. Sol. (b)* 229, No. 2, 877–880, 2002.
- [133] C. Klingshirn, "The Luminescence of ZnO under High One- and Two Quantum Excitation" *phys. stat. sol. (b)* 71, 547, 1975.

CITED LITERATURE (continued)

- [134] I. Vurgaftman and J. R. Meyer, "Band parameters for nitrogen-containing semiconductors" *J. Appl. Phys.* 94, 3675, 2003.
- [135] J. E. Fouquet and A. E. Siegman, "Room-temperature photoluminescence times in a GaAs/Al_xGa_{1-x}As molecular beam epitaxy multiple quantum well structure" *Appl. Phys. Lett.* 46, 280, 1985.

VITA

NAME	Ketaki Sarkar
EDUCATION	<p>Ph.D, Electrical and Computer Engineering, University of Illinois at Chicago, Chicago, Illinois, 2018.</p> <p>B.Tech Instrumentation and Electronics Engineering, Jadavpur University, Kolkata, India, 2010.</p> <p>B.Sc Physics Honors, Lady Brabourne College, University of Calcutta, Kolkata, India, 2007.</p>
EXPERIENCE	<p>Teaching Assistant, Electrical and Computer Engineering, University of Illinois at Chicago, Chicago, Illinois, 2011-2017</p> <p>Research Assistant, Electrical and Computer Engineering, University of Illinois at Chicago, Chicago, Illinois, 2012-2017</p> <p>CNM User, Argonne National Laboratory, Lemont, IL, 2013-2014, 2016-2017</p> <p>Programmer Analyst Trainee, Cognizant Technology Solutions, Kolkata, India, 2010-2011.</p>
HONORS	<p>Wexler Award, Electrical and Computer Engineering, University of Illinois at Chicago, Chicago, Illinois, Fall 2011, Spring 2012.</p>

PUBLICATIONS

Debopam Datta, **Ketaki Sarkar**, Souvik Mukherjee, Xenia Meshik, Michael A Stroschio, Mitra Dutta, “Graphene oxide and DNA aptamer based sub-nanomolar potassium detecting optical nanosensor”, *Nanotechnology*, 28 (32), 325502, 2017.

Ketaki Sarkar, Souvik Mukherjee, Sidra Farid, Alan Nicholls, Michael A. Stroschio and Mitra Dutta, “Characterization of Co-existing In_2O_3 – ZnO nanostructures”, *Journal of Electronic Materials*, 46 (10), 5848-5854, 2017.

Debopam Datta, Xenia Meshik, Souvik Mukherjee, **Ketaki Sarkar**, Min S Choi, Mojgan Mazouchi, Sidra Farid, Yung Yu Wang, Peter Burke, Mitra Dutta, Michael A. Stroschio, “Sub-millimolar detection of Adenosine Monophosphate using graphene based electrochemical aptasensor”, *IEEE Transactions on Nanotechnology* 16 (2), 196-202.

S. Farid, S. Mukherjee, **K. Sarkar**, M. Mazouchi, M. A. Stroschio and M. Dutta, “Enhanced optical properties due to indium incorporation in zinc oxide nanowires”, *Appl.Phys.Lett*, 108, 021106 (2016).

Souvik Mukherjee, Xenia Meshik, Min Choi, Sidra Farid, Debopam Datta, Yi Lan, Shripriya Poduri, **Ketaki Sarkar**, Undarmaa Baterdene, Ching-En Huang, Yung Yu Wang, Peter Burke, Member, IEEE, Mitra Dutta, Fellow, IEEE, and Michael A. Stroschio, Fellow, IEEE, “A graphene and aptamer based liquid gated FET-like electrochemical biosensor to detect adenosine triphosphate”, *IEEE Trans. on Nanobioscience*, Vol. 14, No. 8, December 2015.

Ketaki Sarkar, Sidra Farid, Souvik Mukherjee, Michael A. Stroschio, Mitra Dutta, Plasmonic enhancement of ZnO and Indium doped ZnO nanowires

using surface sputtered Au metallic nanoparticles, 2016 APS/CNM Users Meeting

Ketaki Sarkar, Richard D Schaller, Michael A Stroscio and Mitra Dutta, “Stimulated emission and optical pumping of lasing from ZnO nanostructures: effect of morphology and surface treatment”, 2017 *Fall Meeting of the APS Prairie Section*, November 11-12, 2017, University of Illinois at Chicago, Chicago, IL

Ketaki Sarkar, Souvik Mukherjee, Gary Wiederrecht, Richard D Schaller, David J Gosztola, Michael A Stroscio and Mitra Dutta, “Stimulated emission and optical pumping of lasing from ZnO nanostructures: effect of morphology and surface treatment”, submitted to *Nanotechnology*.

Ketaki Sarkar, Debopam Dutta, David J Gosztola, Michael A Stroscio and Mitra Dutta, “Raman analysis of phonon modes in a short period AlN/GaN superlattice” to be submitted to *Superlattices & Microstructures*.

Souvik Mukherjee, **Ketaki Sarkar**, Gary Wiederrecht, Richard D Schaller, David J Gosztola, Michael A Stroscio and Mitra Dutta, "Defect induced structural inhomogeneity, ultraviolet light emission and near-band-edge photoluminescence broadening in degenerate In₂O₃ nanowires", to be submitted to *Nanotechnology*.